

Self-replicating fuels via autocatalytic molecular bond fission

Peter Agbo^{1,2,3*}

¹Chemical Sciences Division
Lawrence Berkeley National Laboratory
Berkeley, CA 94720 USA

²Molecular Biophysics & Integrated Bioimaging Division
Lawrence Berkeley National Laboratory
Berkeley, CA 94720 USA

³Carbon Negative Initiative
Lawrence Berkeley National Laboratory
Berkeley, CA 94720, United States

*Corresponding author

Abstract

This computational study advances a theoretical framework for practical, electrochemical fuel generation displaying exponential product yields and product formation rates as functions of time. Exponential reaction scaling for formate/formic acid replication is simulated through an autocatalytic cycle that emulates the process of DNA replication facilitated by the well-known polymerase chain reaction (PCR). Here, an initial buildup of formate into a two-carbon chain through CO₂ carboxylation forms oxalate. A subsequent, two-electron reduction yields glyoxylate, with base-mediated hydrolysis driving C-C bond fission of glyoxylate into two molecules of formate. These products are then recycled back to serve as reactants. This recursive process chemistry displays 2ⁿ stoichiometries with respect to formate growth in the limit of ideal reaction selectivity. Each step of the proposed fuel cycle shows direct analogy to the steps of DNA annealing, nucleotide polymerization and hybridized strand fission that are responsible for the exponential product yields observed in PCR-mediated DNA synthesis. As a consequence of this replication behavior, rapid rates of fuel production are accessible even when the individual rate constants for the cycle's constituent processes are slow. Significant focus is placed on practical routes for realizing each of the three steps comprising this model case of formate replication, particularly the challenge of formate carboxylation and the corresponding energy demands and power constraints of the overall process.

Introduction

The application of nonlinear chemical processes are often treated as the purview of a relatively small number of chemical specialists, constituting a niche chemical field rather than a key part of all chemical sub-disciplines. The subset of chemical research dealing with renewable energy and fuels synthesis has been no different in the general attention given to nonlinear chemistries, with the vast majority of research in this area falling under the umbrella of linear scaling reactions.

Binary cell division (mitosis) displays exponential growth, with population sizes evolving according to a 2^n expansion rule, where n is the doubling time¹. Similarly, the process of DNA amplification using the polymerase chain reaction (PCR) has shown the possibility of crafting chemical reactions where temporal product yields have an exponential dependence, rather than following the linear time dependencies found in most chemical systems². In physics, such nonlinearities are also common. For example, both lasing³ and nuclear fission^{4,5} exhibit exponential increases in photon yield (as a function of input power) and $^{235}\text{U}/^{240}\text{Pu}$ fission rates (as a function of incident neutron flux), respectively. However, despite the clear prevalence of nonlinear processes in biology and physics, the mainstream application of nonlinear reactions in chemical disciplines - particularly renewable energy research - remains a comparatively marginal subject area⁶⁻⁸. In chemistry, autocatalysis has generally been couched in studies exploring its relevance to origin of life chemistry^{9,10}, the behavior of atmospheric aerosols¹¹, molecular synthesis/self-assembly¹²⁻¹⁴, and nanoparticulate growth¹⁵. However, in direct analogy to this study, recent work in the field of capacitive energy storage has demonstrated the possibility of constructing systems where rates of energy storage scale nonlinearly as a function of cycle number¹⁶. A key distinction between forms of autocatalysis such as nuclear fission and the chain reactions comprising chemical explosions, versus phenomena like DNA and cell replication, is that the former represent processes where autocatalytic behavior drives rapid energy release, whereas the latter are thermodynamically-driven processes demanding the uptake of energy from the environment. As a result, these driven processes effectively concentrate the diffuse energy of a thermal bath into energy-dense entities such as the biosynthetic components of a cell or the phosphoanhydride bonds comprising replicating nucleic acids. This latter class of driven autocatalytic processes are effectively fuel-forming reactions, as they result in products where energy has been stored and inspire the type of autocatalytic reaction sequence discussed here. This understanding establishes autocatalytic fuel production as the conjugate of a process such as nuclear fission, where now, instead of rapid expansions in the rate of energy release over time, energy from some power source is rapidly incorporated as fuel at increasing rates with time.

This concentrating of energy in some fuel product occurs in a manner distinct from normal, fuel-forming processes, where the kinetics of energy conversion to fuel are generally constant with time, and fuel concentrations can only scale linearly as the product of time and reaction rate. This serves as key advantage of autocatalysis: because the reactant is also the product, this leads to higher-order scaling in reaction rates as functions of time and reactant concentration, in stark contrast to linear processes where reaction orders are simply 1st or 2nd order with respect to reactant concentration and invariant with time. As a consequence of this, an autocatalytic fuel cycle can achieve very fast rates of catalysis, even for systems with very slow rate constants. In the context of electrochemical reactions, such behavior carries the additional possibility of constructing devices where mass-transport impedances actually decrease with time, as rates of substrate flux to electrode active sites rapidly increase with the rapidly growing substrate concentration. Furthermore, because these reactions can be efficiently run as batch processes (with respect to the reactant/product), the rapid product growth means that they effectively incorporate the task of fuel production and fuel concentration into a single step.

This paper presents a theoretical study exploring a non-linear amplification mechanism for the generation of formate, a prospective hydrogen carrier and renewable fuel¹⁷. More broadly, this work aims to establish the general approach for rationally designing autocatalytic processes for renewable, self-replicating chemical fuel production. The reported concept repurposes the autocatalytic mechanism for the *in-vitro* replication of DNA via PCR as a generic reaction template, upon which a specific process for the autocatalytic generation of formate is

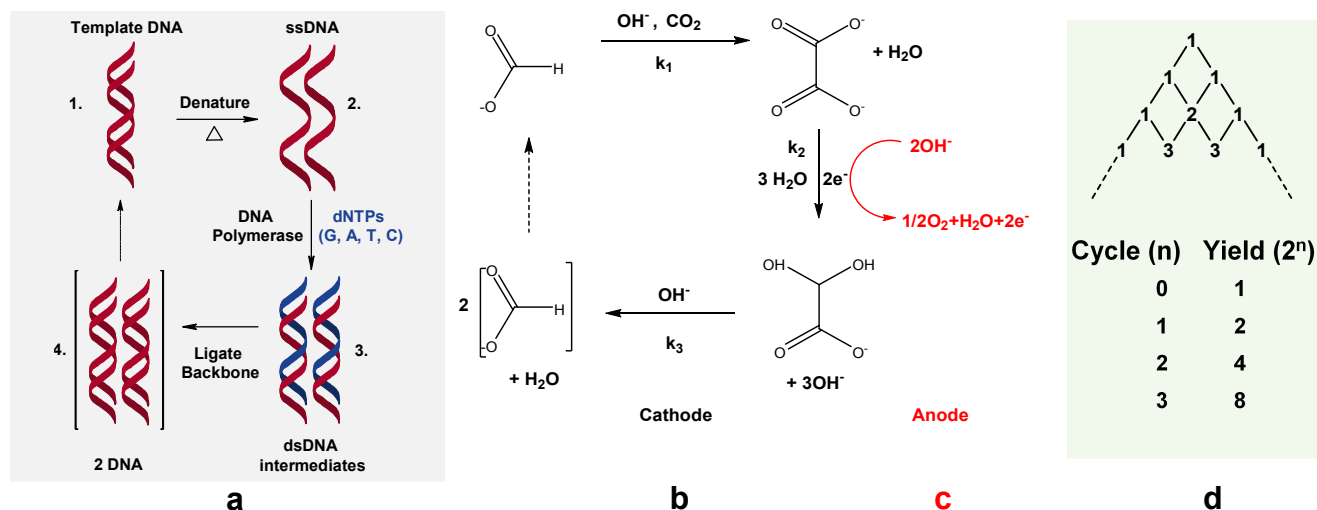


Figure 1

a) The chemical mechanism of the polymerase chain reaction. Replication of a single DNA molecule (and strand) exhibits exponential growth kinetics (amplification) in regimes where the reaction order is pseudo-first order in [DNA], with the deoxynucleotide triphosphates (dNTPs) serving as the monomer building blocks present in excess. In the ideal limit, reaction kinetics follow a 2^n expansion rule, where n is the cycle number. At high cycle numbers (longer times), dNTP consumption results in DNA replication kinetics that are limited by [dNTP], arresting polymerization at long times. **b)** A PCR-analogous scheme for formate generation. Exponential formate yields are initially seeded by a low concentration of the compound, with CO_2 serving as a building block analogous to the role played by dNTPs in PCR. The C-C coupling of CO_2 and formate in the first reaction step, and the hydrolytic C-C bond fission of glyoxylate to yield two formate molecules in step 3, can be viewed as equivalent to the respective steps of annealing and denaturation found in PCR cycles. **c)** The step of oxalate reduction (step 2) points to the possibility of driving this formate cycle by coupling this redox process to electrochemical or photoelectrochemical water-splitting. **d)** In the limit of perfect cycle efficiencies, product yields in these schemes follow Pascal's triangle.

superimposed. Starting from the PCR template scheme, retrosynthetic analysis was applied to determine the intermediate compounds needed to generate two formate molecules from an initial input of one formate molecule and one molecule of carbon dioxide. The recursive chemical mechanism resulting from this reverse-engineered approach displays exponential generation of formate with respect to time, in direct relation to the exponential yields of DNA realized through PCR. In this report, the proposed autocatalytic cycle for formate evolution is decomposed into three reaction steps. Each of these are explored at successively-increasing levels of mechanistic detail, following realistic strategies for driving them using existing chemistries. Through this exercise, we demonstrate that each of three basic reactions in the proposed cycle are possible, if challenging. Complexities that arise with increasing mechanistic granularity are addressed, including observed deviations from ideal exponential behavior that occur as a result of substrate depletion and reaction branching in the radical mechanisms used for simulating reaction 1, the net carboxylation of formate. A discussion is provided of the requirements that each elementary step of the proposed mechanism must satisfy for exponential growth kinetics to be observed, along with the thermodynamic constraints of a self-replicating fuel cycle. The requirements for satisfying the exponentially-growing energy demands for sustaining such a cycle are discussed, and a prospective route for dealing with this challenge in practice is proposed. The practical implications of generating exponential yields of a chemical fuel product with time are provided as strong arguments for the potential of nonlinear reactions to augment the existing linear approaches that currently define the vast majority of energy storage research in the chemical sciences. Finally, a generalized set of design rules governing the construction of autocatalytic reactions dependent on

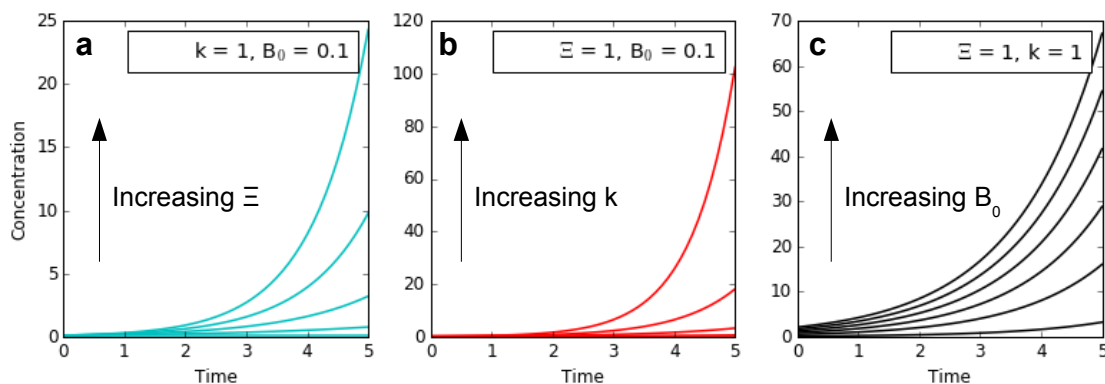


Figure 2

Dependencies of unbounded autocatalytic growth functions (exponential phase only), describing some arbitrary, chemical replicator, on parameters **(a)** Ξ , the reaction selectivity for a product, **(b)** the cycle rate constant, $k = 1/\tau$ and **(c)** the seed concentration of the replicator, B_0 . While these functions are only idealized representations displaying no limits on growth, these relationships usefully describe the key dependencies of real autocatalytic replication during the exponential growth phase, for reaction types that include PCR, formate amplification in this study and reactions with 2^n scaling generally.

molecular fission events are outlined, with an emphasis on their applicability to a wider range of chemical transformations.

Results

Concept Framework

As the analogy with PCR would suggest, mathematical descriptions of the proposed system for exponential formate production parallel those used to describe PCR-mediated DNA amplification¹⁸. The net reaction scheme is reducible to the simplest case of autocatalytic sets, of the form:



In this study, substrate A (CO_2) is supplied at a steady-state concentration required for sustaining the amplification of species B (formate). Here, formate generation per cycle follows a power rule:

$$B(n) = B_0 [1 + \Xi_n]^n \quad \text{eq. 1b,}$$

where n refers to the n^{th} reaction cycle, B_0 is the initial formate concentration, and Ξ_n refers to the conversion selectivity of each cycle for the production of two formate molecules from one molecule of CO_2 and one molecule of formate. In the ideal limit of no side reactions, a cycle selectivity of 100% results. Discrete cycles may be expressed as continuous functions of time (t) through the relation $n = t/\tau$, where τ is the characteristic time constant for each reaction cycle. A characteristic rate constant is given by $k = 1/\tau$. These relations permit the description of concentration as a continuous function of time:

$$B(t) = B_0 [1 + \Xi(t)]^{\frac{t}{\tau}} = B_0 [1 + \Xi(t)]^{kt} \quad \text{eq. 1c.}$$

Differentiation of eq. 1b with respect to time yields the rate equation for formate evolution:

$$r(t) = \frac{dB(t)}{dt} = B_0 k \frac{d\Xi}{dt} [1 + \Xi(t)]^{kt} \quad \text{eq. 1d.}$$

The general form of eqs. 1a-c speak to the exponential nature of formate production in the scheme described, with dependencies on the parameters τ , Ξ , and B_0 as depicted in Figure 2. The parameter $\tau = 1/k$ (where k is a unimolecular rate constant) describes the characteristic time required for the n^{th} reaction cycle to complete. In the limit of a reaction cycle featuring no side reactions, $\Xi(t)$ converges to 1 and the bracketed quantity collapses to 2^n ($2^{t/\tau}$), resulting in a growth function displaying exponential behavior. While this represents a theoretical limit on yields per cycle, it should be noted that exponential growth may be observed for all $\Xi(t) > 0$. In the limit $\Xi(t) \rightarrow 0$, reaction kinetics will converge towards arrested growth. It should be noted that equations 1b-d, while descriptive of the system explored here, are not generalized expressions for autocatalysis, such as those laid out by Hanopolskyi et al.¹⁹, or expressed by logistic growth equations²⁰, which are rigorously derived and incorporate the effects of exponential plateau in the limit of reactant depletion. However, the use of equations 1 and 2 in this study was preferred as a result their expressing nonlinear expansion intuitively, while enabling a sharp parallel to be cast between the power functions commonly used to describe the PCR¹⁸, cell replication¹ and nuclear fission processes that inspired this approach. In this current study, simulations are performed over a model system that is a semi-batch process, with CO_2 treated as a reactant supplied at a steady-state concentration. It is therefore not subject to depletion kinetics; all other species are treated as batch quantities, provided either at the start of the simulation or evolved through the course of autocatalytic cycling. Steady-state CO_2 concentrations carry the implicit understanding that for a real system, this means that rates of CO_2 flux into the solution bulk must occur at rates fast enough to accommodate the rate of CO_2 consumption by autocatalysis, which must increase over time to sustain formate replication. Finally, rates of energy delivery into this thermodynamically-driven cycle serve as an ultimate limit on the system's replication kinetics. In this study, the endergonic conversions of formate to oxalate and oxalate reduction to glyoxylate are the points of external energy consumption by the replicating system.

While some PCR models assume a static product selectivity, a generalized, time-dependent description of process selectivity will more accurately capture the system's time-evolution¹⁸. Using the proposed scheme outlined in Figure 1b, the product selectivity (Ξ) for any particular j^{th} step of the fuel cycle may be generally expressed as:

$$\Xi = \frac{(r_f - r_b)}{(r_f - r_b) + \sum (r_{s,f} - r_{s,b})} \quad \text{eq. 2a,}$$

where the summation in the numerator gives the total rate of all back and forward side reactions ($r_{s,f}$, $r_{s,b}$), and terms r_f , r_b give the rates of the primary forward and back reactions, respectively. Applying this formula to the reaction scheme outlined in Table 1, the selectivity for step 1 may then be expressed as:

$$\Xi_1(t) = \frac{k_1[\text{HCO}_2](t)[\text{CO}_2](t) - k'_1[\text{oxa}](t)}{k_1[\text{HCO}_2](t)[\text{CO}_2](t) - k'_1[\text{oxa}](t) + k_{s1}[\text{HCO}_2](t) - \sum_i k'_{s1i}[\text{S}_{1i}](t)} \quad \text{eq. 2b.}$$

Terms k_i and k'_i give the rates of the primary forward and back reactions for the first step of the cycle, k'_{s1i} is the rate constant for the i^{th} side reaction, $[\text{HCO}_2]$ is the formate concentration and $[\text{oxa}]$ refers to the concentration of oxalate. The selectivity for step two, the two-electron reduction of oxalate to dihydroxyacetate (DHA, the equilibrium hydrate of glyoxylate) is expressed as:

$$\Xi_2(t) = \frac{k_2[\text{oxa}](t) - k_2'[\text{DHA}](t) + k_{S_2}[\text{oxa}](t)}{k_2[\text{oxa}](t) - k_2'[\text{DHA}](t) + k_{S_2}[\text{oxa}](t) - \sum_i k'_{S_{2i}}[\text{S}_{2i}](t)} \quad \text{eq. 2c.}$$

Here, k_2 , and k_2' give the rates of the primary forward and back reactions for the second cycle step, while k_{S_2} and $k'_{S_{2i}}$ are the rate constants for the forward and i^{th} reverse side reactions of the second step. The term [DHA] denotes the concentration of dihydroxyacetate; [OH⁻] refers to the hydroxide ion concentration. For the third step, a similar expression for reaction selectivity results, yielding eq. 2d:

$$\Xi_3(t) = \frac{k_3[\text{DHA}][\text{OH}^-](t)}{k_3[\text{DHA}][\text{OH}^-](t) + k_{S_3}[\text{DHA}](t) + \sum_i k'_{S_{3i}}[\text{S}_{3i}](t)} \quad \text{eq. 2d.}$$

Terms k_3 , and k_3' give the rates of the primary forward and back reactions for the third step of the reaction cycle, DHA hydrolysis to two molecules of formate. Constants k_{S_3} and $k'_{S_{3i}}$ are the rate constants for the forward and i^{th} reverse side reactions of the third step. The overall, time-dependent selectivity of the entire fuel cycle is then given by the product of the individual step efficiencies:

$$\Xi(t) = \prod_{j=1}^3 \Xi_j(t) \quad \text{eq. 2e.}$$

In this formulation, time dependence of individual reaction and overall cycle selectivity is captured by the rate constants defining product formation kinetics for each step (S.5). The resulting system may be viewed as a fundamental autocatalytic “core,” according to certain taxonomic classifications for autocatalytic processes²¹.

As a time-dependent selectivity implies, real replication processes may be expected to deviate significantly from perfect exponential growth. Even where selectivity is ideal, such deviations occur for all physical replicators bounded by a physical limit, such as limiting reactant or energy availability from the replicator’s surroundings. As a result, determining key aspects of the replicator behavior, such as the maximum value of its rate constant, becomes difficult and makes rigorous application of growth models such as those encapsulated by eqs. 1b-1d difficult, as exponential growth phases deviate from ideality. To deal with this, this paper introduces the following analytical approach, which exploits the fact that for an ideal replicator, the logarithm of its growth with respect to time is linear. As a result, any deviations from linearity indicate times where replication starts to diverge from purely exponential (ideal) growth kinetics as a result of limiting processes. Taking the logarithm of eq. 1c gives:

$$\ln(B(t)) = kt \ln[1 + \Xi(t)] + \ln(B_0) \quad \text{eq. 2f.}$$

For times where selectivity is constant, this yields a slope of $k \ln(B_0[1 + \Xi])$ and equals $k \ln(2B_0)$ for an ideal 2^t scaling replicator. Furthermore, taking the derivative of equation 2f yields:

$$\frac{d \ln(B(t))}{dt} = k \ln[1 + \Xi(t)] + \frac{kt}{[1 + \Xi(t)]} \frac{d \Xi}{dt} \quad \text{eq. 2g.}$$

The time-invariant selectivity of an ideal replicator forces the differential term $d \Xi / dt$ to zero, causing the time dependent term of eq. 2g to vanish. In this limit, eq. 2g collapses to a time-independent term of constant Ξ , the case for an ideal replicator following purely exponential growth kinetics:

$$\frac{d\ln(B(t))}{dt} = k\ln[1+\Xi] \quad \text{eq. 2h.}$$

As a result, using either eqs. 2f or 2h, we can readily determine the points at which a non-ideal replicator deviates from ideality and extract approximate values for k (or Ξ) (S.1). The result expands the analytical utility of the idealized exponential replicator model for parameter extraction from realistic cases of bounded, non-deal autocatalysts (S.1).

Table 1 – Simulated ‘Basic’ System

Reaction	Forward	Units	Reverse	Units	Ref
Autocatalytic System					
(1) $\text{HCO}_2^- + \text{CO}_2 + \text{H}_2\text{O} \rightarrow \text{C}_2\text{O}_4^{2-} + \text{H}_3\text{O}^+$	$k_1 = 10$	$\text{M}^{-1} \text{s}^{-1}$	--	--	--
(2) $\text{C}_2\text{O}_4^{2-} + 2 \text{H}_2\text{O} \rightarrow \text{C}_2\text{H}_3\text{O}_4^- + \text{OH}^- + 0.5 \text{O}_2$	$k_2 = 0.01$	s^{-1}	--	--	--
(3) $\text{C}_2\text{H}_3\text{O}_4^- + \text{OH}^- \rightarrow 2 \text{HCO}_2^- + \text{H}_2\text{O}$	$k_3 = 1000$	$\text{M}^{-1} \text{s}^{-1}$	--	--	--
Buffering Equilibria (pK_{a1} = 8, pK_{a2} = 13)					
$\text{H}_3\text{O}^+ + \text{B}^- \leftrightarrow \text{BH} + \text{H}_2\text{O}$	$k_a = 1\text{e}8$	$\text{M}^{-1} \text{s}^{-1}$	$k_a' = 1$	s^{-1}	--
$\text{OH}^- + \text{BH} \leftrightarrow \text{B}^- + \text{H}_2\text{O}$	$k_b = 1\text{e}6$	$\text{M}^{-1} \text{s}^{-1}$	$k_b' = 1$	s^{-1}	--
$\text{BH} + \text{H}_3\text{O}^+ \leftrightarrow \text{BH}_2 + \text{H}_2\text{O}$	$k_a = 1\text{e}13$	$\text{M}^{-1} \text{s}^{-1}$	$k_a' = 1$	s^{-1}	--
$\text{OH}^- + \text{BH}_2 \leftrightarrow \text{BH} + \text{H}_2\text{O}$	$k_b = 1\text{e}1$	$\text{M}^{-1} \text{s}^{-1}$	$k_b' = 1$	s^{-1}	--
Solvent Autoionization					
$\text{H}_3\text{O}^+ + \text{OH}^- \leftrightarrow 2 \text{H}_2\text{O}$	$k_w = 1.12\text{e}11$	$\text{M}^{-1} \text{s}^{-1}$	$k_w' = 1.12\text{e}-3$	s^{-1}	²²

Fuel replication kinetics – ‘Basic System,’ ideal replicator

The fuel cycle under consideration can be represented using the elementary reactions outlined in Table 1: Reactions (1) and (3) represent reactions both difficult to facilitate and with little-studied kinetics. As a result, for demonstration purposes, rate constants spanning orders of magnitude were sampled for these reactions. In an effort to keep the simulation assumptions conservative as possible, the range of rate constants tested for reactions (1) and (3) span relatively low values for bimolecular kinetics, with a base case of only $10 \text{ M}^{-1} \text{ s}^{-1}$ for reaction (1) and $1000 \text{ M}^{-1} \text{ s}^{-1}$ for reaction (3). Buffering reaction rates were determined using values for rate constants of proton/base recombination in autoionization equilibria²², in conjunction with equilibrium constants for respective buffer pK_a values and water dissociation processes (Table S1).

Simulations of the autocatalytic fuel cycle described here were carried out using Kinetiscope. As a stochastic kinetics simulation engine, Kinetiscope discretizes the problem of microkinetics simulation using the formalism pioneered by Gillespie²³, explicitly tracking the time evolution of all molecules in a reaction volume. Using the reaction scheme above, which results in the production of two molecules of formate each cycle, stochastic calculations of formate yield over time are found to amplify the concentration of formate in a manner analogous to the amplification of DNA produced via PCR. Rather than a linear increase in the product concentration with time, formate production for cases of a constant CO₂ concentration in solution ($100 \mu\text{M}$) is characterized by a fast exponential rise, with the concentration of formate exceeding 1.5 M within the first 12000 s of the reaction (Figure 3a), for a reaction seeded with $100 \mu\text{M}$ formate at $t = 0 \text{ s}$. It is worth observing that this autocatalytic cycle may,

in principle, be seeded with any of the reaction intermediates – formate, oxalate or DHA. In cases where bulk CO_2 concentrations are not held constant, CO_2 availability rapidly becomes limiting, resulting in transient reactions whose rates quickly decay, with only negligible amounts of formate being generated (S.6). Expanding the buffering equilibria in this system to include actual values for phosphate and inorganic carbon (DIC) speciation has virtually no effect on the system behavior over the examined timescale (S.1, Figure S3).

In this process, the conversion of oxalate to DHA represents a redox process; coupling this two-electron reduction to the oxygen evolution reaction yields the overall redox equation embodied in reaction 2. As a result, we can consider how an electrochemical cell that integrates autocatalysis will respond. Comparing autocatalytic formate yields to the performance of an equivalent CO_2 -to-formate electrolyzer (operating with an electrocatalyst with the same active site density (A) of 10^{17} cm^{-2} , and a catalytic rate constant equal to the characteristic rate constant of the autocatalytic cycle, 0.0013 s^{-1}) illustrates the dramatic differences between the linear vs autocatalytic fuel synthesis. Explicit calculation of the autocatalytic electrolyzer current is readily achieved by taking the first-derivative of the oxygen concentration with respect to time:

$$J = nF v_{\text{rxn}} \frac{d[\text{O}_2]}{dt} \quad \text{eq. 3a,}$$

where F is Faraday’s constant, n ($= 4$) is the number of electrons transferred per substrate turnover, and v_{rxn} is the simulation reaction volume. This is in stark contrast to the current calculated for a comparable linear electrolyzer with a catalytic turnover rate of 0.0013 s^{-1} , which yields a steady-state current of $42 \mu\text{A cm}^{-2}$ according to:

$$J = \frac{nFAk_{\text{cat}}}{N_A} \quad \text{eq. 3b.}$$

Here we assume the ideal case, where a linear electrolyzer operates at a current limit controlled only by the total density of electrocatalyst active sites and $k_{\text{cat}} = 0.0013 \text{ s}^{-1}$ is a catalytic rate constant. Evidence of these trends are found in Figure 3d.

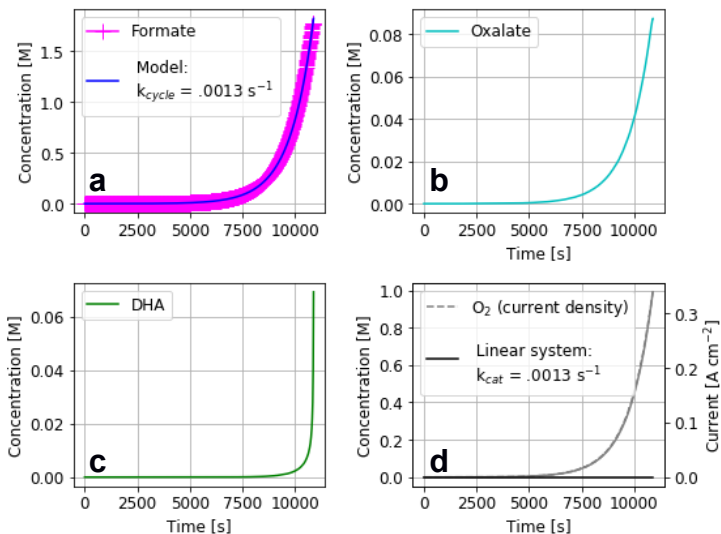


Figure 3

a) A simulation of ideal, unbounded formate autocatalysis according to a PCR-analogous mechanism described in Table 1. $B_0 = 100 \mu\text{M}$; $[\text{CO}_2]$ is held constant at $100 \mu\text{M}$. Data shown are for the exponential phase. As an ideal autocatalytic system, growth can be modeled with eqs. 1c and 1d, for $k_{\text{cycle}} = 1/\tau = 0.0013 \text{ s}^{-1}$, $\Xi=1$. Nonlinearity in the fuel cycle also results in exponential scaling in the growth of oxalate (b) and glyoxylyate (c) intermediates as functions of time, with relative growth rates set by the relative rate constants feeding and consuming each species. (d) Coupling the reductive chemistry of the autocatalytic cycle to electrochemical oxygen evolution suggests the possibility of driving such processes electrochemically, provided that energetic sinks are sufficiently power-dense to drive the process. Here, measurement of the first derivative of O_2 evolution (gray) is used to calculate total current consumed in the generation of all reductive intermediates in the cycle for all times t . Comparison to an idealized, traditional electrolyzer system (black) operating within a regime only limited by active site density (10^{17} cm^{-2} used for calculation). Linear electrolyzer current is calculated using turnover rate constant equal to k_{cycle} , yielding a steady-state device current density of $42 \mu\text{A cm}^{-2}$.

This carries direct implications for the expected current response for any electrolyzer employing this autocatalytic cycle. First, the exponential increase in the rate of formate production means the rate of charge flow must scale similarly, with electrical current increasing with time. In contrast to a typical electrolyzer, where catalytic turnover depletes available substrate, here a feedback exists between electrolyzer current and substrate concentration, as cathodic turnover will lead to increasing concentrations of oxalate (Figure 3b). As a result, the high current densities required by the system at long times are facilitated, in part, by the increasing substrate availability. In fact, even for cases where the catalyst has a low binding affinity or turnover rate for the substrate, catalysis would be expected to become more efficient as catalysis proceeds and substrate concentration increases with successive turnovers. Such an approach offers practical utility for electrocatalysts that may be highly selective but have catalytic rate constants too low to be of use in linear electrolyzers, with substrate amplification making high current densities accessible in such systems.

A clear challenge associated with implementing this type of nonlinear scheme is highlighted by the rates of side products evolved, which themselves display exponential amplification (Figures 3b, 3c). However, any interference from amplified side products will depend on the particulars of the side reactions, especially their associated rate constants. Despite the focus on formate production here, each of the intermediates involved in the proposed autocatalytic cycle are subject to exponential growth. The relative growth rates of formate, oxalate, and DHA are functions of the rate constants for the reactions driving both their formation and depletion. As a result of this dependence, it becomes possible to control the selectivity of the cycle for one intermediate over another, allowing for significant shifts in the product accumulation profile. While the base case tested ($k_1 = 10 \text{ M}^{-1} \text{ s}^{-1}$, $k_2 = 0.01 \text{ s}^{-1}$, $k_3 = 1000 \text{ M}^{-1} \text{ s}^{-1}$) causes formate growth to occur at rates significantly greater than that of oxalate or DHA, modifying the simulation by slowing down the depletion of DHA ($k_3 = 1 \text{ s}^{-1}$) results in a significantly faster rate of DHA growth, with the decreased rate constant enabling the buildup of this intermediate. Similarly, increasing k_1 to 10 s^{-1} or decreasing k_2 to 0.1 s^{-1} is shown to increase the rate of oxalate accumulation (S.4). This also has clear implications with respect to control of reaction pH; various simulation scenarios show that the nonlinear base accumulation – rapid increases in pH – may result in such cycles. In the context of formate production, these properties signal how such an autocatalytic process may be designed to maximize the purity of formate in the reaction volume, through appropriate control of the relative values of the individual reaction rate constants.

Fuel replication kinetics – ‘Partial Mechanistic System,’ non-ideal replicator

Attempting to simulate this system using the stoichiometric rate laws for the net reactions requires invoking direct formate carboxylation in step (1) and termolecular reactions in step (3). However, formate carboxylation invokes the C-C coupling of two low-energy carbon compounds that are famously difficult to activate. Meanwhile, termolecular processes are typically discounted as relevant kinetic processes, as they require the coincidence of three reactive species in three dimensions, and therefore occur with only vanishing probabilities in real systems. In addition, reaction (2) represents a redox process, which must be expressed as an explicit sum of paired oxidation/reduction reactions in order to be meaningfully simulated. As a result, we must build in system complexity by decomposing these three reactions into their serial, mechanistic processes. We start by first expressing reactions (2) and (3) as discrete, mechanistic steps (Table 2):

Table 2 – Simulated ‘Partial Mechanistic’ System

Reaction	Forward	Units	Reverse	Units	Ref
Autocatalytic System					
(1) $\text{HCO}_2^- + \text{CO}_2 + \text{H}_2\text{O} \rightarrow \text{C}_2\text{O}_4^{2-} + \text{H}_3\text{O}^+$	10	$\text{M}^{-1} \text{ s}^{-1}$	--	--	--
(2) $\text{C}_2\text{O}_4^{2-} + 2 \text{H}_2\text{O} \rightarrow \text{C}_2\text{H}_3\text{O}_4^- + \text{OH}^- + 0.5 \text{O}_2$					

Cathode: $C_2O_4^{2-} + 3 H_2O + 2e^- \rightarrow C_2H_3O_4^- + 3 OH^-$						
2.1	$C_2O_4^{2-}(aq) + A \leftrightarrow A-C_2O_4^{2-}(ads)$	2.4	s^{-1}	0.8	s^{-1}	S.2
2.2	$A-C_2O_4^{2-}(ads) + 2 H_2O + 2e^- \leftrightarrow A-C_2HO_3^-(ads) + 3 OH^-$	215	s^{-1}	0.002	s^{-1}	S.3
2.3	$A-C_2HO_3^-(ads) \leftrightarrow C_2HO_3^-(aq) + A$	0.8	s^{-1}	2.4	s^{-1}	S.2
2.4	$C_2HO_3^-(aq) + H_2O \leftrightarrow C_2H_3O_4^-(aq)$	70	s^{-1}	1.14	s^{-1}	²⁴
Anode: $2 OH^- \leftrightarrow H_2O + 0.5 O_2 + 2e^-$		215	s^{-1}	0.002	s^{-1}	S.3
(3) $C_2H_3O_4^- + OH^- \rightarrow 2 HCO_2^- + H_2O$						
3.1	$C_2H_3O_4^- + Cat \leftrightarrow Cat-C_2H_3O_4^-$	100	$M^{-1} s^{-1}$	1	s^{-1}	S.7
3.2	$Cat-C_2H_3O_4^- + OH^- \leftrightarrow Cat-DHA^*$	1000	$M^{-1} s^{-1}$	1	s^{-1}	S.7
3.3	$Cat-DHA^* \rightarrow 2 HCO_2^- + Cat + H_2O$	10	s^{-1}	--	--	S.7
Buffering Equilibria						
Phosphate – Values for $H_3PO_4^- (BH_2) \leftrightarrow H_2PO_4^{2-} (BH) \leftrightarrow HPO_4^{3-} (B^-)$ equilibrium ($pK_{a1} = 7.20$, $pK_{a2} = 12.32$)						
	$H_3O^+ + B^- \leftrightarrow BH + H_2O$	1.58e7	$M^{-1} s^{-1}$	1	s^{-1}	²⁵
	$OH^- + BH \leftrightarrow B^- + H_2O$	6.34e6	$M^{-1} s^{-1}$	1	s^{-1}	²⁵
	$BH + H_3O^+ \leftrightarrow BH_2 + H_2O$	2.38e12	$M^{-1} s^{-1}$	1	s^{-1}	²⁵
	$OH^- + BH_2 \leftrightarrow BH + H_2O$	4.21e1	$M^{-1} s^{-1}$	1	s^{-1}	²⁵
Carbonate						
	$CO_2 + H_2O \leftrightarrow H_2CO_3$	0.04	s^{-1}	12	s^{-1}	²⁶⁻²⁹
	$CO_2 + OH^- \leftrightarrow HCO_3^-$	1.21e4	$M^{-1} s^{-1}$	4e-4	s^{-1}	²⁹
	$H_2CO_3 \leftrightarrow H^+ + HCO_3^-$	1e7	s^{-1}	5e10	$M^{-1} s^{-1}$	²⁸
	$HCO_3^- \leftrightarrow H^+ + CO_3^{2-}$	3	s^{-1}	5e10	$M^{-1} s^{-1}$	²⁸
Solvent Autoionization						
	$H_3O^+ + OH^- \leftrightarrow 2 H_2O$	$k_w = 1.1e11$	$M^{-1} s^{-1}$	$k_w' = 1.1e-3$	s^{-1}	²²

The second step of the cycle, oxalate reduction to glyoxylate, represents a process that is readily achievable within the bounds of known electrochemistry. In particular, previous work has demonstrated the possibility of reducing oxalate formed *in situ* (via CO_2 reduction) to glyoxylate under alkaline conditions³⁰⁻³³. In the mechanism for step (2), A represents a free electrode active site, available for oxalate binding and subsequent reduction to glyoxylate. At time zero, $[A]_0$ equals the total active site concentration, $[A]_T$, with an active site population that evolves over the course of formate replication according to:

$$[A](t) = [A]_0 - [A-oxa_{(ads)}](t) - [A-Gly_{(ads)}](t). \quad \text{eq. 4a.}$$

A value of $[A]_0 = 10^{17} \text{ cm}^{-2}$ is used for initializing these simulations, as it represents a number within range of a typical, close-packed metal catalyst layer (10^{14} cm^{-2}) deposited on a high-aspect ratio surface (1000x). Electrode adsorption of oxalate is treated as being under diffusion control in this system, with oxalate adsorption ($A-oxa_{(ads)}$) at electrode active sites approximated as following a pseudo-first order dependence of oxalate concentration at the electrode surface (S.3). The rate constant for oxalate diffusion is calculated according to a modified, Fickian description of diffusive mean squared displacement:

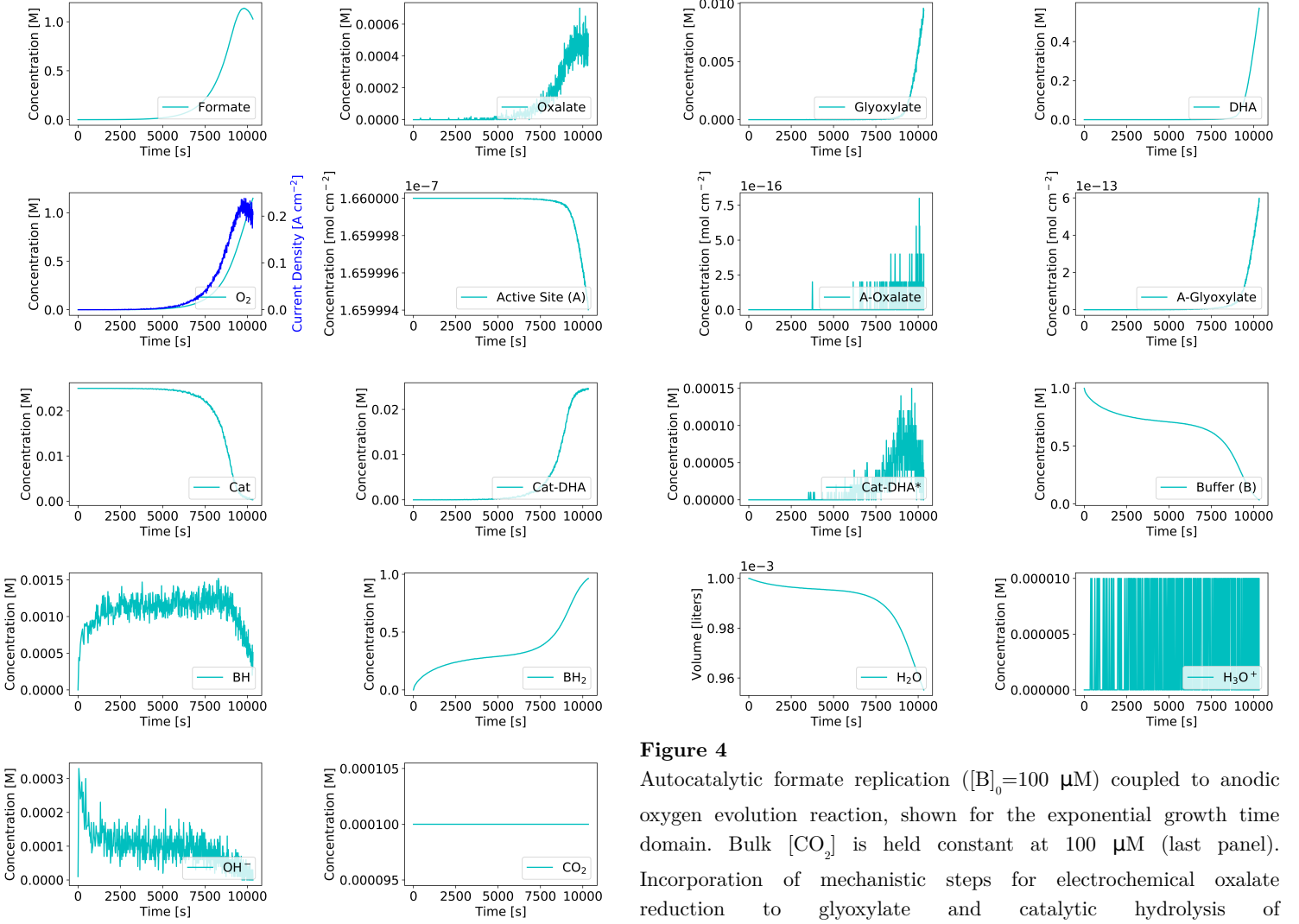


Figure 4

Autocatalytic formate replication ($[B]_0=100 \mu\text{M}$) coupled to anodic oxygen evolution reaction, shown for the exponential growth time domain. Bulk $[\text{CO}_2]$ is held constant at $100 \mu\text{M}$ (last panel). Incorporation of mechanistic steps for electrochemical oxalate reduction to glyoxylate and catalytic hydrolysis of glyoxylate/dihydroxyacetate (DHA) result in a slower catalytic cycle relative to the simplified base model.

$$\frac{1}{k_{diff}} \approx \frac{\langle x^2 \rangle}{2n\gamma_{mix}D} \quad \text{eq. 4b,}$$

where x is the diffusion length, D is the diffusion constant for the diffusing, and n gives the degrees of freedom in the system (taken as 3 for this system). Weighting the diffusion constant by the unitless term $\gamma_{mix} \geq 1$ is a phenomenological treatment, reflecting the increased effective diffusion constant of a species under mixing conditions, with $\gamma_{mix} = 1$ reflecting the case of pure diffusion in quiescent solutions. Simulation of the reaction volume as a 1 cm^3 reactor featuring a 1 cm^2 electrode, with an electrode surface region defined as a volume element projected within one bond length ($\sim 0.2 \text{ nm}$) from the electrode surface, yields an average distance of $x = 0.5 \text{ cm}$ for bulk to surface-region diffusion. From these parameters, a diffusion rate constant $k_{diff} = 2 \times 10^{-4} \text{ s}^{-1}$ was calculated from the diffusion coefficient for oxalate ($1.03 \times 10^{-5} \text{ cm}^2 \text{ s}^{-1}$)³⁴. Explicit measurements of the glyoxylate diffusion coefficient in water were unavailable and were therefore approximated as the same order of magnitude of oxalate, at $10^{-5} \text{ cm}^2 \text{ s}^{-1}$. Previous work suggests glyoxylate, rather than its hydrate, dihydroxyacetate, as the species interacting

with the electrode, with an equilibrium process controlling their interconversion with a $K = 0.016^{24}$. Finally, we expand buffering equilibria to now include kinetics detailing the equilibrium speciation of dissolved inorganic carbon (DIC) species, H_2CO_3 , HCO_3^- and CO_3^{2-} into the simulation, with $[\text{HCO}_3^-] = 10 \text{ mM}$ at time zero.

Incorporation of the mass-transport of oxalate flux to the cathode surface results in a growth curve for formate that retains significant exponential character. This is evidenced by the formate growth subplot in Figure 4, which displays growth-limiting behavior at later times far below the ideal $B(t) \sim 2^t$ scaling of the idealized Basic System, as a result of depleted catalyst (Cat) (Figure 4, Cat subplot). Mass-transport constraints operate uniquely here, compared to a typical electrochemical

cell, where the electrode substrate is not under amplification. Here, the electrode substrate, oxalate, is also shown to be under nonlinear amplification (Figure 4, oxalate subplot). As a result, current draw from such a system is expected to increase in proportion to this amplifying substrate concentration. This is evidenced by the subplot for the anode reaction (Figure 4, O_2 subplot); taking the 1st derivative of oxygen concentration with time gives the electrolyzer current, which is also found to grow roughly as a time-exponential over the time scale examined.

In this work, oxalate reduction is treated as an electron transfer process with a rate controlled by a pseudo-first order dependence on oxalate adsorbate surface concentration, as suggested by Eggins^{30,35}:

$$r_2(t) = k_{ET}[\text{A-oxa}_{(ads)}](t) - k'_{ET}[\text{Gly-ads}](t) \quad \text{eq. 4c.}$$

Constants k_{ET} and k'_{ET} denote forward and reverse rate constants for the cathodic conversion of oxalate to glyoxylate using the traditional Butler-Volmer description for the electrode kinetics (S.3), simulated using values of $k_0 = 0.624 \text{ s}^{-1}$ ($j_0 = 10^{-5} \text{ A cm}^{-2} \times 1000x \text{ aspect ratio}$), $\alpha = 0.5$, and $T = 298 \text{ K}$. The overpotential (full cell), η , is taken to be -0.3 V . With these parameters, k_{ET} and k'_{ET} yield respective values of 215 and 0.002 s^{-1} for the cathode's forward and back reactions.

In reaction (3), hydrolysis of dihydroxyacetate is decomposed into three elementary steps, initiated through an equilibrium between bound and unbound substrate at a catalyst, in accordance with the rationale of activated complex formation in transition state theory:



Bracketed terms represent proposed transition state intermediates in the process of DHA/glyoxylate hydrolysis, with the species DHA^* representing the symmetric, pre-fission intermediate that is proposed to form prior before decaying to two equivalents of formate. It is noted that this process could also be initiated through glyoxylate-bound catalyst, which is then hydrated to form the species Cat-DHA. However, this alternative binding sequence does not affect the possibility of observing formate amplification.

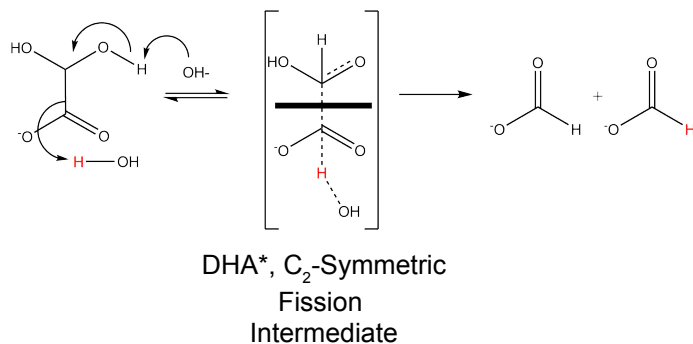


Figure 5

A putative reaction mechanism for step 3, the base-mediated fission of glyoxylate (as its hydrate dihydroxyacetate), to form two formate equivalents. Evolution of two molecules of formate arises from C-C bond breakage following deprotonation of the alcohol functionality, yielding a C_2 -symmetric transition state (DHA^*) that may decay into two molecules of formate.

Hydrolysis of DHA to give two molecules of formate represents a less-studied reaction but is again anticipated to be feasible (Figure 5). While this process is anticipated to be slow under ambient conditions, its possibility is evidenced by the presence of residual formate that can be eventually detected in a solution of 0.1 M glyoxylate in pH 9 1 M bicarbonate incubated at room temperature (S.11). Furthermore, preliminary experimental work has demonstrated the possibility of decomposing glyoxylate/DHA into formate (3) using the Mn-metallated N-macrocycle, 1,4,8,11-tetraazacyclotetradecane (Mn-Cyclam; S.11), an exploration inspired by the Mn-N(histidine) – mediated glyoxylate chemistry of glycolate oxidases³⁶. In this study, glyoxylate decay to two formate molecules is proposed as a process first-order with respect to a pre-fission intermediate, DHA* (Figure 5). Bond breakage across the intermediate’s horizontal mirror plane, σ_h (and a coincident C_2 axis), bisects the molecule, ultimately driving the evolution of two formate species according to the rate law:

$$r_3(t) = k_3[\text{DHA}^*](t) \quad \text{eq. 5.}$$

This rate law is informed by the likely mechanism for glyoxylate/DHA fission (Figure 5), which decomposes step 3 into a pre-equilibrium between glyoxylate and the DHA* and the first-order decay of DHA* to two formate molecules. The bar bisecting the proposed glyoxylate fission transition state denotes a plane of mirror symmetry accounting for the 2:1 formate:glyoxylate stoichiometry of this reaction. This reaction sequence has not been characterized, making selection of rates for simulation arbitrary. As a result, a range of rate-constants were tested for each reactions 3.1-3.3 to demonstrate that changing these rate constants over several orders of magnitude still permits formate amplification to proceed (S.7). Base case rate constants for the steps of DHA hydrolysis are as described in Table 2.

Fuel replication kinetics – ‘Full Mechanistic System,’ non-ideal replicator

Table 3 – Simulated ‘Full Mechanistic’ System

Reaction	Forward	Units	Reverse	Units	Ref
Autocatalytic System					
(1) $\text{HCO}_2^- + \text{CO}_2 + \text{H}_2\text{O} \rightarrow \text{C}_2\text{O}_4^{2-} + \text{H}_3\text{O}^+$					
1.1 $\text{H}_2\text{O} + \text{h}\nu \rightarrow \text{OH}^\cdot + \text{H}^\cdot$	0.045	s^{-1}	–	--	37
1.2 $\text{H}_2\text{O} + \text{h}\nu \rightarrow \text{e}^-_{(\text{aq})} + \text{H}_2\text{O}^+$	0.045	s^{-1}	–	--	37
1.3 $\text{HCO}_2^- + \text{H}^\cdot \rightarrow \text{CO}_2^\cdot + \text{H}_2$	2.2e8	$\text{M}^{-1} \text{s}^{-1}$	–	--	37
1.4 $\text{HCO}_2^- + \text{OH}^\cdot \rightarrow \text{CO}_2^\cdot + \text{H}_2\text{O}$	2.5e9	$\text{M}^{-1} \text{s}^{-1}$	–	–	37
1.5 $\text{HCO}_2^- + \text{e}^-_{(\text{aq})} \rightarrow \text{CO}_2^\cdot + \text{H}_2 + \text{OH}^\cdot$	1.0e6	$\text{M}^{-1} \text{s}^{-1}$	–	–	37
1.6 $\text{CO}_2 + \text{OH}^\cdot \rightarrow \text{HCO}_3^\cdot$	1.0e6	$\text{M}^{-1} \text{s}^{-1}$	–	–	37
1.7 $\text{CO}_2 + \text{H}^\cdot \rightarrow \text{COOH}^\cdot$	8.0e6	$\text{M}^{-1} \text{s}^{-1}$	–	–	37
1.8 $\text{COOH}^\cdot + \text{H}_2\text{O} \leftrightarrow \text{H}_3\text{O}^+ + \text{CO}_2^\cdot$	3.98e7	$\text{M}^{-1} \text{s}^{-1}$	1e9	$\text{M}^{-1} \text{s}^{-1}$	37
1.9 $\text{CO}_2 + \text{e}^-_{(\text{aq})} \rightarrow \text{CO}_2^\cdot$	7.7e9	$\text{M}^{-1} \text{s}^{-1}$	–	–	37
1.10 $2 \text{CO}_2^\cdot \rightarrow \text{C}_2\text{O}_4^{2-}$	1.0e9	$\text{M}^{-1} \text{s}^{-1}$	–	–	37
**Reactions 1.11 – 1.72 located in Supporting Information (S.17)					38,39
(2) $\text{C}_2\text{O}_4^{2-} + 2 \text{H}_2\text{O} \rightarrow \text{C}_2\text{H}_3\text{O}_4^- + \text{OH}^\cdot + 0.5 \text{O}_2$					
Cathode: $\text{C}_2\text{O}_4^{2-} + 3 \text{H}_2\text{O} + 2\text{e}^- \rightarrow \text{C}_2\text{H}_3\text{O}_4^- + 3 \text{OH}^\cdot$					
2.1 $\text{C}_2\text{O}_4^{2-}(\text{aq}) + \text{A} \leftrightarrow \text{A-C}_2\text{O}_4^{2-}(\text{ads})$	2.4	s^{-1}	0.8	s^{-1}	S.2
2.2 $\text{A-C}_2\text{O}_4^{2-}(\text{ads}) + 2 \text{H}_2\text{O} + 2\text{e}^- \leftrightarrow \text{A-C}_2\text{HO}_3^-(\text{ads}) + 3 \text{OH}^\cdot$	215	s^{-1}	0.002	s^{-1}	S.3

2.3 $A-C_2HO_3^-(ads) \leftrightarrow C_2HO_3^-(aq) + A$	0.8	s^{-1}	2.4	s^{-1}	S.2
2.4 $C_2HO_3^-(aq) + H_2O \leftrightarrow C_2H_3O_4^-(aq)$	70	s^{-1}	1.14	s^{-1}	24
Anode: $2 OH^- \leftrightarrow H_2O + 0.5 O_2 + 2e^-$	215	s^{-1}	0.002	s^{-1}	S.3
(3) $C_2H_3O_4^- + OH^- \rightarrow 2 HCO_2^- + H_2O$					
3.1 $C_2H_3O_4^- + Cat \leftrightarrow Cat-C_2H_3O_4^-$	100	$M^{-1} s^{-1}$	1	s^{-1}	S.7
3.2 $Cat-C_2H_3O_4^- + OH^- \leftrightarrow Cat-DHA^*$	1000	$M^{-1} s^{-1}$	1	s^{-1}	S.7
3.3 $Cat-DHA^* \rightarrow 2 HCO_2^- + Cat + H_2O$	10	s^{-1}	--	--	S.7
Buffering Equilibria					
Phosphate – Refer to reactions and values in Table (2).					
Carbonate – Refer to reactions and values in Table (2).					
Solvent Autoionization					
$H_3O^+ + OH^- \leftrightarrow 2 H_2O$	$k_w = 1.1e11$	$M^{-1} s^{-1}$	$k_w' = 1.1e-3$	s^{-1}	22

Having provided mechanistic routes for reactions 2 and 3, a fully mechanistic description for this autocatalytic system is now achieved by decomposing reaction 1 into 72 elementary radical reactions partly outlined in Table 3 and fully described in S.17. The initial step of base-mediated formate carboxylation to yield oxalate represents a thermodynamically challenging reaction, as it requires the C-C coupling of two low-energy reactants, formate and CO_2 . However, this net reaction has been realized in previous work by Getoff et. al³⁷, where it was demonstrated that vacuum UV (VUV) photolysis of CO_2 -saturated formate solutions yield oxalate as the chief carbon product, with quantum efficiency > 0.6 . It must be noted that the proposed mechanism of Getoff's VUV experiments invoked the dimerization of $COO \cdot^-$ radical intermediate, formed either through a formate or CO_2 precursor, as the rate-limiting step for oxalate synthesis. This would suggest that at long times, equimolar production of $COO \cdot^-$ from both formate and CO_2 becomes difficult. Given the exponential growth in formate concentration and the similar rate constants for the kinetically-limiting steps for $COO \cdot^-$ formation from CO_2 and formate, it would be expected that at long times, $COO \cdot^-$ intermediates derive almost exclusively from formate, rather than CO_2 , breaking the exponential scaling of formate accumulation and causing a plateau in replication rates. This is observed in Figure 6.

Radical speciation from the primary products of VUV photolysis in aqueous media forms an incredibly complex chain of reactions, which have been successfully modeled by Pastina et al, and later modified by Severin and coworkers^{38,39}; full incorporation of the mechanistic details of radical chemistry that are possible in water-based solutions are also included in the Full Mechanistic simulation (S.17). Simulated, steady-state VUV illumination with 124 nm photons, for this fully-described autocatalytic system yields a much shorter time base for formate evolution compared to the Basic and Partial simulations, as a result of the fast timescale of radical initiation reactions, with formate concentration reaching 2 M within 250 seconds (Figure 6, formate subplot). Formate evolution initiates with an exponential rise that quickly transitions towards hyperbolic growth, within the first 20 seconds of the simulation, as formate replication rapidly becomes limited by the rate of the radical processes responsible for oxalate evolution, whose concentration reaches a fast plateau within early stages of the reaction. Taking the derivative of anodic O_2 evolution in this system points to a current that rapidly stabilizes at ca. $3 A cm^{-2}$ over this period. Primary species evolved by VUV illumination of water are hydrogen radicals ($H \cdot$), hydroxide radicals ($OH \cdot$), and solvated electrons, ($e_{(aq)}^-$), which engage in secondary reactions; ultimately these reactions yield the $CO_2 \cdot^-$ intermediate from either CO_2 or formate (Table 3, reactions 1.3-1.5, 1.9; S.17)^{37,40,41}. The $CO_2 \cdot^-$

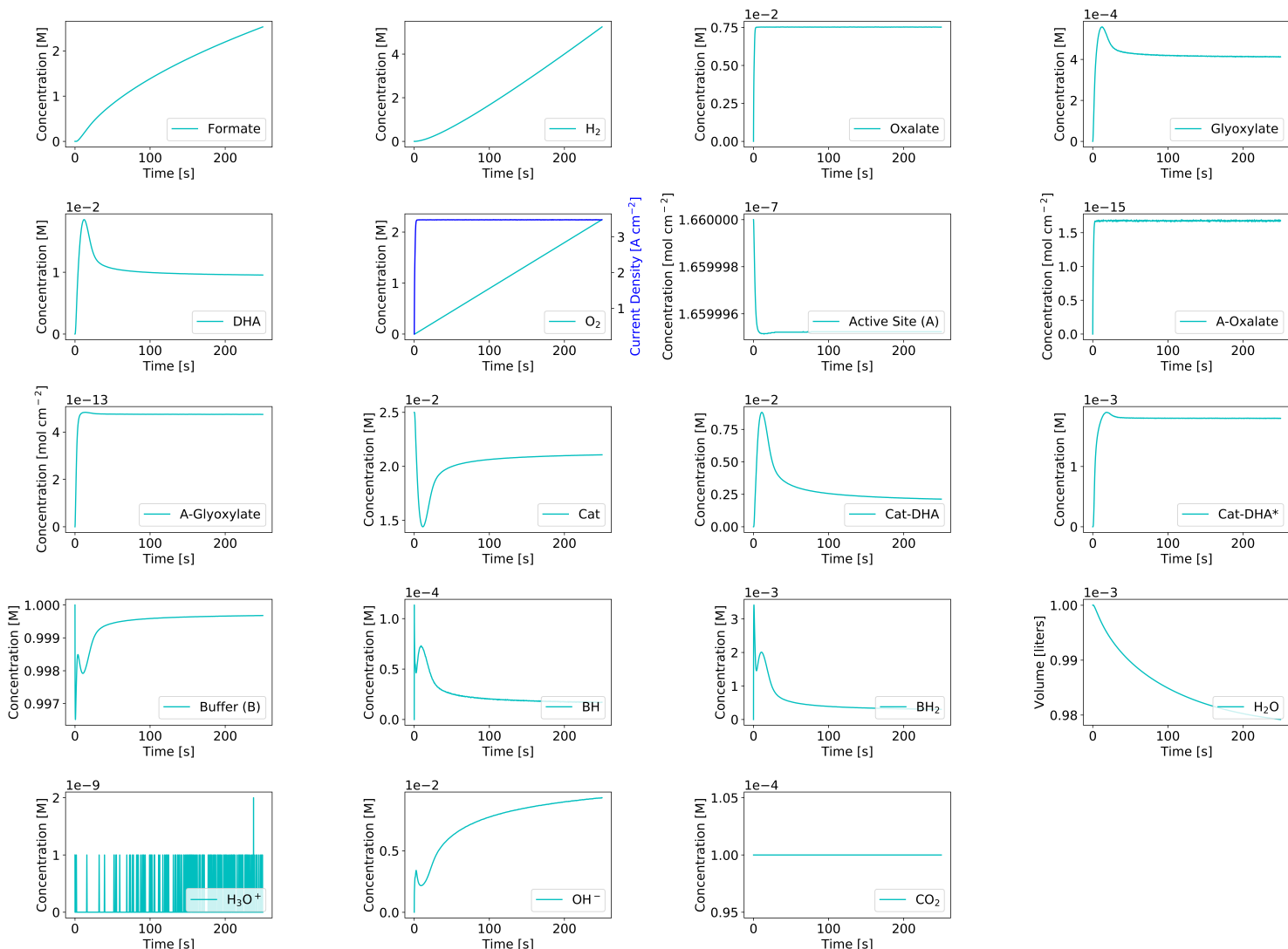


Figure 6: Behavior of the system with a mechanistic description for all steps, coupled to anodic OER. $B_0 = 100 \mu\text{M}$; $[\text{CO}_2]$ is held constant at $100 \mu\text{M}$. The simulation now incorporates radical-initiated, VUV-pumped mechanisms for formate carboxylation previously reported to drive the net conversion of formate to oxalate via formate carboxylation (step 1). VUV irradiation is at steady-state, with water consumption in the simulation mitigated through the incorporation of an H_2O reservoir feeding the reactor at a constant rate of 0.061 M s^{-1} .

intermediate then dimerizes to yield the oxalate intermediate^{37,40,41} (Table 3, reaction 1.10), thereby initiating reaction 2. The incorporation of these radical mechanisms into the overall scheme for formate amplification also result in the co-evolution of molecular hydrogen. As with formate and other cycle intermediates, the kinetics of H_2 evolution prove to be highly sensitive to rate constants driving these radical reactions, particularly the rate of OH^\cdot and H^\cdot radical initiation upon VUV irradiation. We find that at high illumination powers, it is possible to observe H_2 evolution following a weakly exponential trend at short timescales before transitioning to linear growth. Radical initiation under these conditions also results in the rapid accumulation of base (Figure 6, OH^- subplot). Transient VUV photoillumination was also explored, revealing a sharp, sigmoidal trend for formate evolution that is diagnostic of self-limiting autocatalysis, plateauing at 0.4 M formate. Concentrations of the key intermediates (oxalate, glyoxylate/dihydroxyacetic acid and their adsorbates) each exhibit sharp increases before rapidly decaying to zero. Significant base production and negligible proton evolution is observed upon integration of these radical

mechanisms for reaction step 1; as a result, there is virtually no consumption of the diprotic alkaline buffer used in these simulations, in contrast to the Basic and Partial simulation results. This is consistent with the large quantities of molecular hydrogen evolved through the radical chemistry. Fast sequences of proton-dependent, H[•] evolution and H-H annihilation yield H₂, providing a sink for protons that would otherwise consume buffer, as observed in the Partial Mechanistic System (Figure 6, H₂ subplot). The time-dependent energy efficiency for the Full Mechanistic System is calculated according to:

$$\eta_{real} = \frac{\sum_i B'_i(t) v_{rxn} \Delta G_{C,i}}{\int_0^t P_{VUV}(t) + i(t) \epsilon dt} \quad \text{eq. 6,}$$

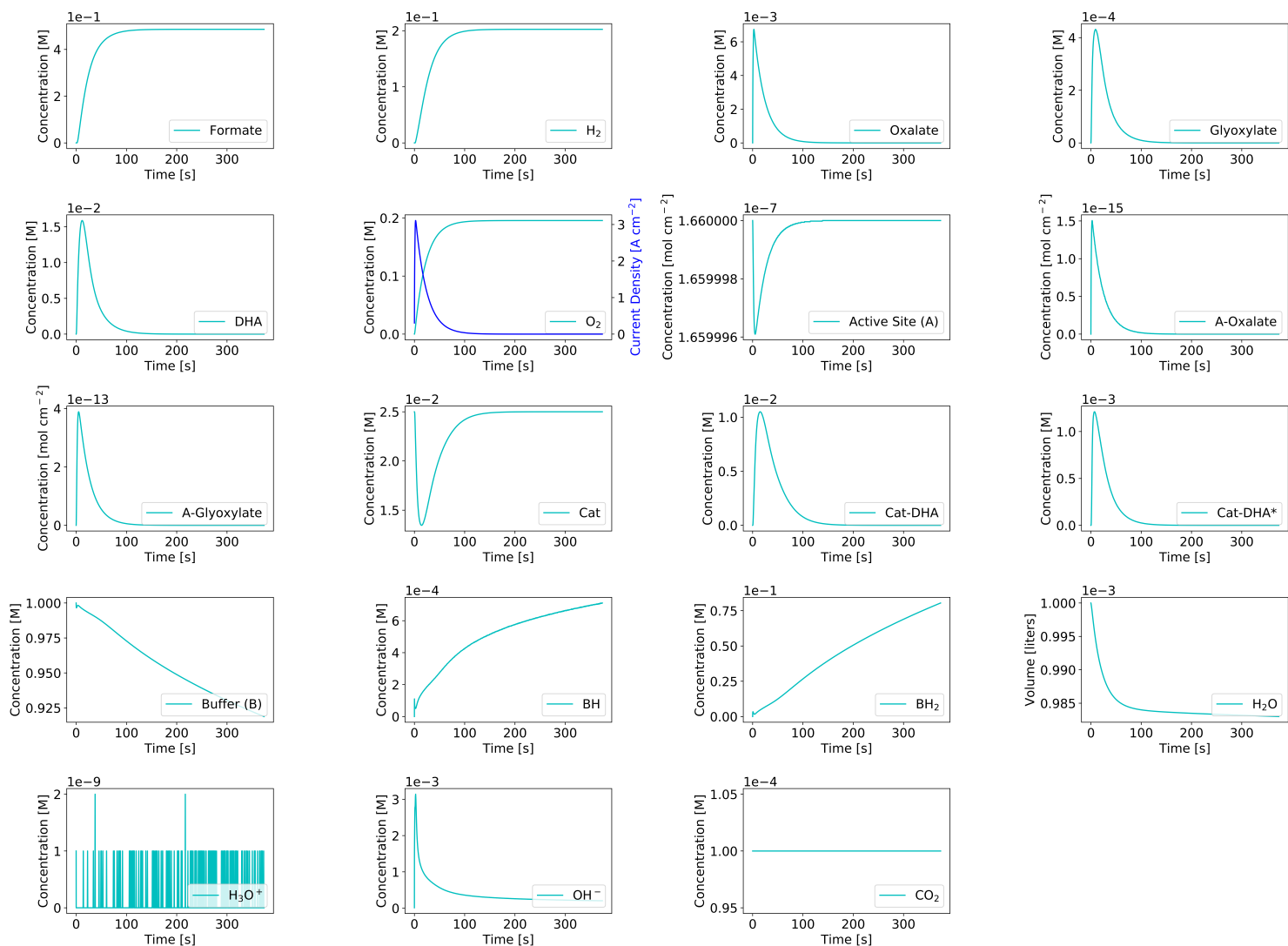


Figure 7 Behavior of the system with a mechanistic description for all steps, coupled to anodic OER, under transient VUV illumination (124 nm). $B_0 = 100 \mu\text{M}$; $[\text{CO}_2]$ is held constant at $100 \mu\text{M}$. The simulation now incorporates radical-initiated, VUV-pumped mechanisms for formate carboxylation previously reported to drive the net conversion of formate to oxalate via formate carboxylation (step 1).

where $B'_i(t)$ gives the time-dependent concentration of the i^{th} fuel component (here, formate, oxalate, glyoxylate/dihydroxyacetic acid and H_2 represent the main fuel components in the reaction volume with significant embodied energy content), v_{rxn} is the reaction volume, and $\Delta G_{c,i}$ is the free energy of combustion of the i^{th} fuel component, with values of -200.27, -273.63, -477.41, -624.43 and 237 kJ mol^{-1} for formate, oxalate, glyoxylate, dihydroxyacetate and hydrogen, respectively (S.3). P_{vuv} is the illumination power of the VUV source, $i(t)$ gives the electrolyzer current, and \mathcal{E} is the electrolyzer applied potential. Application of eq. 6 results in very low overall energy efficiencies for the VUV-coupled processes, peaking around 1.6% and 1.0% for steady-state and transient illumination cases, respectively. Losses here are dominated by the requirement for using high energy, 124 nm photons to drive water photolysis for radical generation, at a high power density (20.2 W cm^{-2} , S.9). This low efficiency highlights a significant opportunity for optimizing this cycle, if alternative routes for formate carboxylation that do not require the high-energy, intermediate step of H-O-H bond homolysis are realized.

The reports by Severin³⁹ and Pastina³⁸ demonstrate that the radical $\text{OH}\cdot$, $\text{H}\cdot$ and solvated electron species invoked by Getoff et al. as the key initiators of formate carboxylation in CO_2 -sparged aqueous solutions are also produced through the exposure of water to various nuclear decay sources, including proton and gamma ray emitters. This opens up the possibility of using the energy content of nuclear waste emissions as inputs for driving formate carboxylation in the cycle. However, successful observation of autocatalysis here requires that relative ratios of primary radical species produced by nuclear emissions (G values) fall within a band of radical product ratios similar to those measured by Getoff for VUV irradiation. However, substituting VUV irradiation in the simulation with values for primary radical generation in water characterizing 10 MeV proton emissions or gamma ray emissions result in linear formate evolution and failure to observe exponential growth in formate at any timescale (S.18). As a result, any implementation of nuclear decays as energy sources for formate carboxylation would need to be tuned appropriately, such that their G values for radical production approximate those of VUV radiation, possibly through the use of moderators for particulate emissions, or Compton scattering for attenuating gamma ray emissions. A minor nonlinear component is observed for H_2 yields for simulations of 10 MeV γ irradiation driving this system, before quickly transitioning to a linear growth trend at longer times (S.18).

Fuel replication thermodynamics

Replication energetics of the proposed cycle are thermodynamically uphill, requiring energetic inputs to push reaction equilibria in the direction of continuous formate evolution. Steps 1 and 2 are individually endothermic, with respective free energies of $+43 \text{ kJ mol}^{-1}$ for formate carboxylation⁴² and $+246 \text{ kJ mol}^{-1}$ for the two-electron reduction of oxalate to glyoxylate coupled to water oxidation, for an overall reaction $\Delta E^0 = 1.275 \text{ V}$ ($E^0 = -0.475 \text{ V}$ for the oxalate/glyoxylate half reaction)⁴². Hydrolytic fission of glyoxylate (via DHA) into two formate molecules (step 3) has a reported free energy change of -55 kJ mol^{-1} ⁴². Notably, the requirement of an exothermic bond-breakage for completing the cycle is consistent with the heat-dissipative nature of replicating systems⁴³. The

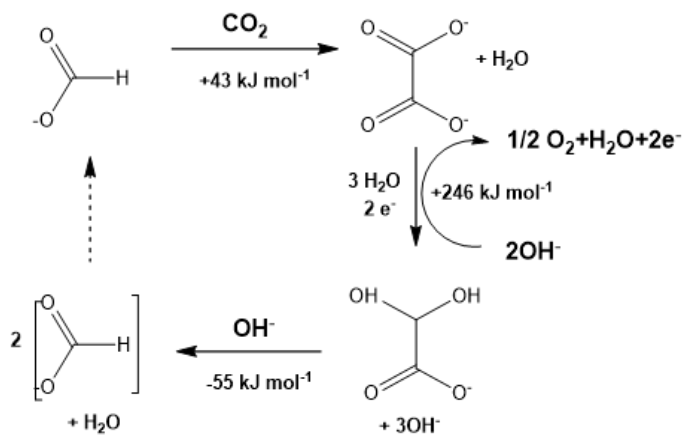


Figure 8

Thermodynamics of the proposed autocatalytic cycle. Conversion of oxalate to glyoxylate (in equilibrium with its hydrate, dihydroxyacetate, DHA) is shown using alkaline water oxidation as the complementary anodic half reaction. The process results in the net consumption of one water equivalent per cycle turnover.

energetics of a single reaction cycle represents the sum of these serial reaction steps, yielding a total free energy change of $\Delta G^o = +234 \text{ kJ mol}^{-1}$ per cycle iteration (Figure 8).

The proportionality between energy consumed and total product yield mandates that the rate of energy consumption also scale exponentially. As a result, in the limit of long times ($t \gg \tau$), sustaining the reaction will require an energy-dense source to maintain exponential fuel growth. In cases where the rate of energy supply (power density) of the source at time t is less than the rate of fuel production at time $t+1$, fuel production will begin to negatively deviate from the exponential growth observed at early times, plateauing at a rate (absent depletion or mass-transport limiting flux of key reactants or intermediates) limited by the source power density. For the case of undamped autocatalysis, exponential product growth can only be maintained for a cycle as the one proposed, if the rate of energy consumption (U_{tot}) by the fuel cycle is less than the peak power density of the source feeding the cycle (P):

$$\frac{dU_{tot}}{dt} < P \quad \text{eq. 7a.}$$

Approaching this limit, autocatalytic dampening occurs, resulting in a plateau of the reaction kinetics, bounded at P . Preferential kinetics relative to the case of steady-state operation occurs for the general condition where:

$$k_{linear} \prod_j [A_j]^{m_j} = \sum_i \frac{1}{\tau} \frac{\partial \Xi}{\partial t} B_0 (1 + \Xi_i(t))^{k_i t} \quad \text{eq. 7b.}$$

Here, k_{linear} is the overall rate constant of a comparable linear process, with a rate proportional to the steady-state concentrations of reactants A_j , of some arbitrary reaction order m_j . (i.e., electrochemical reduction of CO_2 to formate in 1:1 CO_2 : formate stoichiometry). Graphical representation of this is captured by Figure 9a.

A clear challenge exists for how to pair such a process for fuel production with a suitable energy source, as most power sources – such as sunlight – are only available at steady-state. Kinetic advantage can therefore only occur relative to some linear system, for cases where the time-averaged current density (or equivalently, time-averaged growth rate) of the autocatalytic system exceeds that of some steady-state linear case (eq. 7b). As a result, for all periods where autocatalysis operates below the rate of the power source, energy availability goes underutilized. At long times, for an optimized replication process only limited by energy availability (as opposed to reactants), the rate of fuel growth and energy consumed by autocatalysis will approach the limit allowed by the source’s maximum power density:

$$U_{tot} = v_{rxn} \sum_i \Delta G_{c,i} k_i \int_0^t \frac{\partial \Xi}{\partial t} B_{0,i} (1 + \Xi_i(t))^{k_i t} dt < \int_0^t P(t) dt \quad \text{eq. 7c,}$$

where the RHS of the inequality in eq. 7c is the source power density. The summation of the RHS captures the effect of integrating autocatalytic energy consumption over time for all fuel species i generated by the process.

Upper limits on achievable thermodynamic efficiency for autocatalytic replication can be estimated through a previously established framework for determining the lower bound of heat dissipation in a replicating system²⁸. Using this approach, any well-defined system of replication and its surrounding bath will be characterized by heat transfer that is a function of the replicator’s durability, defined as the inverse of its decay constant ($1/\delta$), internal entropy (ΔS_{int}), and growth rate constant (g_{max})⁴³. The internal entropy of a formate replicator may be calculated according to the Gibbs relation:

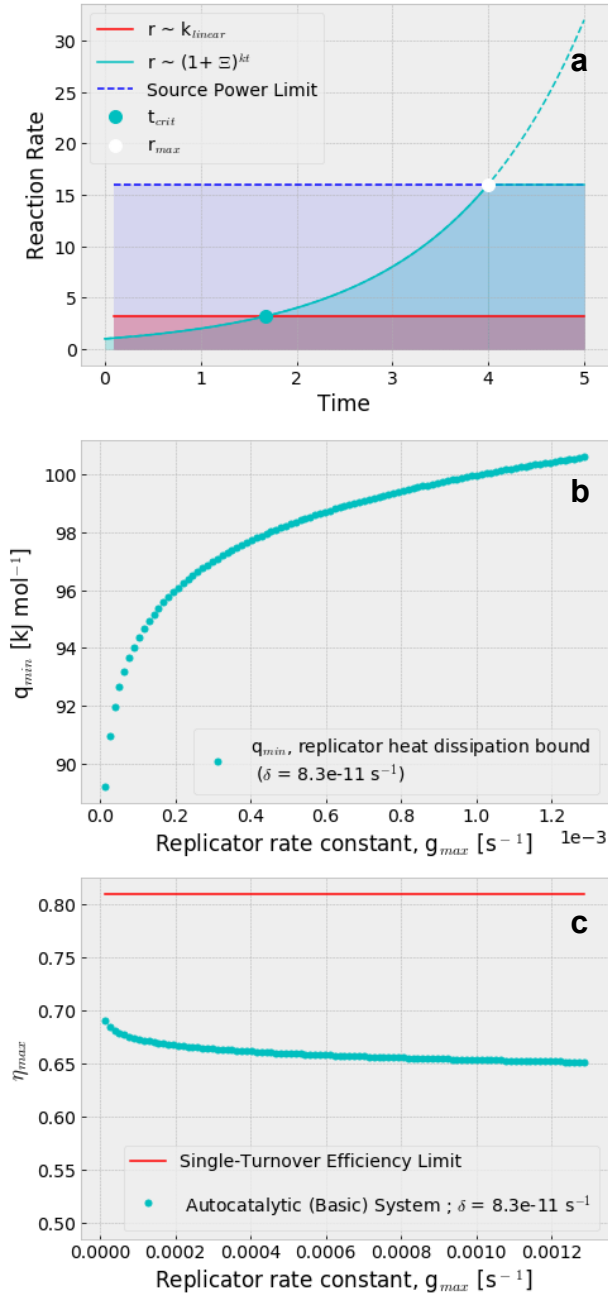


Figure 9 (a) A graphical representation of eqs. 6b & 6c. Rates of product evolution through autocatalysis ($\Xi = 1$) becomes preferential relative to linear catalysis for $t > t_{crit}$, with an intersection (cyan dot) described by equation 6b. (b) Lower bounds of replicator heat dissipation as a function of replicator rate constant, g_{max} . (c) Energy efficiency (η) scaling of g_{max} for formate replication (Basic System, cyan); $T = 298$ K. The thermodynamic limit for a single turnover (red) is calculated assuming a perfect cycle where energy losses only occur at the exothermic step of DHA bond fission to yield 2 formate equivalents (minimum input of 289 kJ mol⁻¹; maximum possible yield of 234 kJ mol⁻¹ as formate; $\eta_{max} = 0.81$).

$$\Delta S_{int} = \frac{\Delta H - \Delta G}{T} \quad \text{eq. 7d,}$$

where ΔH is the heat of formation of formic acid at (-425 kJ mol⁻¹ at 25 °C), ΔG is formic acid's free energy of formation (-361 kJ mol⁻¹ at 25 °C), and T_{sys} is the system temperature (298 K). Using these values with eq. 7d gives a value for ΔS_{int} -0.2 kJ mol⁻¹ K⁻¹ for a formate replicator at room temperature. Formate durability, $1/\delta$, may be estimated by considering known rates of spontaneous formate decomposition (to either CO₂ and hydrogen or carbon monoxide and water) under conditions relevant to those in the proposed autocatalytic cycle. Barham and coworkers have measured the Arrhenius behavior of formic acid decay constants, reporting a first-order decay constant of 700 s⁻¹ for decomposition of formic acid into CO and H₂O at 40 °C⁴⁴. Using these data, a decay constant $\delta = 8.3 \times 10^{-11}$ s⁻¹ at 25 °C could be extrapolated (S.10).

Applying these values for ΔS_{int} and δ to eq. 7e provides solution for q , the minimum waste heat transferred from the replicating system to the bath⁴³, for a given value of g_{max} :

$$q \geq k_B T \ln\left(\frac{g_{max} - \delta}{\delta}\right) - T \Delta S_{int} \quad \text{eq. 7e.}$$

Equation 7e estimates for the upper bound on thermodynamic efficiency and lower bound on generated waste heat (q) as a function of g_{max} for a formate replicator, as shown in Figures 9b and 9c. Critically, the calculated values for replication-dependent heat dissipation based on England's proof⁴³ quickly assume values with a minimum bound (~ 89 kJ mol⁻¹) within range of the exothermic step of glyoxylate/DHA bond fission (-55 kJ mol⁻¹) even before consideration of dissipative losses from reactions 1 and 2, suggesting the validity of England's framework. As replication rate constants increase, a greater fraction of this free energy release are shunted towards waste heat, which increases logarithmically with g_{max} (Figure 8b). As a result, the upper bound on energy efficiency for this process, as determined from the free energies of reaction for individual steps of the cycle shown in Figure 7, point to a thermodynamic limit of $\eta = 0.81$ per cycle (289 kJ mol⁻¹ total input per cycle; 234 kJ mol⁻¹ maximum available for conversion into formate). Calculating heat dissipation by eq. 7e allows determination

of a time-dependent efficiency (eqs. 7f, 7g) for formate replication. Using the definitions in eqs. 5c and 6b, the energy efficiency for an autocatalytic fuel cycle may be expressed as:

$$\eta = \frac{U(t)_{tot}}{\int P(t)dt} \tag{eq. 7f,}$$

with an upper efficiency bound of:

$$\eta = 1 - \frac{q}{\int P(t)dt} \tag{eq. 7g.}$$

Application of the replication rate constant extracted from formate growth simulated in the Basic System allows for determination of energy efficiency bounds of such fuel amplification processes. We take $g_{max} = 0.0013 \text{ s}^{-1}$, the value of the characteristic replication constant for the idealized growth kinetics of the Basic System. At 298 K, eqs. 7e, 7f and 7d yield an upper-bound efficiency of 65% (Figure 9c).

Discussion

Practical implications

There are three key advantages offered by the possibility of autocatalytic energy storage. First is the clear opportunity for building very fast systems for fuel generation, with rates that can scale exponentially with time. The doubling of product yield per cycle (in the ideal limit) for a 2^n autocatalytic system also means that fast overall rates of catalysis are possible even for systems featuring very slow catalytic rate constants; in most linear systems, this is difficult to achieve as rate scales only linearly with rate constants.

The second advantage is that autocatalytic systems will see their rate of fuel production (and so power consumption) increase until a plateau is reached at the power limit dictated by the source power density. That is, an optimized system exhibits adaptive behavior, with a peak rate that will continue increasing with time, so long as there is sufficient rate of energy input and substrate availability, to accommodate replicator growth. This property has the potential to be incredibly beneficial to electrolyzer performance, as these devices tend to have peak currents that are governed by mass-transport-limited substrate flux and availability. Replicating systems actually help mitigate such mass-transport limitations, as the primary reactant being consumed by the cycle is also evolved at successively higher concentrations by the same system. As a result, mass-transport issues should be far less pronounced when the electrode substrate concentration can actually increase with time. This differs significantly from a linearly-scaling system, where rates of power input, being generally invariant with time, will remain unchanged (as their substrate concentrations are constant). In the case of a typical electrolyzer, if the peak current of the system is far below that of the power source driving it, total power utilization only becomes possible with a sufficient multiple of electrolyzer units, with a sum power density of equaling P . This opens the possibility that for some arbitrarily large source power, two systems with comparable rate constants, one linear, one autocatalytic, it is possible to utilize the power source with a single autocatalytic electrolyzer, whereas multiple linear electrolyzers are required to utilize the source power density.

The third advantage of autocatalytic fuel generation is the fact that since the substrate and product are the same molecule, the system acts as a defacto concentrator for the target product. That is, it incorporates the functions of a fuel generator (such as an electrolyzer) and concentrator (a solvent still, etc.) into a single unit. The long-studied dependence between “fitness” of biological and chemical replicators and the ability of one replicator to dominate in number at long times, implies a potential role of autocatalysis in designing integrated systems for concentrating products as they are being generated^{10,43,45–47}. This fact is also evidenced by findings here, with

formate becoming a dominant product at long times relative to oxalate, glyoxylate and DHA replicators, despite the fact that all four (along with other intermediates in the Partial and Full Mechanistic systems) exhibit exponential growth behavior during the simulation time.

The decision to design an autocatalytic scheme around formate production was motivated by a number of critical factors. First, as the simplest liquid CO₂ reduction product, formate requires the least amount of chain buildup prior to the fission event that doubles product concentration. The reduced number of intermediate steps required for transforming formate precursors into C₂ compounds relative to other liquid fuel candidate schemes (S.12-S.14) also represent reduced opportunities for efficiency losses and the generation of side products that may interfere with the primary amplification reaction. In addition, formate/formic acid is a candidate hydrogen carrier, featuring a volumetric energy density similar to that of liquid hydrogen compressed to 700 atmospheres, a storage benchmark relevant to hydrogen deployment in automotive applications¹⁷. This, along with the mature state of hydrogen fuel cell technology and the significant advancements that have been made in processes catalyzing the dehydrogenation of formic acid to yield H₂^{48,49}, highlight the prospect of utilizing formate/formic acid as a carbon-neutral fuel or hydrogen storage reservoir. Such considerations motivated the particular focus on autocatalytic formate production by this study.

The ability of the proposed fuel cycle to generate exponential product yields, using exogenous substrate (CO₂) and reducing equivalents that are supplied at sufficient rates, demonstrates how such nonlinear energy storage schemes may be rationally constructed by integrating individual reactions displaying conventional, linear kinetics. In the domain of fuel production, this translates to an ability to rapidly store energy as a chemical fuel when the energy inputs are of sufficient power density. This property, taken with these simulation results, where nonlinear formate synthesis is dependent on an electrochemical reduction step, points to the possibility of driving this fuel cycle by coupling it to electrochemical/photoelectrochemical water oxidation. The potential for driving this cycle by coupling the oxalate reduction step to an anodic electrochemical process is supported by the long-established example of electrocatalytic oxalate reduction to glyoxylate over Pb cathodes reported by Tafel et al^{32,50}. Finally, the fact that these nonlinear kinetics result in the rapid consumption of water as formate accumulates, suggest that using autocatalytic reactions of the type proposed here will preclude their operation in batch, with the possible exception of operation at short timescales.

Aside from its more fundamental implications, fission-mediated autocatalysis may reduce barriers to industrial-scale production of fuel or commodity chemicals. Where fuel generation moves as an exponential function of time, such chemistries would significantly relax the capital requirements on plant size and process operation time needed to achieve profitable economies of scale. Perhaps most critical, is the fact that the concentrating nature of autocatalytic, fuel-forming reactions means that product yields at high concentrations are a natural consequence of autocatalytic behavior, potentially easing the requirement for downstream separations processes. Finally, as demonstrated tentatively through this study, combining this autocatalytic approach with preexisting radiochemistry may provide a route for utilizing the high energy content of nuclear wastes for energy storage applications, if the significant energy efficiency losses from primary radical generation can be mitigated.

Generalizing PCR for chemical energy storage

The ability to generate a fuel – indeed, any valuable product – as exponential functions of reaction time, carries clear implications in the domains of both fundamental chemical research and industrial production of chemical commodities. This study demonstrates that renewable fuel production, through a partly electrochemical process, can be implemented as a bond fission-dependent, autocatalytic reaction. The outcome of this study validates its underlying premise that general steps of primer annealing, nucleotide polymerization and ligation, and final dimer denaturation in PCR appear to be translatable to a broader set of chemical reactions. In particular, the chief constraints of the applicability of this scheme appear to be defined by only three broad requirements: (1) that the precursor/target can be built up into a molecule featuring a ground state or transition state that can be

represented as an dimer of the target product, (2) that the process of chain buildup include a balancing of redox equivalents, where the terminal hydrocarbon prior to binary fission has $2n$ reducing equivalents relative to the template/product oxidation state, and (3) this approximate dimer species can be decomposed to yield the target product in a 1:2 stoichiometry. The requirement of chain buildup prior to bond fission is reflected in prior work detailing the replication mechanisms of molecular fiber structures⁵¹, chimeric nucleobase/amino acid assemblies⁵² in origin-of-life research, and definitions of minimal self-replicating systems detailed by Paul et al⁵³. It is worth noting that constraints (1) and (2) are implicit statements about the molecular symmetries required of the pre-fission intermediate (here, the DHA* transition state), with the cycle’s ability to duplicate the starting template molecule suggested, in part, by the very structure of the pre-fission intermediate. Such symmetry requirements are again reminiscent of DNA, where the two-fold (anti)symmetry of the double helix was observed by Watson and Crick to suggest the very mechanism by which it could be replicated *in vivo*⁵⁴. While these three fundamental constraints of the proposed fuel cycle are relatively slack, suggesting a large theoretical space of target molecules that could be produced via PCR-type schemes of fission-dependent autocatalysis (S.12-S.14), realizing such processes in practice will be highly dependent on the nature of the individual reaction cycles under consideration. The significant challenges of realizing formate amplification indicated by this study suggest that engineering such reaction cycles for even marginally more complex molecular targets will be non-trivial.

Viewed from a different but equivalent perspective, the system described here bears directly upon Von Neumann’s *Theory of Self-Reproducing Automata*⁵⁵, which outlines the fundamental requirements of, and constraints on, self-replicating objects. Key are the requirements that a system capable of replication contain (1) an instruction set (2) building blocks and (3) a way of copying the instructions into the newly synthesized replicants, demands each satisfied by the system here. As a chemical system, the “instructions” are the system conditions for reactions 1, 2 and 3 that drive the interconversion of molecular intermediates; the fundamental building blocks at $t = 0$, are formate, CO₂, water, and electrons. The passage of these instructions into the newly replicated formate molecules are represented by the molecular bonds themselves comprising the molecular species, along with the system state.

The foundational logic behind 2^n product amplification should be extendable to the higher-order cases of ternary, quaternary, etc. fission, where even greater rates of product formation, scaling respectively as m^n (for $m = 3, 4$, etc.) would occur in the limits of perfect cycle selectivities. However, such cycles would carry even greater demands on the balancing of redox equivalents, catalytic selectivity and the extent of chain buildup into pre-fission intermediates of either m -fold symmetry or m repeating units. Given the clear difficulties of engineering high reaction selectivities for each of these steps in the simplest case of binary fission, realizing product amplification cycles featuring a higher exponent base will be even more challenging. To have any chance at demonstrating such schemes, mastery of the constituent linear chemical reactions comprising any such fission-coupled autocatalytic cycle – especially the elimination of side reactions – will be critical. Work here suggests that highest priority should be placed on optimization of reaction selectivity over rates, as even minority side reactions can result in the rapid accumulation of undesirable products, stalling the amplification process. Meanwhile, the demonstration of rapid formate yields, despite individual reaction steps featuring slow rate constants, suggests that the doubling effect per cycle allowed by the fission process may easily compensate for slow kinetics among any individual reaction steps with a molecularity of 1 or greater (any steps with a zeroth order rate constant would not be influenced by increases in substrate concentration).

In addition to autocatalytic cycling proceeding continuously – the general case explored by this manuscript – running the reaction as a sequence of discretized steps (as done in PCR), where the $n+1$ reaction step does not initiate until the completion of the n th step, represents a secondary configuration by which autocatalytic substrate production may be achieved. This type of discrete implementation would have the benefit of enabling separate control over CO₂ carboxylation and electrochemical steps, which, in the case of radical-mediated carboxylation, would minimize the possibility of chemical cross-talk between the intermediates generated by the independent

reaction sequences comprising the autocatalytic cycle. Here, the time for a cycle based on the mechanistic scheme used in this work is expressed as the sum of the reaction length for steps 1 through 3:

$$\tau = \frac{1}{k_{cycle}} = \lim_{A_1 \rightarrow 0} \frac{1}{k_1} \left(\frac{1}{A_1} - \frac{1}{A_{1,0}} \right) + \sum_2^j \lim_{A_j \rightarrow 0} \frac{1}{k_j} \ln \left(\frac{A_{j,0}}{A_j} \right) \quad \text{eq. 8a,}$$

assuming reactions that can be treated as sequential chemical transients with respect to substrate concentrations, A_j . The first limit expresses the time for transient substrate consumption for a 2nd order process, the case for the initial formate carboxylation reaction, where the rate-controlling step of CO_2^- radical dimerization to yield oxalate has a dependence expressed as:

$$r = k_{1.10}[\text{CO}_2^-]^2 \quad \text{eq. 8b,}$$

where $k_{1.10}$ is the rate constant for the CO_2^- dimerization (Table 3, reaction 1.10). The summation term generalizes the time for steps two and three to occur as a sequence, with the transient reaction times for each being represented by first-order decay kinetics, as given by the rate laws of their proposed rate-limiting processes. Here, terms k_1 and k_j give the respective 2nd and 1st order rate constants describing the relevant reaction step. Terms $A_{1,0}$ and $A_{j,0}$ denote the initial concentration of substrate A at the start of the j^{th} reaction, while terms A_t , A_j give the concentration of substrate at time t . Evaluating equations 1b and 1c using the calculated τ for the discontinuous case allows for determination of formate growth in the limit of discrete cycling.

Technical barriers to implementation

Despite its conceptual simplicity and the standing precedent set by PCR, significant technical barriers lie in demonstrating the autocatalytic formate cycle described here. One of the key intermediates, glyoxylate, may also undergo decomposition through UV photochemistry⁵⁶, although this has been reported at timescales far longer than the reaction cycle times considered here. In the process investigated here, the high energy photons used for photolysis represent the main point of efficiency losses calculated for the Full Mechanistic System. It is clear that achieving autocatalysis with high energy efficiency will require a movement way from this photolytic strategy. Alternatively, work on non-equilibrium replication has demonstrated how transient energy inputs can improve replication efficiency, opening the possibility of utilizing pulsed VUV sources to improve replication efficiency, if pulse times are suitably coordinated with timescales of replication⁵⁷. The application of primary radical production through voltammetric methods, such as electrochemical Fenton reactions for OH^\bullet generation, may also provide avenues for facilitating reaction 1 with fewer energetic losses⁵⁸. Finally, it is critical to note that, as with any model, this simulation assumes many chemical intermediates and processes do not cross-interact and furthermore, cannot account for any unique impact that a potential but unknown chemical side product might have on the overall reaction chemistry.

Development of a selective catalyst for glyoxylate/DHA decomposition into two formate equivalents will be essential. Currently there has been no underlying rationale for why such a reaction would be pursued in the first place; such rationale are now put forth by this paper. Ongoing experimental work will act as a follow-on to this theoretical manuscript, and characterize the kinetics and selectivity of the Mn-Cyclam catalyst under exploration for driving reaction 3 in the proposed cycle. In particular, this future work will aim to resolve the exact stoichiometry of formate evolved with respect to hydrolyzed glyoxylate, as it is also possible that, like in the Mn-bearing glyoxylate oxidase, Mn-Cyclam catalyzes reactions in which glyoxylate is decomposed into 1 equivalent of CO_2 and formate through Mn redox-disproportionation, rather than two formate equivalents.

For future efforts to realize this fuel cycle, the most daunting problem is likely the high selectivity required for each reaction step, to avoid amplifying side-products. In addition, the challenge of realizing a fuel cycle as this one is compounded by the particular difficulty of facilitating reaction 1, which requires the carboxylation of formate; here the reactants, CO₂ and formate, each constitute low-energy compounds that are generally difficult to chemically activate. Work by Getoff et al. has shown the possibility of realizing photochemical carboxylation of formate to yield oxalate through photochemical radical mechanisms with high quantum efficiencies in the vacuum ultraviolet regime, suggesting radical-dependent paths for realizing reaction 1 in practice³⁷. The requirement of a high reaction specificity is reminiscent of the role played by DNA polymerase III in PCR chemistry, where the enzyme catalyzes rapid nucleotide incorporation ($k_{\text{cat}} \sim 1000 \text{ s}^{-1}$) into the duplicate strand with an error rate of order 1 in 1 million (excluding the additional fidelity provided by DNAP's exonuclease activity)^{59,60}. This high specificity is essential for DNA polymerase III; without it, the exponential nature of DNA replication would lead to the fast accumulation of random errors (mutations) within genetic material, impacting biochemical functions in living organisms. Indeed, the exploitation of low-fidelity DNA polymerases in error-prone PCR are used for the rapid generation of random mutant libraries *in vitro*, despite the error rates of promiscuous DNA polymerases being on the order of just tenths of a percent, demonstrating how even side reactions with relatively low rate constants may rapidly accumulate side products under the amplified scaling of nonlinear reaction kinetics⁶¹.

Conclusions

The extension of nonlinear chemical kinetics to reaction schemes for sustainable fuel production carries a significant and largely unexplored potential to reshape our conceptual approaches to the design of renewable energy systems. In particular, chemical processes deploying the essential reaction characteristics of PCR - particularly the property of autocatalytic cycling that incorporates a molecular fission step, may reorient our design focus entirely. Such processes have the attributes necessary for enabling exponential yields of fuel as a function of time, growth relations that dwarf the conventional, linear schemes characterizing the vast majority of work done in the field of renewable chemicals and fuel production. Furthermore, because these autocatalytic schemes also result in exponential growth for cycle intermediates, such approaches also open the possibility of generating significant quantities of the more reduced/longer-chain compounds that are generated prior to molecular bond fission, provided that the relative rates of the constituent reactions can be suitably controlled. Such an approach would be immensely powerful if successfully implemented, carrying with it significant downstream economic implications on issues spanning fuel scarcity to the capital demands on plant size for production scale-up. On this latter subject, a fuel production facility exploiting autocatalytic fission kinetics could possibly result in a breakage in the traditional, linear correlations linking plant size and production capacity, with a process exhibiting exponential fuel yields enabling similar output for a production plant of much smaller size.

Practical application of autocatalytic molecular fission will require surmounting significant technical challenges. In particular, high specificity catalysts will be needed to drive the individual reaction steps comprising such chemical cycles, which remain a broad challenge in chemistry. In the specific fuel cycle studied here, rate constants for side product evolution (assuming first-order kinetics) must be reduced to approximately $\sim 10^{-5}$ that of the most chemically-demanding step (reaction 1), a level of fidelity closer to the specificity displayed by natural enzymes, rather than typical inorganic catalysts. While reactions 2 and 3 demand far lower catalytic specificities for the reaction to proceed, the particulars of these reactions, which involve the optimization of oxalate reduction to glyoxylate in the case of reaction 2, and hydrolytic C-C bond breakage in reaction 3, also mark non-trivial challenges. However, resolving these problems will open a path towards rethinking chemical energy storage - and chemical reactions more generally - in terms of nonlinear processes and their potential benefits relative to traditional, linear reaction schemes.

Materials and Methods

Materials and Methods can be found in the Supporting Information.

References

- (1) Luria, S. E.; Delbrück, M. Mutations of Bacteria From Virus Sensitivity to Virus Resistance. *Genetics* **1943**, *28* (6), 491–511. <https://doi.org/10.1093/genetics/28.6.491>.
- (2) Mullis, K. B.; Faloona, F. A. [21] Specific Synthesis of DNA in Vitro via a Polymerase-Catalyzed Chain Reaction. In *Methods in Enzymology*; Recombinant DNA Part F; Academic Press, 1987; Vol. 155, pp 335–350. [https://doi.org/10.1016/0076-6879\(87\)55023-6](https://doi.org/10.1016/0076-6879(87)55023-6).
- (3) Gordon, J. P.; Zeiger, H. J.; Townes, C. H. The Maser---New Type of Microwave Amplifier, Frequency Standard, and Spectrometer. *Phys. Rev.* **1955**, *99* (4), 1264–1274. <https://doi.org/10.1103/PhysRev.99.1264>.
- (4) Meitner, L.; Frisch, O. R. Disintegration of Uranium by Neutrons: A New Type of Nuclear Reaction. *Nature* **1939**, *143* (3615), 239–240. <https://doi.org/10.1038/143239a0>.
- (5) Improvements in or Relating to the Transmutation of Chemical Elements. GB630726 (A), March 30, 1936. https://worldwide.espacenet.com/publicationDetails/biblio?FT=D&date=19360330&DB=&locale=en_EP&CC=GB&NR=630726A&KC=A&ND=1 (accessed 2022-10-07).
- (6) Rayder, T. M.; Adillon, E. H.; Byers, J. A.; Tsung, C.-K. A Bioinspired Multicomponent Catalytic System for Converting Carbon Dioxide into Methanol Autocatalytically. *Chem* **2020**, *6* (7), 1742–1754. <https://doi.org/10.1016/j.chempr.2020.04.008>.
- (7) Vorotyntsev, M. A.; Antipov, A. E.; Konev, D. V. Bromate Anion Reduction: Novel Autocatalytic (EC^o) Mechanism of Electrochemical Processes. Its Implication for Redox Flow Batteries of High Energy and Power Densities. *Pure Appl. Chem.* **2017**, *89* (10), 1429–1448. <https://doi.org/10.1515/pac-2017-0306>.
- (8) Jin, F.; Zeng, X.; Liu, J.; Jin, Y.; Wang, L.; Zhong, H.; Yao, G.; Huo, Z. Highly Efficient and Autocatalytic H₂O Dissociation for CO₂ Reduction into Formic Acid with Zinc. *Sci. Rep.* **2014**, *4* (1), 4503. <https://doi.org/10.1038/srep04503>.
- (9) Semenov, S. N.; Kraft, L. J.; Ainla, A.; Zhao, M.; Baghbanzadeh, M.; Campbell, V. E.; Kang, K.; Fox, J. M.; Whitesides, G. M. Autocatalytic, Bistable, Oscillatory Networks of Biologically Relevant Organic Reactions. *Nature* **2016**, *537* (7622), 656–660. <https://doi.org/10.1038/nature19776>.
- (10) Morrow, S. M.; Colomer, I.; Fletcher, S. P. A Chemically Fuelled Self-Replicator. *Nat. Commun.* **2019**, *10* (1), 1011. <https://doi.org/10.1038/s41467-019-08885-9>.
- (11) Tham, Y. J.; He, X.-C.; Li, Q.; Cuevas, C. A.; Shen, J.; Kalliokoski, J.; Yan, C.; Iyer, S.; Lehmusjärvi, T.; Jang, S.; Thakur, R. C.; Beck, L.; Kemppainen, D.; Olin, M.; Sarnela, N.; Mikkilä, J.; Hakala, J.; Marbouti, M.; Yao, L.; Li, H.; Huang, W.; Wang, Y.; Wimmer, D.; Zha, Q.; Virkanen, J.; Spain, T. G.; O'Doherty, S.; Jokinen, T.; Bianchi, F.; Petäjä, T.; Worsnop, D. R.; Mauldin, R. L.; Ovadnevaite, J.; Ceburnis, D.; Maier, N. M.; Kulmala, M.; O'Dowd, C.; Maso, M. D.; Saiz-Lopez, A.; Sipilä, M. Direct Field Evidence of Autocatalytic Iodine Release from Atmospheric Aerosol. *Proc. Natl. Acad. Sci.* **2021**, *118* (4). <https://doi.org/10.1073/pnas.2009951118>.
- (12) Soai, K.; Shibata, T.; Morioka, H.; Choji, K. Asymmetric Autocatalysis and Amplification of Enantiomeric Excess of a Chiral Molecule. *Nature* **1995**, *378* (6559), 767–768. <https://doi.org/10.1038/378767a0>.
- (13) Semenov, S. N.; Belding, L.; Cafferty, B. J.; Mousavi, M. P. S.; Finogenova, A. M.; Cruz, R. S.; Skorb, E. V.; Whitesides, G. M. Autocatalytic Cycles in a Copper-Catalyzed Azide–Alkyne Cycloaddition Reaction. *J. Am. Chem. Soc.* **2018**, *140* (32), 10221–10232. <https://doi.org/10.1021/jacs.8b05048>.
- (14) Ferrer Flegeau, E.; Bruneau, C.; Dixneuf, P. H.; Jutand, A. Autocatalysis for C–H Bond Activation by Ruthenium(II) Complexes in Catalytic Arylation of Functional Arenes. *J. Am. Chem. Soc.* **2011**, *133* (26), 10161–10170. <https://doi.org/10.1021/ja201462n>.

- (15) Bohner, B.; Schuszter, G.; Nakanishi, H.; Zámbo, D.; Deák, A.; Horváth, D.; Tóth, Á.; Lagzi, I. Self-Assembly of Charged Nanoparticles by an Autocatalytic Reaction Front. *Langmuir* **2015**, *31* (44), 12019–12024. <https://doi.org/10.1021/acs.langmuir.5b03219>.
- (16) Yu, J.; Ma, E.; Ma, T. Exponential Energy Harvesting through Repetitive Reconfigurations of a System of Capacitors. *Commun. Phys.* **2018**, *1* (1), 1–10. <https://doi.org/10.1038/s42005-018-0010-y>.
- (17) Eppinger, J.; Huang, K.-W. Formic Acid as a Hydrogen Energy Carrier. *ACS Energy Lett.* **2017**, *2* (1), 188–195. <https://doi.org/10.1021/acsenergylett.6b00574>.
- (18) Cobbs, G. Stepwise Kinetic Equilibrium Models of Quantitative Polymerase Chain Reaction. *BMC Bioinformatics* **2012**, *13*, 203. <https://doi.org/10.1186/1471-2105-13-203>.
- (19) Hanopolskyi, A. I.; Smaliak, V. A.; Novichkov, A. I.; Semenov, S. N. Autocatalysis: Kinetics, Mechanisms and Design. *ChemSystemsChem* **2021**, *3* (1), e2000026. <https://doi.org/10.1002/syst.202000026>.
- (20) Schuster, P. What Is Special about Autocatalysis? *Monatshefte Für Chem. - Chem. Mon.* **2019**, *150* (5), 763–775. <https://doi.org/10.1007/s00706-019-02437-z>.
- (21) Blokhuis, A.; Lacoste, D.; Nghe, P. Universal Motifs and the Diversity of Autocatalytic Systems. *Proc. Natl. Acad. Sci.* **2020**, *117* (41), 25230–25236. <https://doi.org/10.1073/pnas.2013527117>.
- (22) Natzle, W. C.; Moore, C. B. Recombination of Hydrogen Ion (H⁺) and Hydroxide in Pure Liquid Water. *J. Phys. Chem.* **1985**, *89* (12), 2605–2612. <https://doi.org/10.1021/j100258a035>.
- (23) Gillespie, D. T. A General Method for Numerically Simulating the Stochastic Time Evolution of Coupled Chemical Reactions. *J. Comput. Phys.* **1976**, *22* (4), 403–434. [https://doi.org/10.1016/0021-9991\(76\)90041-3](https://doi.org/10.1016/0021-9991(76)90041-3).
- (24) Eggins, B. R.; McMullan, E. A. Kinetic Control and Adsorption in the Voltammetry of Glyoxylate. *Collect. Czechoslov. Chem. Commun.* **1989**, *54* (10), 2631–2637. <https://doi.org/10.1135/cccc19892631>.
- (25) Zumdahl, S. S. *Chemical Principles*, 5th edition.; Houghton Mifflin: Boston, 2004.
- (26) Dreybrodt, W.; Lauckner, J.; Zaihua, L.; Svensson, U.; Buhmann, D. The Kinetics of the Reaction CO₂ + H₂O → H⁺ + HCO₃[−] as One of the Rate Limiting Steps for the Dissolution of Calcite in the System H₂O-CO₂-CaCO₃. *Geochim. Cosmochim. Acta* **1996**, *60* (18), 3375–3381. [https://doi.org/10.1016/0016-7037\(96\)00181-0](https://doi.org/10.1016/0016-7037(96)00181-0).
- (27) Ho, C.; Sturtevant, J. M. The Kinetics of the Hydration of Carbon Dioxide at 25°. *J. Biol. Chem.* **1963**, *238* (10), 3499–3501. [https://doi.org/10.1016/S0021-9258\(18\)48695-4](https://doi.org/10.1016/S0021-9258(18)48695-4).
- (28) Mitchell, M. J.; Jensen, O. E.; Cliffe, K. A.; Maroto-Valer, M. M. A Model of Carbon Dioxide Dissolution and Mineral Carbonation Kinetics. *Proc. R. Soc. Lond. Math. Phys. Eng. Sci.* **2010**, *466* (2117), 1265–1290. <https://doi.org/10.1098/rspa.2009.0349>.
- (29) Wang, X.; Conway, W.; Burns, R.; McCann, N.; Maeder, M. Comprehensive Study of the Hydration and Dehydration Reactions of Carbon Dioxide in Aqueous Solution. *J. Phys. Chem. A* **2010**, *114* (4), 1734–1740. <https://doi.org/10.1021/jp909019u>.
- (30) Eggins, B. R.; Ennis, C.; McConnell, R.; Spence, M. Improved Yields of Oxalate, Glyoxylate and Glycolate from the Electrochemical Reduction of Carbon Dioxide in Methanol. *J. Appl. Electrochem.* **1997**, *27* (6), 706–712. <https://doi.org/10.1023/A:1018444022321>.
- (31) Eggins, B. R.; Ennis, C.; McConnell, R.; Spence, M. Improved Yields of Oxalate, Glyoxylate and Glycolate from the Electrochemical Reduction of Carbon Dioxide in Methanol. *J. Appl. Electrochem.* **1997**, *27* (6), 706–712. <https://doi.org/10.1023/A:1018444022321>.
- (32) Tafel, J.; Friedrichs, G. Elektrolytische Reduction von Carbonsäuren Und Carbonsäureestern in Schwefelsaurer Lösung. *Berichte Dtsch. Chem. Ges.* **1904**, *37* (3), 3187–3191. <https://doi.org/10.1002/cber.190403703116>.
- (33) Krupka, R. M.; Towers, G. H. N. Small-Scale Preparation of Glyoxylic Acid Labelled with Carbon-14. *Nature* **1958**, *181* (4605), 335. <https://doi.org/10.1038/181335a0>.

- (34) Šljukić, B.; Baron, R.; Compton, R. G. Electrochemical Determination of Oxalate at Pyrolytic Graphite Electrodes. *Electroanalysis* **2007**, *19* (9), 918–922. <https://doi.org/10.1002/elan.200703852>.
- (35) Eggins, B. R.; Brown, E. M.; McNeill, E. A.; Grimshaw, J. Carbon Dioxide Fixation by Electrochemical Reduction in Water to Oxalate and Glyoxylate. *Tetrahedron Lett.* **1988**, *29* (8), 945–948. [https://doi.org/10.1016/S0040-4039\(00\)82489-2](https://doi.org/10.1016/S0040-4039(00)82489-2).
- (36) Yokota, A.; Kawabata, A.; Kitaoka, S. Mechanism of Glyoxylate Decarboxylation in the Glycolate Pathway in *Euglena Gracilis* Z: Participation of Mn²⁺-Dependent NADPH Oxidase in Chloroplasts. *Plant Physiol.* **1983**, *71* (4), 772–776. <https://doi.org/10.1104/pp.71.4.772>.
- (37) Getoff, N.; Schenck, G. O. Primary Products of Liquid Water Photolysis at 1236, 1470 and 1849 Å. *Photochem. Photobiol.* **1968**, *8* (3), 167–178. <https://doi.org/10.1111/j.1751-1097.1968.tb05859.x>.
- (38) Pastina, B.; LaVerne, J. A. Effect of Molecular Hydrogen on Hydrogen Peroxide in Water Radiolysis. *J. Phys. Chem. A* **2001**, *105* (40), 9316–9322. <https://doi.org/10.1021/jp012245j>.
- (39) Domnanich, K. A.; Severin, G. W. A Model for Radiolysis in a Flowing-Water Target during High-Intensity Proton Irradiation. *ACS Omega* **2022**, *7* (29), 25860–25873. <https://doi.org/10.1021/acsomega.2c03540>.
- (40) Getoff, N. CO₂ and CO Utilization: Radiation-Induced Carboxylation of Aqueous Chloroacetic Acid to Malonic Acid. *Radiat. Phys. Chem.* **2003**, *67* (5), 617–621. [https://doi.org/10.1016/S0969-806X\(03\)00145-2](https://doi.org/10.1016/S0969-806X(03)00145-2).
- (41) Fjodorov, V. V.; Getoff, N. Radiation Induced Carboxylation of Methanol Under Elevated CO₂ Pressure. *Radiat. Phys. Chem.* **1983**, *22* (3–5), 841–848. [https://doi.org/10.1016/0146-5724\(83\)90103-6](https://doi.org/10.1016/0146-5724(83)90103-6).
- (42) Bar-Even, A.; Flamholz, A.; Noor, E.; Milo, R. Thermodynamic Constraints Shape the Structure of Carbon Fixation Pathways. *Biochim. Biophys. Acta BBA - Bioenerg.* **2012**, *1817* (9), 1646–1659. <https://doi.org/10.1016/j.bbabi.2012.05.002>.
- (43) England, J. L. Statistical Physics of Self-Replication. *J. Chem. Phys.* **2013**, *139* (12), 121923. <https://doi.org/10.1063/1.4818538>.
- (44) Barham, H. N.; Clark, L. W. The Decomposition of Formic Acid at Low Temperatures. *J. Am. Chem. Soc.* **1951**, *73* (10), 4638–4640. <https://doi.org/10.1021/ja01154a042>.
- (45) Plasson, R.; Brandenburg, A.; Jullien, L.; Bersini, H. Autocatalyses. *J. Phys. Chem. A* **2011**, *115* (28), 8073–8085. <https://doi.org/10.1021/jp110079p>.
- (46) Cortassa, S.; Aon, M. A.; Westerhoff, H. V. Linear Nonequilibrium Thermodynamics Describes the Dynamics of an Autocatalytic System. *Biophys. J.* **1991**, *60* (4), 794–803.
- (47) Ragazzon, G.; Prins, L. J. Energy Consumption in Chemical Fuel-Driven Self-Assembly. *Nat. Nanotechnol.* **2018**, *13* (10), 882–889. <https://doi.org/10.1038/s41565-018-0250-8>.
- (48) Rees, N. V.; Compton, R. G. Sustainable Energy: A Review of Formic Acid Electrochemical Fuel Cells. *J. Solid State Electrochem.* **2011**, *15* (10), 2095–2100. <https://doi.org/10.1007/s10008-011-1398-4>.
- (49) Navlani-García, M.; Mori, K.; Kuwahara, Y.; Yamashita, H. Recent Strategies Targeting Efficient Hydrogen Production from Chemical Hydrogen Storage Materials over Carbon-Supported Catalysts. *NPG Asia Mater.* **2018**, *10* (4), 277. <https://doi.org/10.1038/s41427-018-0025-6>.
- (50) Pickett, D. J.; Yap, K. S. A Study of the Production of Glyoxylic Acid by the Electrochemical Reduction of Oxalic Acid Solutions. *J. Appl. Electrochem.* **1974**, *4* (1), 17–23. <https://doi.org/10.1007/BF00615902>.
- (51) Colomb-Delsuc, M.; Mattia, E.; Sadownik, J. W.; Otto, S. Exponential Self-Replication Enabled through a Fibre Elongation/Breakage Mechanism. *Nat. Commun.* **2015**, *6* (1), 7427. <https://doi.org/10.1038/ncomms8427>.
- (52) Liu, B.; Pappas, C. G.; Ottel , J.; Schaeffer, G.; Jurissek, C.; Pieters, P. F.; Altay, M.; Marić, I.; Stuart, M. C. A.; Otto, S. Spontaneous Emergence of Self-Replicating Molecules Containing Nucleobases and Amino Acids. *J. Am. Chem. Soc.* **2020**, *142* (9), 4184–4192. <https://doi.org/10.1021/jacs.9b10796>.

- (53) Paul, N.; Joyce, G. F. Minimal Self-Replicating Systems. *Curr. Opin. Chem. Biol.* **2004**, *8* (6), 634–639. <https://doi.org/10.1016/j.cbpa.2004.09.005>.
- (54) Watson, J. D.; Crick, F. H. C. Molecular Structure of Nucleic Acids: A Structure for Deoxyribose Nucleic Acid. *Nature* **1953**, *171* (4356), 737–738. <https://doi.org/10.1038/171737a0>.
- (55) Von Neumann, J.; Burks, A. W. (Arthur W. *Theory of Self-Reproducing Automata*; Urbana, University of Illinois Press, 1966.
- (56) Eugene, A. J.; Xia, S.-S.; Guzman, M. I. Aqueous Photochemistry of Glyoxylic Acid. *J. Phys. Chem. A* **2016**, *120* (21), 3817–3826. <https://doi.org/10.1021/acs.jpca.6b00225>.
- (57) Zhang, R.; Walker, D. A.; Grzybowski, B. A.; Olvera de la Cruz, M. Accelerated Self-Replication under Non-Equilibrium, Periodic Energy Delivery. *Angew. Chem. Int. Ed.* **2014**, *53* (1), 173–177. <https://doi.org/10.1002/anie.201307339>.
- (58) Chen, S.; Liang, S.; Huang, R.; Zhang, M.; Song, Y.; Zhang, Y.; Tao, S.; Yu, L.; Deng, D. Direct Electroconversion of Air to Nitric Acid under Mild Conditions. *Nat. Synth.* **2024**, *3* (1), 76–84. <https://doi.org/10.1038/s44160-023-00399-z>.
- (59) Freese, E. B.; Freese, E. On the Specificity of Dna Polymerase. *Proc. Natl. Acad. Sci.* **1967**, *57* (3), 650–657. <https://doi.org/10.1073/pnas.57.3.650>.
- (60) Alic, N.; Ayoub, N.; Landrieux, E.; Favry, E.; Baudouin-Cornu, P.; Riva, M.; Carles, C. Selectivity and Proofreading Both Contribute Significantly to the Fidelity of RNA Polymerase III Transcription. *Proc. Natl. Acad. Sci.* **2007**, *104* (25), 10400–10405. <https://doi.org/10.1073/pnas.0704116104>.
- (61) Leung, D. W. A Method for Random Mutagenesis of a Defined DNA Segment Using a Modified Polymerase Chain Reaction. *Technique* **1989**, *1*, 11–15.

Supporting Information

Computational methodology, simulation parameterization, kinetic schemes for Basic, Partial and Full systems, calculations of reaction selectivity, influence of rate constants, and reactivity under batch CO₂, Arrhenius extrapolation of formic acid decay constants, characterization of a glyoxylate (DHA) hydrolysis catalyst, examples of potential autocatalytic schemes for the production of methanol, dimethyl ether, carbon monoxide, and calculations for radiolysis-mediated formate carboxylation can be found in the Supporting Information.

Acknowledgments

This research was supported, in part, through the Office of Science of the U.S. Department of Energy under award number DE-FOA-0002676, an Early-Career Laboratory Directed Research and Development (LDRD) award through Lawrence Berkeley National Laboratory, funding through an LDRD from the LBNL Carbon Negative Initiative, and by the Clean Energy Manufacturing Program, U.S. Department of Energy, Office of Science, Office of Basic Energy Sciences, CSGB Division under contract no. DE-AC0205CH11231. The Kinetiscope simulation environment (<http://hinsberg.net/kinetiscope/index.html>) was used for all kinetics simulations presented in this work. The author thanks Melanie Pribisko Yen, Joseph Varghese, David Larson, Frances Houle, and Walter Drisdell for their helpful comments.

Dedication

This work is dedicated to Sophia and Samuel Agbo and in memory of Lovette Tochukwu Chiezey.

ORCID

Peter Agbo: 0000-0003-3066-4791

Correspondence

P.Agbo@lbl.gov

Competing Interests

This work relates to a Lawrence Berkeley National Laboratory invention disclosure by P.A.

Keywords: Autocatalysis, PCR, nonlinear dynamics, renewable energy, CO₂ conversion, replication, self-replication, gain, amplification, electrochemical storage

Self-replicating fuels via autocatalytic molecular bond fission

Peter Agbo^{1,2*}

Chemical Sciences Division¹, Molecular Biophysics & Integrated Bioimaging Division² Lawrence Berkeley National Laboratory, Berkeley CA 94720

*Corresponding author

PAgbo@LBL.gov

Supporting Information

Index

S.1 Computational and Quantitative Methods	S2
S.2 Unit Conversions Between Homogeneous and Heterogeneous Concentration	S7
S.3 Model Parameterization	S10
S.4 Product Selection as a Function of Rate Constants	S14
S.5 Effects of Side Reactions	S17
S.6 Effects of Batch CO ₂ Supply	S26
S.7 Rate Constant Sensitivity Analysis of Glyoxylate/DHA Fission	S27
S.8 Species Evolution Under VUV Pumping	S29
S.9 Energy Efficiency of Full Simulated System	S31
S.10 Arrhenius Extrapolation of Measured Formic Acid Decay	S32
S.11 Glyoxylate Hydrolysis Catalyst Characterizations	S33
S.12 Example CO Replication Scheme	S35
S.13 Example Syngas Replication Scheme	S36
S.14 Example Methanol Replication Scheme	S37
S.15 Simulation 1 – Basic System Setup	S38
S.16 Simulation 2 – Partial System Setup	S42
S.17 Simulation 3 – Full System Setup	S46
S.18 Radiolysis Calculated from Nuclear Decay Source G Values	S57
References	S60

S.1 Computational & Quantitative Methods

Microkinetics simulations of autocatalytic formate synthesis were executed using the Kinetiscope simulation environment (<https://hinsberg.net/kinetiscope/>). As a stochastic kinetics simulation engine, Kinetiscope discretizes the problem of microkinetics simulation using the formalism pioneered by Gillespie¹, explicitly tracking of the time evolution of all molecules in a reaction volume using Monte Carlo methods. Simulations were assembled using the single compartment configuration, with chemical schemes as described in S.15-17. All simulations were run on an HP G4 Z4 workstation with 80 gigabytes of RAM and an Intel Xeon Processor.

VUV Irradiance Calculation from 0th-Order Rate Constants; oxalate production rate, r_1 – Linear Approximation
 Reactivity of VUV radiation in CO₂-sparged solutions described by Getoff et al:

- 1 a. $\text{H}_2\text{O} + h\nu \rightarrow \text{H}\cdot + \text{OH}\cdot$
- 1 b. $\text{H}_2\text{O} + h\nu \rightarrow e^{\cdot}_{(\text{aq})} + \text{H}_2\text{O}^+$
- 1 c. $\text{H}\cdot + \text{OH}\cdot \rightarrow \text{H}_2\text{O}$
- 1 d. $\text{H}_2\text{O}^+ + e^{\cdot}_{(\text{aq})} \rightarrow \text{H}_2\text{O}$
- 1 e. $2 \text{H}\cdot \leftrightarrow \text{H}_2$
- 1 d. $2 \text{OH}\cdot \leftrightarrow \text{H}_2\text{O}_2$
- 2 a. $\text{HCO}_2^- + \{\text{H}\cdot, \text{OH}\cdot\} \rightarrow \text{CO}_2^{\cdot-} + \text{H}_2$
- 2 b. $\text{CO}_2 + e^{\cdot}_{(\text{aq})} \rightarrow \text{CO}_2^{\cdot-}$
- 2 c. $2 \text{CO}_2^{\cdot-} \rightarrow \text{C}_2\text{O}_4^{2-}$

The rate of oxalate (oxa) production by reaction 1 is given by:

$$r_1 = \frac{d[\text{oxa}]}{dt} = k_1[\text{CO}_2^-]^2 \quad (\text{a})$$

in the limit of times $\Delta t \ll t_{\text{cycle}}$, we can make the approximation that $d[\text{CO}_2^-]/dt = 0$:

$$\frac{d[\text{CO}_2^-]}{dt} = -k_{2c}[\text{CO}_2^-]^2 + k_{2b}[e^{\cdot}_{(\text{aq})}][\text{CO}_2] + k_{2a}[\text{OH}\cdot + \text{H}\cdot][\text{HCO}_2^-] = 0 \quad (\text{b})$$

$$\frac{d[\text{OH}\cdot]}{dt} = \frac{\phi_{1a}f_{\text{VUV}}}{V} - k_{2a}[\text{OH}\cdot][\text{HCO}_2^-] - k_{1c}[\text{H}\cdot][\text{OH}\cdot] - k_{1d}[\text{OH}\cdot]^2 + k_{1d}'[\text{H}_2\text{O}_2] = 0 \quad (\text{c})$$

$$\frac{d[\text{H}\cdot]}{dt} = \frac{\phi_{1a}f_{\text{VUV}}}{V} - k_{2a}[\text{H}\cdot][\text{HCO}_2^-] - k_{1c}[\text{H}\cdot][\text{OH}\cdot] - k_{1e}[\text{H}\cdot]^2 + k_{1e}'[\text{H}_2] = 0 \quad (\text{d})$$

$$\frac{d[e^{\cdot}_{\text{aq}}]}{dt} = \frac{\phi_{1b}f_{\text{VUV}}}{V} - k_{2b}[e^{\cdot}_{\text{aq}}][\text{CO}_2] = 0 \quad (\text{e}).$$

Using eqs. (c) and (d), we solve for the concentrations of OH \cdot , H \cdot . The resulting quadratic equations give the solutions:

$$[OH\cdot] = \frac{k_{2a}[HCO_2^-] + k_{1c}[H\cdot] \pm \sqrt{(-k_{2a}[HCO_2^-] - k_{1c}[H\cdot])^2 + 4k_{1d}\left(\frac{\phi_{1a}f_{VUV}}{\nu} + k'_{1e}[H_2O_2]\right)}}{-2k_{1d}} \quad (f)$$

$$[H\cdot] = \frac{k_{2a}[HCO_2^-] + k_{1c}[OH\cdot] \pm \sqrt{(-k_{2a}[HCO_2^-] - k_{1c}[OH\cdot])^2 + 4k_{1d}\left(\frac{\phi_{1a}f_{VUV}}{\nu} + k'_{1e}[H_2O_2]\right)}}{-2k_{1d}} \quad (g)$$

Solving for $[OH\cdot]$ and $[H\cdot]$ requires determination of the real roots of equations (f) and (g). General solutions for each are found deductively, by considering that real values for species concentrations must be non-negative. As a result $b^2 - 4ac > b^2$ (as the denominator is negative). So real solutions for $[OH\cdot]$ and $[H\cdot]$ are of the form:

$$\frac{-b - \sqrt{(b^2 - 4ac)}}{2a} \quad (h).$$

Using the roots for $[OH\cdot]$ and $[H\cdot]$ as defined in (h), we then solve for $[CO_2\cdot^-]$ using eq. (b):

$$[CO_2\cdot^-]^2 = \frac{k_{2b}[e_{aq}^-][CO_2] + k_{2a}[HCO_2^-]([OH\cdot] + [H\cdot])}{k_{2c}} \quad (i)$$

it is now seen that substitution of this expression for $[CO_2\cdot^-]^2$ into (a) yields a rate expression where the rate of oxalate production in the forward reaction (2c) has a rate dependence that scales as:

$$\frac{d[oxa]}{dt} = k_1[CO_2\cdot^-]^2 \propto \sqrt{(\phi_{1a}f_{VUV})} \quad (i)$$

This result is consistent with the finding of Getoff and Schenk, where photochemical oxalate production driven by the scheme in 1a – 2c was found to generally show dependencies in agreement with a square root dependence². In addition, solving for the case of $[OH\cdot]$ and $[H\cdot]$ concentrations ~ 0 , the oxalate production rate converges to the following expression:

$$\frac{d[oxa]}{dt} = \frac{k_1\phi_{1b}f_{VUV}[CO_2]}{k_{2c}V} \quad (j)$$

This is consistent with the observation of Getoff that in the particular case of low illumination powers, photochemical oxalate production under VUV illumination shows an approximate linear dependence². Finally, the reasonableness of a steady-state approximation, at least in the limit $t \ll t_{cycles}$, is also considered by inspecting the time-averaged concentration of $CO_2\cdot^-$ in these simulations. Here, $CO_2\cdot^-$ is found to fluctuate about an average value of 5 μM during the course of simulated autocatalysis for the Full System (Figure S1).

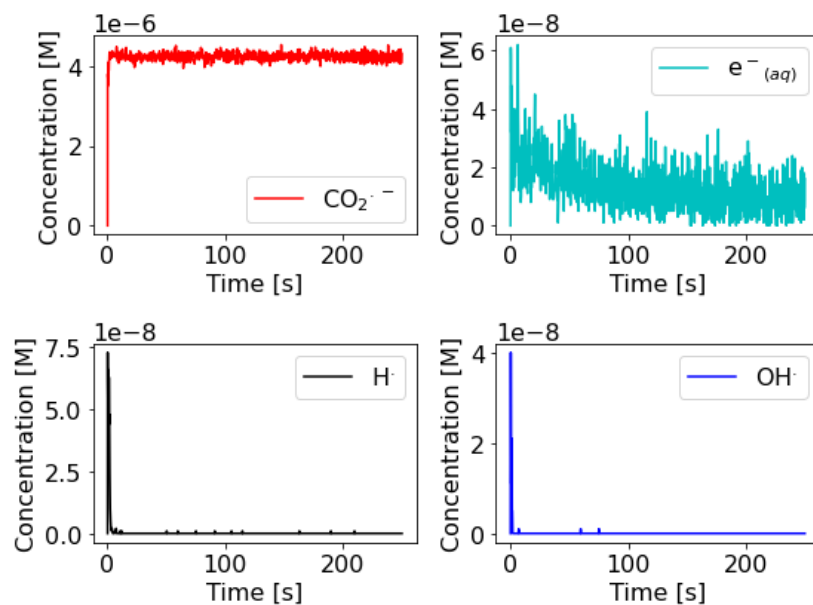


Figure S1

Simulation output of $[\text{CO}_2^{\cdot -}]$, $[e^-_{(aq)}]$, $[\text{H}^{\cdot}]$ and $[\text{OH}^{\cdot}]$ for the fully-described autocatalytic system (Full System), under VUV pumping at steady-state (**top**) and transient (**bottom**) light illumination. $[\text{CO}_2] = 100 \mu\text{M}$, and the reaction is seeded with $100 \mu\text{M}$ formate. Data suggest the reasonableness of a steady-state approximation for these species, at least in the limit of $t \ll t_{\text{cycle}}$. $\text{CO}_2^{\cdot -}$ concentrations average near zero μM during the course of simulation, along with $\text{OH}^{\cdot}/\text{H}^{\cdot}$ Radical species concentrations.

* * *

Below, bounded autocatalysis is calculated according to the canonical replicator model for the case $A + B \rightarrow 2 B$:

$$[B](t) = \frac{[A]_0 + [B]_0}{1 + \frac{[A]_0}{[B]_0} e^{-([A]_0 + [B]_0)kt}} \quad (\text{j})$$

where $k = 0.3$, $[B]_0 = [A]_0 = 100 \mu\text{M}$.

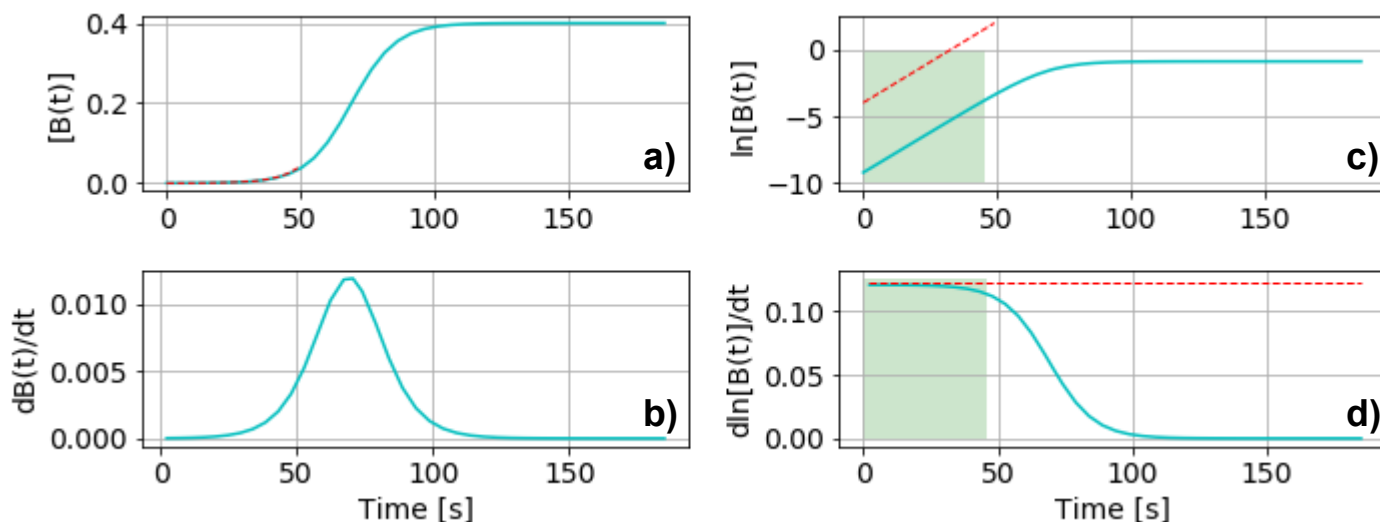


Figure S2

a) An example of bounded (non-ideal) autocatalytic growth over time, for some arbitrary chemical replicator. Here, the convolution of exponential growth kinetics at early times and the onset of growth-limiting processes at intermediate times, make fitting to an exponential growth model difficult, obscuring the values of the growth rate constant (k) and/or replicator selectivity (Ξ). However, **b)** for bounded growth functions, calculation of the 1st derivative of a sigmoid yields a peak, marking times in the growth phase where autocatalysis is now dominated by the growth-limiting processes rather than the kinetics of replicator expansion. This provides a useful guide on the regimes which should be excluded from curve fitting when attempting parameter extraction using an unbounded exponential model. **c)** calculation of $\ln[B(t)]$ should yield regions at early times (green shaded region; the pure exponential growth phases) that yield a straight line (red) with a slope of $k\ln(1+\Xi)$. **d)** Alternatively, calculating $d\ln[B(t)]/dt$ yields a flat line (red) of constant value equaling $k\ln[(1+\Xi)]$ over the same period (green shaded region).

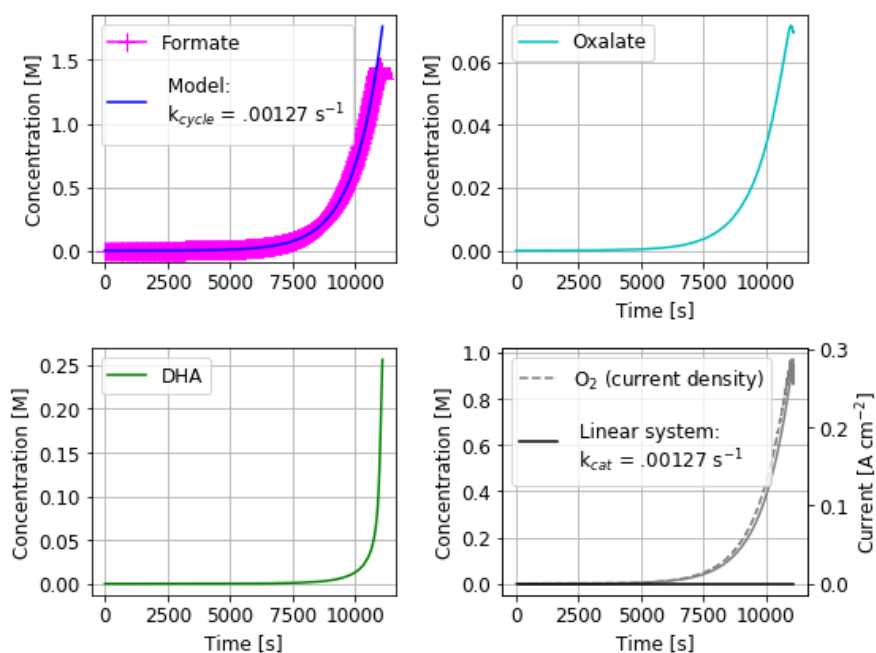


Figure S3

Incorporating the additional details of phosphate and carbonate buffer equilibria into the Basic System simulation are found to produce little change in system response, with the autocatalytic rate constant for formate evolution resulting giving a best fit of $k = 0.00127 \text{ s}^{-1}$. As a result, changes in system response going from the Basic to Partial System simulations can be attributed to the mechanistic details of reaction 2 (electrochemical oxalate reduction) and reaction 3 (DHA hydrolysis).

Table S1

Reaction	Forward	Units	Reverse	Units	Ref
Buffering Equilibria					
Phosphate – Values for $\text{H}_3\text{PO}_4^- (\text{BH}_2) \leftrightarrow \text{H}_2\text{PO}_4^{2-} (\text{BH}) \leftrightarrow \text{HPO}_4^{3-} (\text{B}^-)$ equilibrium ($\text{pK}_{\text{a}1} = 7.20$, $\text{pK}_{\text{a}2} = 12.32$)					
$\text{H}_3\text{O}^+ + \text{B}^- \leftrightarrow \text{BH} + \text{H}_2\text{O}$	1.58e7	$\text{M}^{-1} \text{ s}^{-1}$	1	 s^{-1}	3
$\text{OH}^- + \text{BH} \leftrightarrow \text{B}^- + \text{H}_2\text{O}$	6.34e6	$\text{M}^{-1} \text{ s}^{-1}$	1	 s^{-1}	3
$\text{BH} + \text{H}_3\text{O}^+ \leftrightarrow \text{BH}_2 + \text{H}_2\text{O}$	2.38e12	$\text{M}^{-1} \text{ s}^{-1}$	1	 s^{-1}	3
$\text{OH}^- + \text{BH}_2 \leftrightarrow \text{BH} + \text{H}_2\text{O}$	4.21e1	$\text{M}^{-1} \text{ s}^{-1}$	1	 s^{-1}	3
Carbonate					
$\text{CO}_2 + \text{H}_2\text{O} \leftrightarrow \text{H}_2\text{CO}_3$	0.04	 s^{-1}	12	 s^{-1}	4,5
$\text{CO}_2 + \text{OH}^- \leftrightarrow \text{HCO}_3^-$	1.21e4	$\text{M}^{-1} \text{ s}^{-1}$	4e-4	 s^{-1}	4
$\text{H}_2\text{CO}_3 \leftrightarrow \text{H}^+ + \text{HCO}_3^-$	1e7	 s^{-1}	5e10	$\text{M}^{-1} \text{ s}^{-1}$	6
$\text{HCO}_3^- \leftrightarrow \text{H}^+ + \text{CO}_3^{2-}$	3	 s^{-1}	5e10	$\text{M}^{-1} \text{ s}^{-1}$	6

S.2 Unit Conversions Between Homogeneous and Heterogeneous Concentration

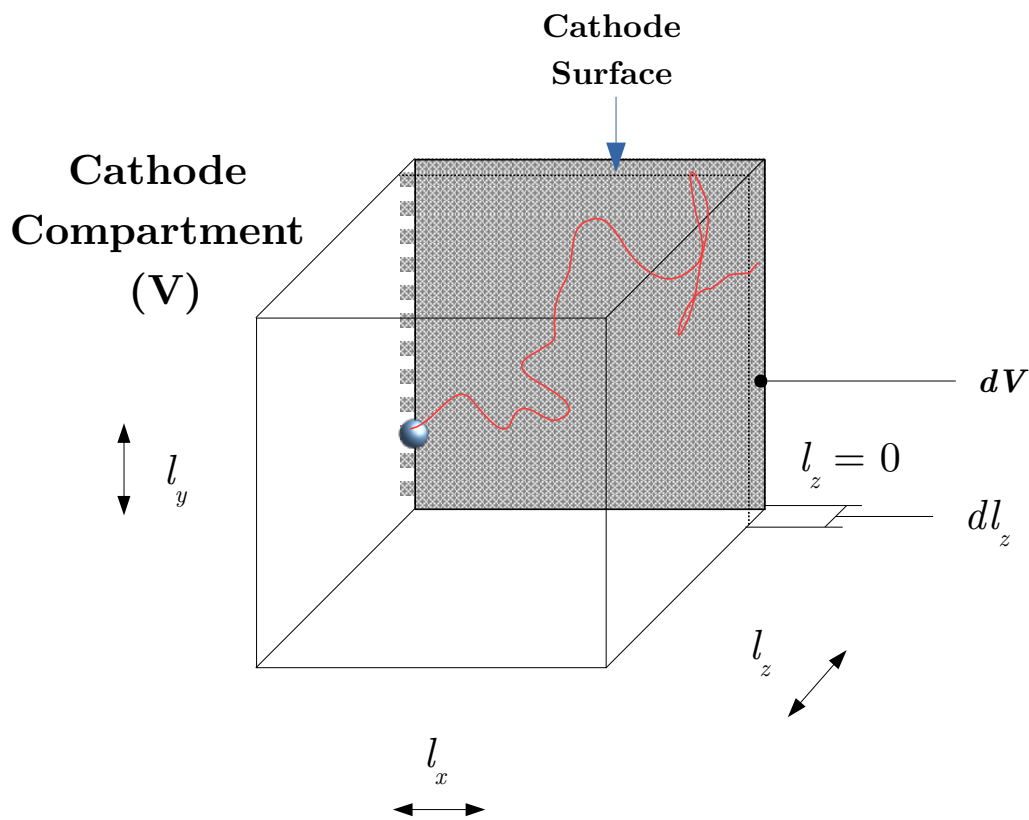


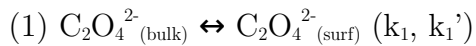
Figure S3

Simulation setup in Kinetiscope. A diffusive (random walk) trajectory for a molecule of oxalate (or glyoxylate) is shown (red line), for random walks between from the compartment bulk into the region defining the electrode surface ($dl = 0.2$ nm). Diffusion of oxalate to the cathode surface was modeled by treating the “surface” region – the region as distances from the surface where oxalate is close enough to the surface as to be considered an adsorbate, taken as $dl = 0.2$ nm. The resulting volume (dV) in which an adsorbate can be found, for a 1 cm^2 electrode bounding one face of a 1 cm^3 volume, is then $2 \times 10^{-8}\text{ cm}^3 = 2 \times 10^{-11}\text{ l}$. Density of active centers are approximated as a metal catalyst (10^{14} cm^{-2}) deposited on a high-aspect ratio ($\sim 1000\times$) substrate for an active site density of 10^{17} cm^{-2} ($1.66 \times 10^{-7}\text{ mol cm}^{-2}$). In the single-compartment simulation in Kinetiscope, this active site density distributed over a differential volume comprising the surface region gives an effective active site concentration $1.66 \times 10^{-7}\text{ mol} / 2 \times 10^{-11}\text{ l} = 8300\text{ M}$.

* * *

Handling Diffusion for Oxalate adsorption/desorption processes:

Step 2 in the proposed sequence of reactions may be decomposed such that oxalate reduction to glyoxylate/dihydroxyacetic acid is governed by an initial step of oxalate diffusion from the bulk region to the surface region, followed by adsorption to a cathodic surface:



A



Species denoted “bulk,” “surf,” and “ads,” respectively refer to states of oxalate that are in bulk solution, the electrode surface boundary region (taken as any distance within ~ 2 angstroms of the electrode surface as described by Figure S3, and oxalate adsorbed and bound to the electrode surface. Note that in this approach, we treat the binding of oxalate to an electrode active site (A) as pseudo-first order, as in the surface region, the effective active site concentration is very high (8300 M effective concentration). Oxalate diffusion from the bulk to surface region is handled by considering the following rate equations:

$$\frac{d[\text{C}_2\text{O}_4^{2-}(\text{surf})]}{dt} = k_1[\text{C}_2\text{O}_4^{2-}(\text{bulk})] + k_2'[\text{A-C}_2\text{O}_4^{2-}(\text{ads})] - k_2[\text{C}_2\text{O}_4^{2-}(\text{surf})] - k_1'[\text{C}_2\text{O}_4^{2-}(\text{surf})]$$

$$\frac{d[\text{C}_2\text{O}_4^{2-}(\text{ads})]}{dt} = k_2[\text{C}_2\text{O}_4^{2-}(\text{surf})] + k_1'[\text{A-C}_2\text{O}_4^{2-}(\text{ads})]$$

It is difficult to provide meaningful rate constants for oxalate adsorption/desorption. However, interconversion between oxalate in the surface region and oxalate adsorbate is assumed to be rapid relative to oxalate diffusion from the bulk into the surface region. As a result, this gives a rate expression controlled by the first step:

$$r = k_1[\text{C}_2\text{O}_4^{2-}(\text{bulk})] - k_1'[\text{C}_2\text{O}_4^{2-}(\text{surf})]$$

Over timescales much shorter than the replication cycle time, we approximate these processes as steady-state. Solving for $\text{C}_2\text{O}_4^{2-}(\text{surf})$ in terms of $\text{C}_2\text{O}_4^{2-}(\text{ads})$, the following rate description for oxalate conversion to an adsorbate results:

$$r = k_1[\text{C}_2\text{O}_4^{2-}(\text{bulk})] - \frac{k_1'k_2'}{k_2}[\text{C}_2\text{O}_4^{2-}(\text{ads})] = k_1[\text{C}_2\text{O}_4^{2-}(\text{bulk})] - \frac{k_1'}{K_2}[\text{C}_2\text{O}_4^{2-}(\text{ads})]$$

a unimolecular rate constant for glyoxylate diffusion between the bulk and surface region is calculated using the oxalate diffusion coefficient, $D_{\text{oxa}} = 1.03 \times 10^{-5} \text{ cm}^2 \text{ s}^{-1}$, as discussed in the manuscript⁷. The ratio $k_2/k_2' = K_2$, the equilibrium constant for oxalate adsorption/desorption within the electrode surface region. With oxalate adsorption/desorption equilibria unclear, we take the value of these fast processes to be similar, such that $K_2 \sim 1$. To check against this assumption, we perform a sensitivity analysis for this system for $K_2 = 1 \times 10^{-3}$, 1, and 1000. (Partial System response shown). As seen in Figure S4, values of K_2 spanning even six orders of magnitude do not appreciably change the formate doubling time, suggestive that the overriding assumption that oxalate adsorption/desorption rates do not significantly influence process kinetics.

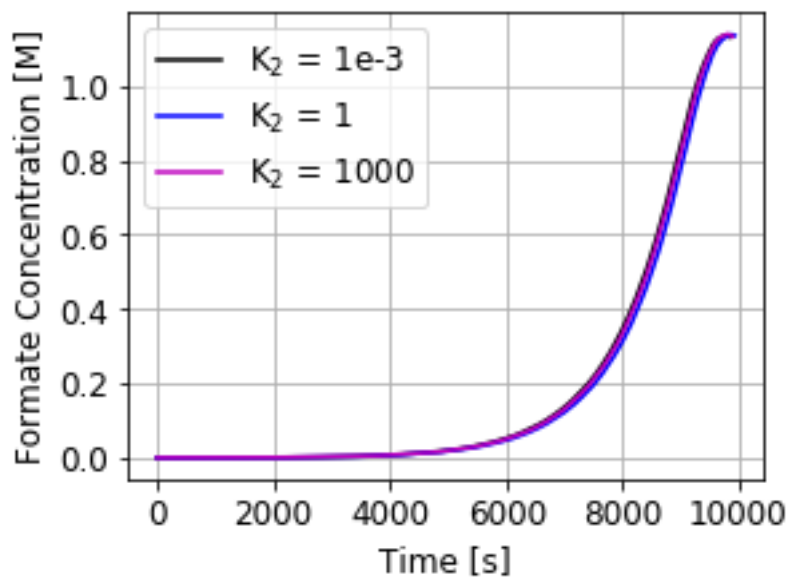


Figure S4

Partial System formate replication as a function of changing oxalate adsorption/desorption equilibrium constants. Changing values of K_2 over six orders of magnitude ($K_2 = 1 \times 10^{-3}$, 1, and 1000) reveals that formate replication displays very low sensitivity to the value of this equilibrium constant.

S.3 Model Parameterization – Determination of Rate Constants

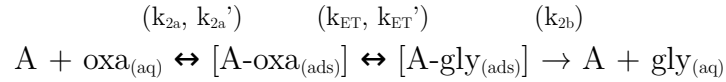
Step 1 rate constants

Rate constants used for simulation of radical reactions constituting step 1 were taken from Pastina et al⁸., Severin et al⁹., and Getoff et al^{2,10}. These values are detailed in section S.17.

* * *

Step 2 rate constants

Reaction 2 is decomposed according to the following mechanism:



In this mechanism, A_T is the total active site density, oxa is the concentration of the cathode substrate, oxalate, $\text{A-oxa}_{(\text{ads})}$ is the density of active sites with adsorbed substrate (oxalate), $\text{A-gly}_{(\text{ads})}$ is the density of active sites with adsorbed product (glyoxylate). Gly gives the concentration of free glyoxylate.

For oxalate reduction, take electrochemical reduction of the adsorbed product species to be the rate-determining process in the conversion to glyoxylate. This is consistent with reports that oxalate reduction over graphite and mercury cathodes¹¹ is rate-controlled by ET to oxalate adsorbates, and assumes that substrate interconversion between substrate-free and electrode-adsorbed states are characterized by rapid equilibria. With ET to the substrate as our rate-determining step, we start from the rate law:

$$r_2(t, V) = k_{\text{ET}}[\text{A-oxa}_{(\text{ads})}] - k'_{\text{ET}}[\text{A-gly}_{(\text{ads})}] \quad .$$

Here, rate constants k_{ET} and k'_{ET} are the interfacial electron transfer rate constants governing the respective, electrode-mediated reduction (k_{ET}) and oxidation (k'_{ET}) of the oxalate/glyoxylate adsorbates:

$$k_{\text{ET}}(\eta) = k_0 \left[\exp\left(\frac{nF\alpha\eta}{RT}\right) \right] \quad ; \quad k'_{\text{ET}}(\eta) = k_0 \left[\exp\left(-\frac{nF\eta(1-\alpha)}{RT}\right) \right] \quad .$$

Using values of $n = 0.3$ V, $\alpha = 0.5$ and $T = 298$ k, for a prototypical exchange current density of 10^{-5} A cm^{-2} , multiplied by a 1000x aspect ratio (total surface coverage = 10^{17} cm^{-2}), yields rate constants of $k_0 = 0.624$ s^{-1} , $k_{\text{ET}} = 215$ s^{-1} , $k'_{\text{ET}} = 0.002$ s^{-1} .

* * *

Step 3 rate constants

A usable expression for the catalyst-DHA* complex is determined according to Mechanism A:



Here, Cat is a homogeneous catalyst, Cat-DHA denotes a transient catalyst-dihydroxyacetate complex, and Cat-DHA* is the transient catalyst-pre-fission Intermediate (DHA*) complex, which decays to two formate molecules

while regenerating the catalyst. Because there is no available data on the kinetics of this reaction, rate constants were chosen to be conservative, with low values being used to parameterize DHA-catalyst binding equilibria, DHA conversion to form the DHA*, along with assumptions of slow decay of the DHA* into two formate equivalents. In addition, sensitivity analyses were conducted for this reaction, to show the impact of a range of rate constants on overall cycle behavior (S.7).

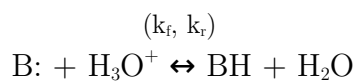
* * *

Buffering Equilibria

Rate constants for buffering equilibria were calculated according to the general expression

$$K_a = k_f/k_r,$$

for a process



where K_a is the acid-base equilibrium constant for a buffer of some specified $\text{p}K_a$, k_f is the forward rate constant for protonation and k_r represents the reverse rate constant for deprotonation. K_b values were calculated according to the relation

$$K_b = 1 \times 10^{14} / K_a.$$

S.3 Model Parameterization – Thermochemical Data

Values for the free energies of combustion for all species in Table S1 were found by applying Hess' Law to combustion reactions for formic acid, oxalic acid, and dihydroxyacetic acid and their conjugate bases. The free energies of formation for all components of each combustion reaction were then used to determine the overall free energy change for combustion. Values for hydrogen were determined from the relation:

$$\Delta G^0 = -nF\Delta E^0.$$

Table S1

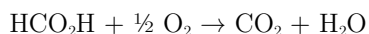
ΔG_c^0 values in bold (conjugate base forms) were used in the calculation of replication energy efficiencies in S9.

Compound	$\Delta_f G^0$ [kJ mol ⁻¹]	ΔH_c^0 [kJ mol ⁻¹] (acid)	ΔE^0 [V]	ΔG_c^0 [kJ mol ⁻¹]	Reference
H ₂ O	-237.19	-	-	-	12
OH ⁻	-157.27	-	-	-	12
O ₂	0	-	-	-	12
CO ₂	-394.37	-	-	-	12
Formate/ Formic Acid	-351.00/-371.79	-254.3	-	-200.27 /-259.77	12-14
Oxalate/ Oxalic Acid	-673.00	-242.9	-	-273.63 /-352.93	13
Dihydroxyacetate/ Dihydroxyacetic acid	-478.85 ^a	-524.8	-	-624.43 /-784.27	12,15
Glyoxylate/Glyoxylic Acid	-468.60	-523.00	-	-477.41 /-557.33	12
Hydrogen	-	-	1.2	-237.3	16

a. Value is calculated starting from the literature value for the free energy of formation of glyoxylate ($\Delta G_c = -468.60$ kJ/mol) and adjusting using the glyoxylate/dihydroxyacetate equilibrium constant, $K = 0.016^{15}$ from Eggins and McMullan.

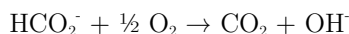
Calculations of ΔG_c^0 for various replication fuel products. Terms in red denote free energies of formation for conjugate bases being used in the calculation of acid form products. As a result, the resulting ΔG_c^0 s for the acid form products are only estimates within 10-20 kJ/mol of their real values.

Formic Acid:



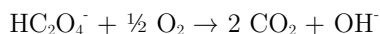
$$\Delta G_c^0 = [(1)(-394.37) + (1)(-237.19)] - [(1)(-371.79) + (0.5)(0)] = -259.77 \text{ kJ/mol}$$

Formate:



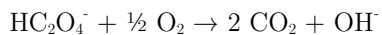
$$\Delta G_c^0 = [(1)(-394.37) + (1)(-157.27)] - [(1)(-351.00) + (0.5)(0)] = -200.27 \text{ kJ/mol}$$

Oxalic Acid:



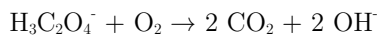
$$\Delta G_c^0 = [(2)(-394.37) + (1)(-237.19)] - [(1)(-673.00) + (0.5)(0)] = -352.93 \text{ kJ/mol}$$

Oxalate:



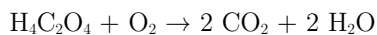
$$\Delta G_c^0 = [(2)(-394.37) + (1)(-157.27)] - [(1)(-673.00) + (0.5)(0)] = -273.63 \text{ kJ/mol}$$

Dihydroxyacetate:



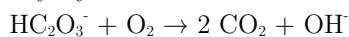
$$\Delta G_c^0 = [(2)(-394.37) + (2)(-157.27)] - [(1)(-478.85) + (1)(0)] = -624.43 \text{ kJ/mol}$$

Dihydroxyacetic Acid:



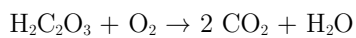
$$\Delta G_c^0 = [(2)(-394.37) + (2)(-237.19)] - [(1)(-478.85) + (1)(0)] = -784.27 \text{ kJ/mol}$$

Glyoxylate:



$$\Delta G_c^0 = [(2)(-394.37) + (1)(-157.27)] - [(1)(-468.60) + (1)(0)] = -477.41 \text{ kJ/mol}$$

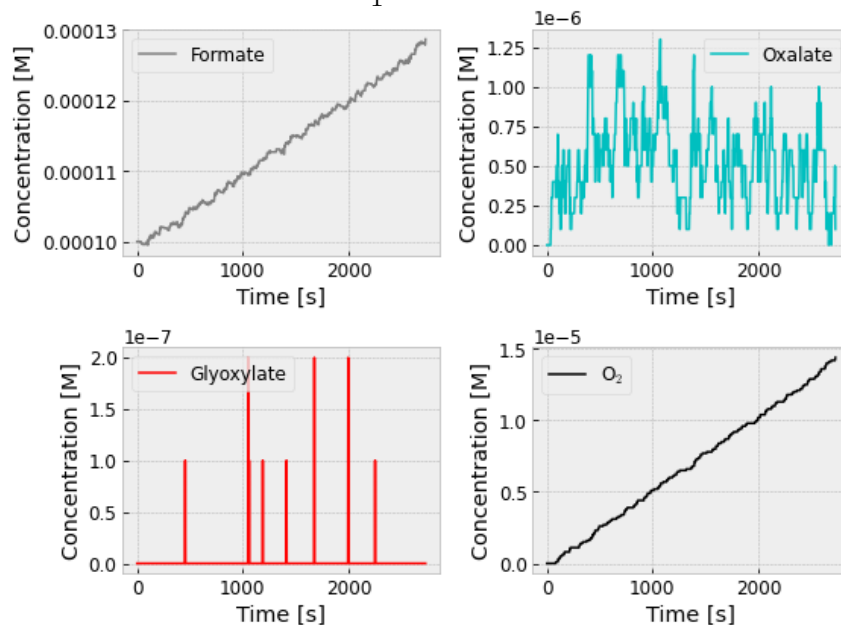
Glyoxylic Acid:



$$\Delta G_c^0 = [(2)(-394.37) + (1)(-237.19)] - [(1)(-468.60) + (1)(0)] = -557.33 \text{ kJ/mol}$$

S.4 Product Selection as a Function of Rate Constants – Reaction 1 Sensitivity

$$k_1 = 1 \text{ M}^{-1} \text{ s}^{-1}$$



$$k_1 = 100 \text{ M}^{-1} \text{ s}^{-1}$$

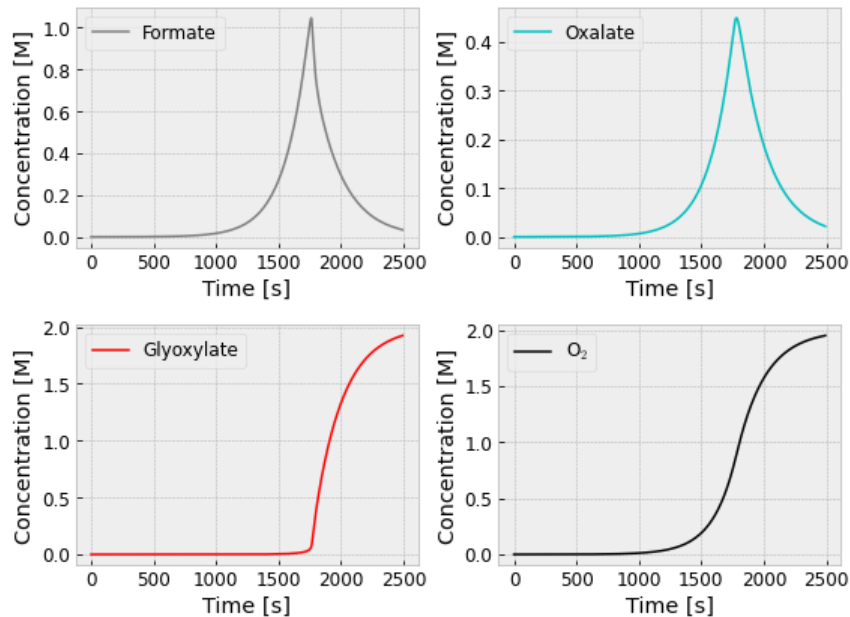
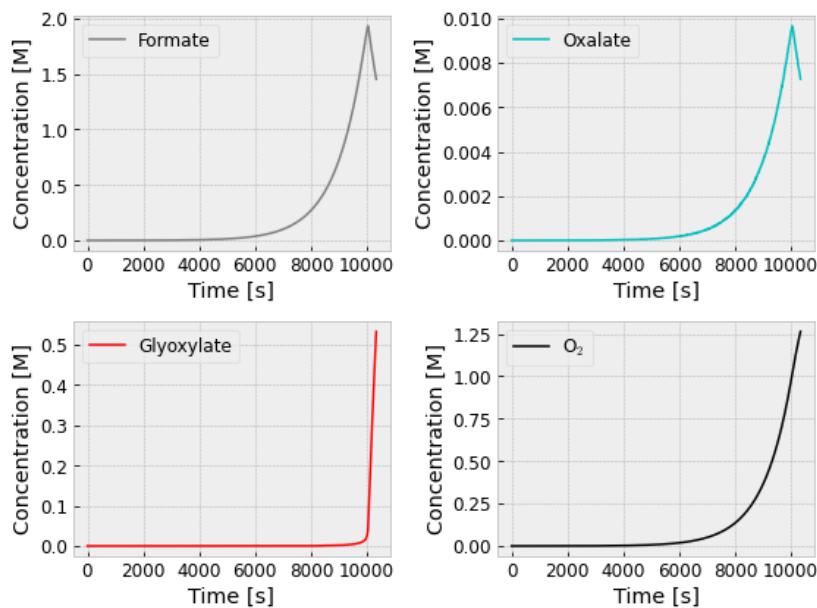


Figure S5 – Basic System

Influence of rate constant k_1 on the evolution of autocatalytic intermediates formate, oxalate and glyoxylate, along with O₂ evolution. $k_2 = 0.01 \text{ s}^{-1}$, $k_3 = 1000 \text{ M}^{-1} \text{ s}^{-1}$. Spikes and hard transitions observed in these reactions occur from the total consumption of water (simulated as a batch species) during the simulation time.

S.4 Product Selection as a Function of Rate Constants – Reaction 2 Sensitivity

$$k_2 = 0.1 \text{ s}^{-1}$$



$$k_2 = 1 \text{ s}^{-1}$$

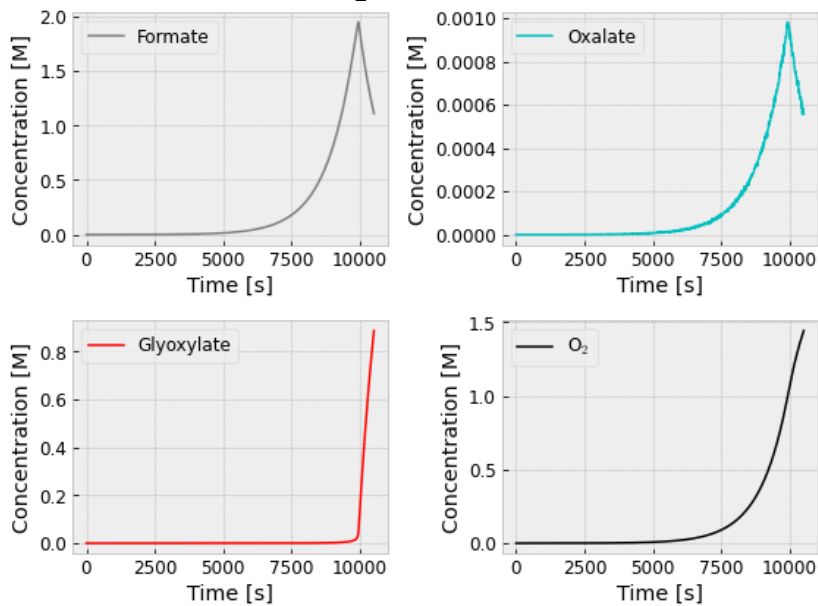


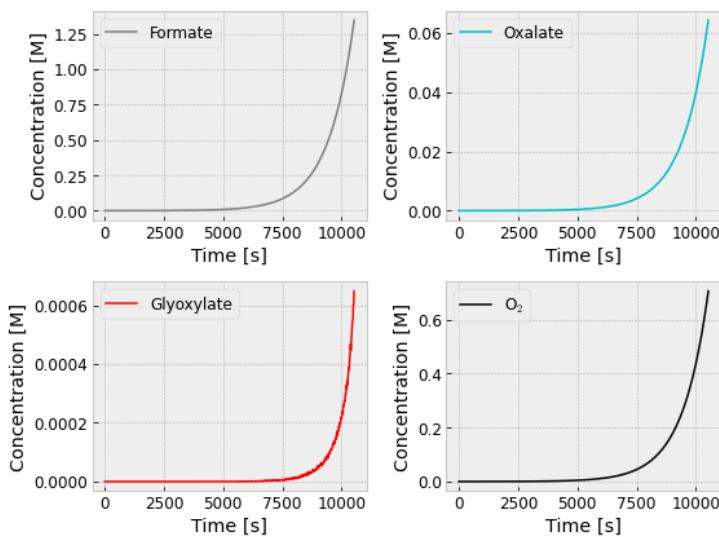
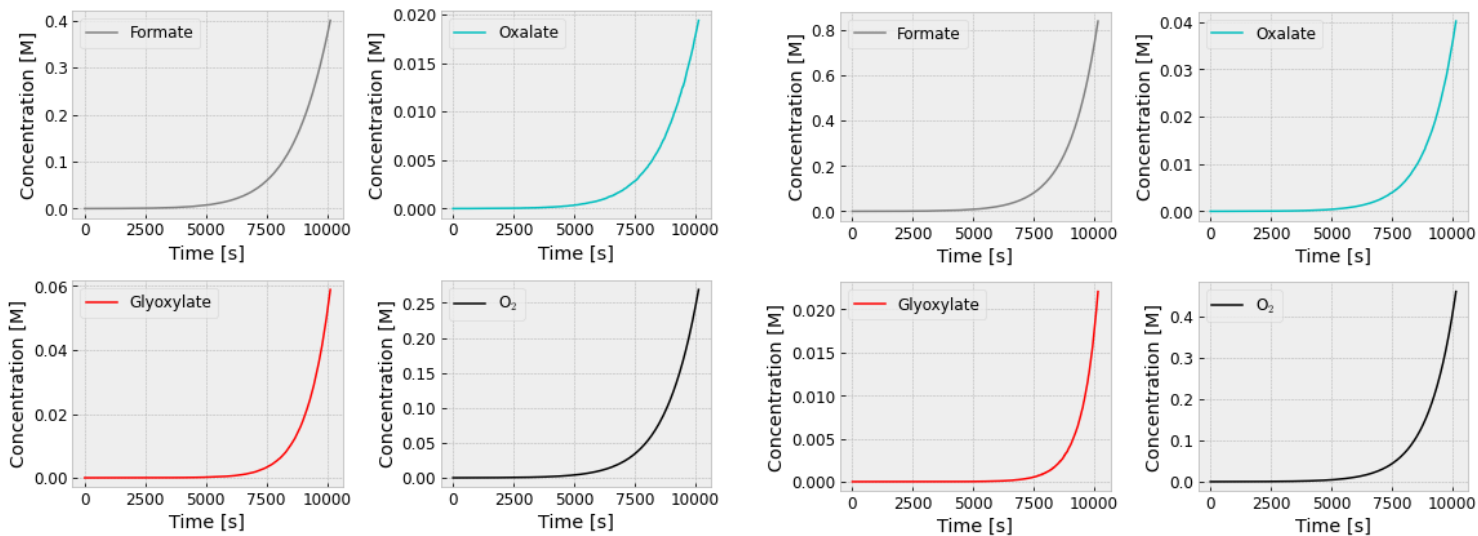
Figure S6 – Basic System

Influence of rate constant k_2 on the evolution of autocatalytic intermediates formate, oxalate and glyoxylate, along with O₂ evolution. $k_1 = 10 \text{ M}^{-1} \text{ s}^{-1}$, $k_3 = 1000 \text{ M}^{-1} \text{ s}^{-1}$. Spikes and hard transitions observed in these reactions occur from the total consumption of water (simulated as a batch species) during the simulation time.

S.4 Product Selection as a Function of Rate Constants – Reaction 3 Sensitivity

$$k_3 = 10 \text{ M}^{-1} \text{ s}^{-1}$$

$$k_3 = 1000 \text{ M}^{-1} \text{ s}^{-1}$$



$$k_3 = 10000 \text{ M}^{-1} \text{ s}^{-1}$$

Figure S7 – Basic System

Influence of rate constant k_3 on the evolution of autocatalytic intermediates formate, oxalate and glyoxylate, along with O_2 evolution. $k_1 = 10 \text{ M}^{-1} \text{ s}^{-1}$, $k_2 = 0.1 \text{ s}^{-1}$.

S.5 Effects of Side Reactions – Selectivity of Reaction 1

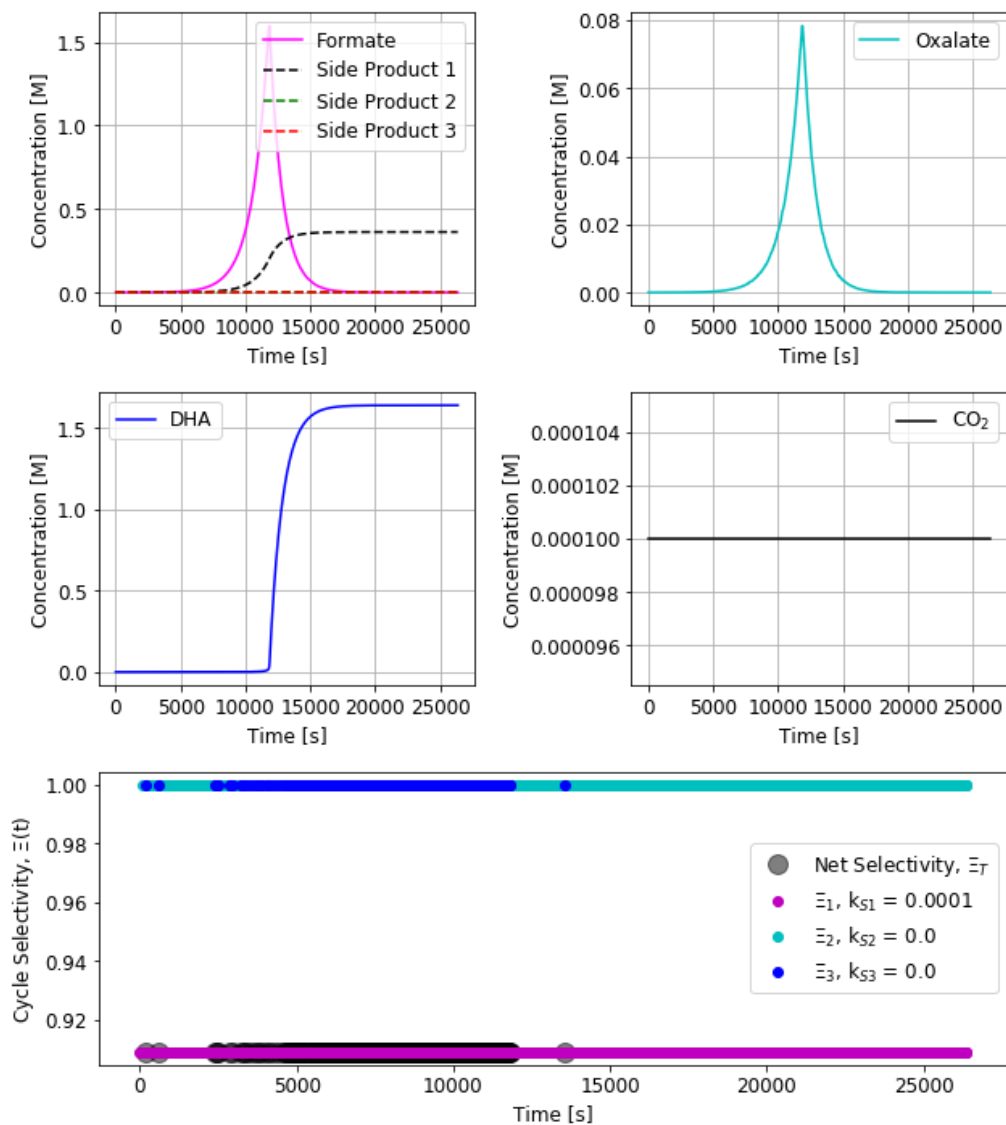


Figure S8 – Basic System

$$k_{s1} = 0.0001 \text{ s}^{-1}, k_{s2} = 0.0 \text{ s}^{-1}, k_{s3} = 0.0 \text{ s}^{-1}$$

Influence of side reactions in step 1 (formate carboxylation). Side reactions are generalized as unimolecular decays following the rate law $r_{s1} = k_{s1}[\text{formate}]$. Spikes and hard transitions observed in these reactions occur from the total consumption of water (simulated as a batch species) during the simulation time. Net selectivity is undefined for times where replication has been arrested, and subsequent reactions only result in the consumption of formate.

S.5 Effects of Side Reactions – Selectivity of Reaction 1

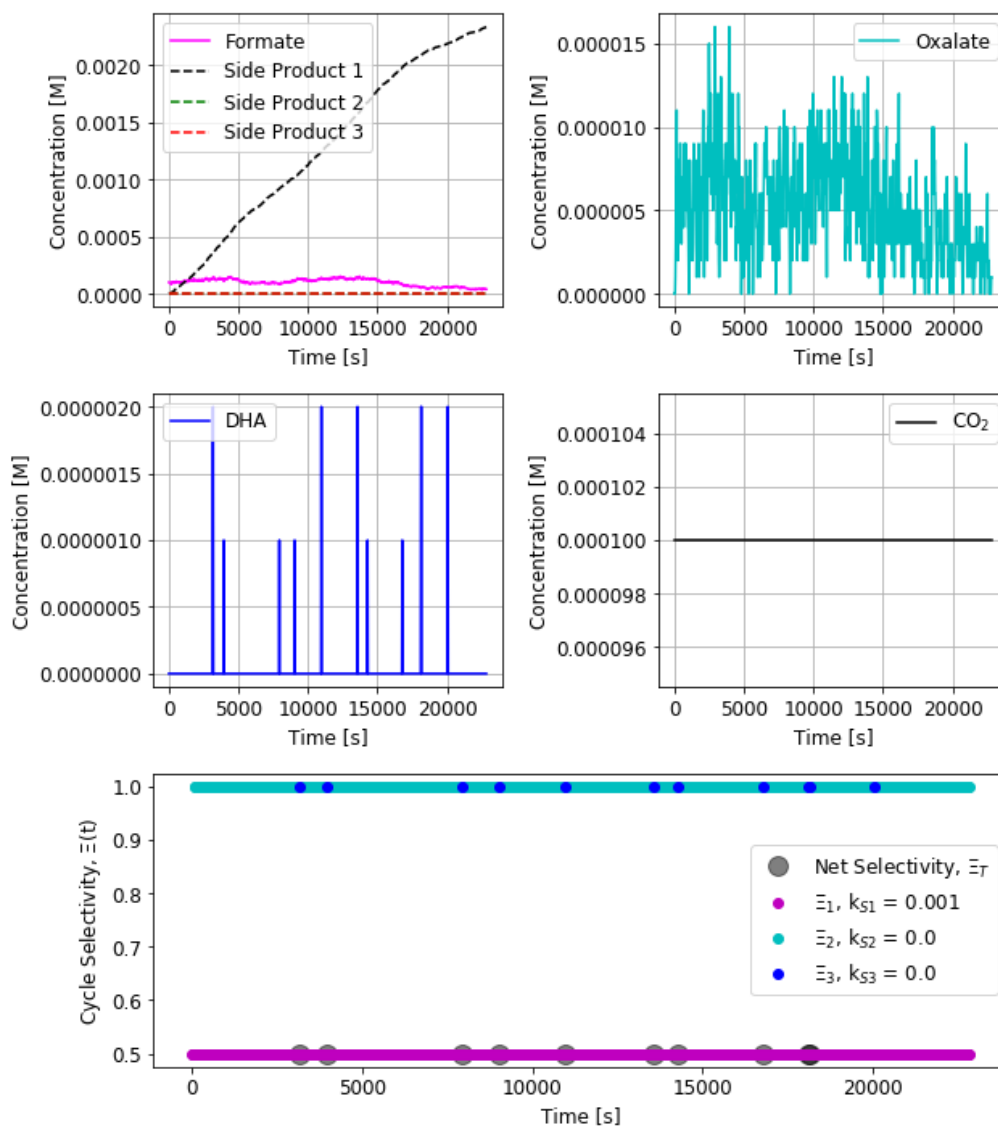


Figure S9 – Basic System

$$k_{s1} = 0.001 \text{ s}^{-1}, k_{s2} = 0.0 \text{ s}^{-1}, k_{s3} = 0.0 \text{ s}^{-1}$$

Influence of side reactions in step 1 (formate carboxylation). Side reactions are generalized as unimolecular decays following the rate law $r_{s1} = k_{s1}[\text{formate}]$. Net selectivity is undefined for times where replication has been arrested, and subsequent reactions only result in the consumption of formate.

S.5 Effects of Side Reactions – Selectivity of Reaction 1

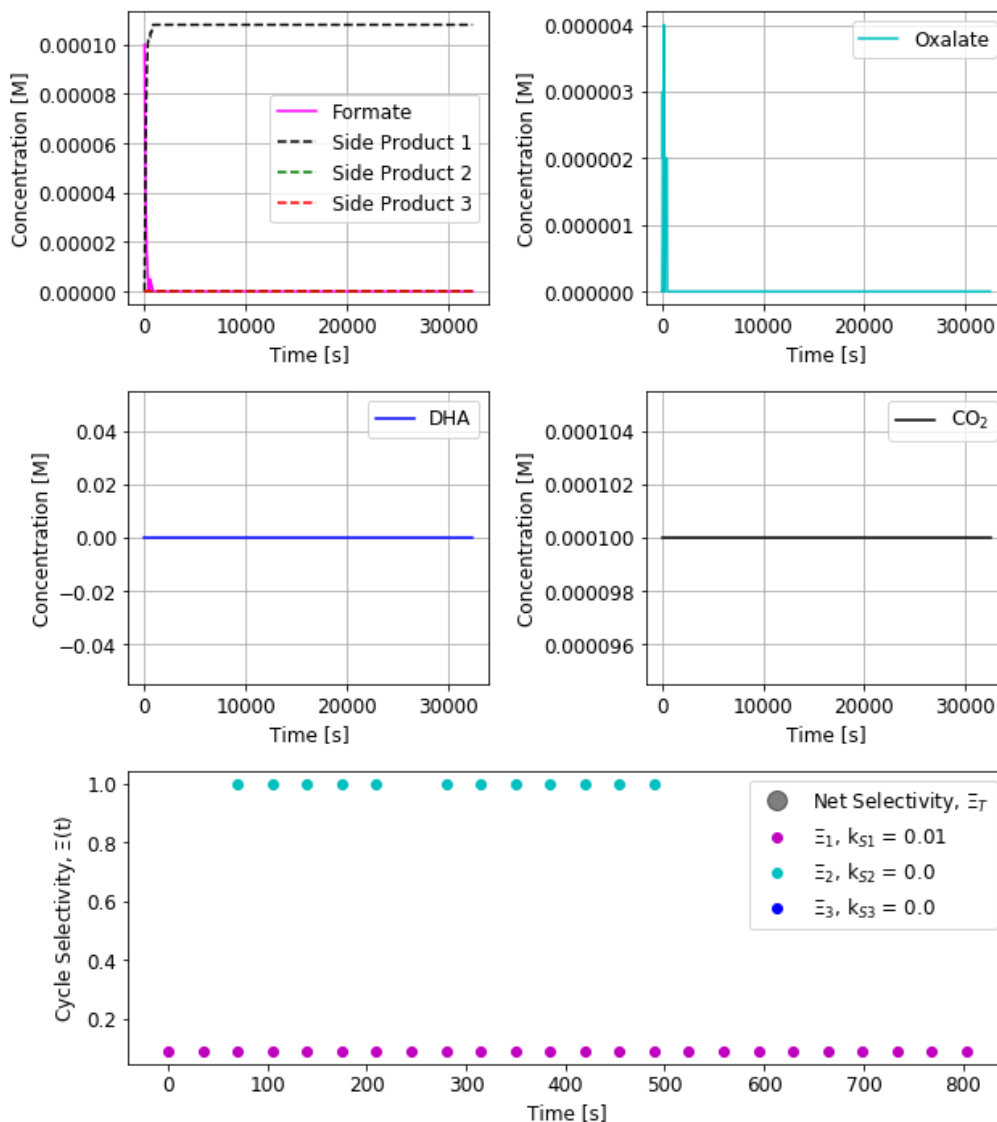


Figure S10 – Basic System

$$k_{s1} = 0.01 \text{ s}^{-1}, k_{s2} = 0.0 \text{ s}^{-1}, k_{s3} = 0.0 \text{ s}^{-1}$$

Influence of side reactions in step 1 (formate carboxylation). Side reactions are generalized as unimolecular decays following the rate law $r_{s1} = k_{s1}[\text{formate}]$. At this value of k_{s1} , the rate of side product formation completely arrests formate turnover into oxalate at early times in the reaction, halting formate growth. This results in an undefined net reaction selectivity for the overall cycle. Net selectivity is undefined for times where replication has been arrested, and subsequent reactions only result in the consumption of formate.

S.5 Effects of Side Reactions – Selectivity of Reaction 1

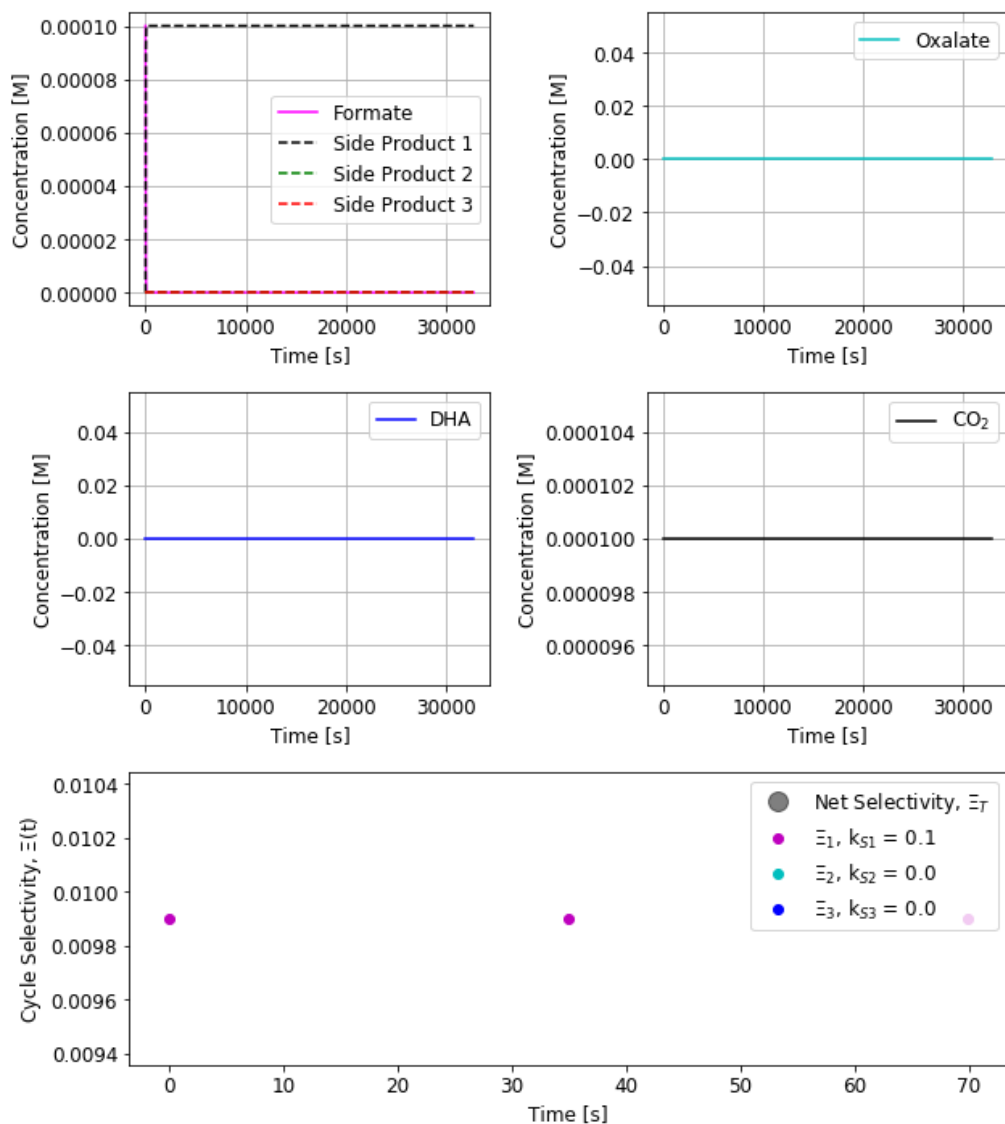


Figure S11 – Basic System

$$k_{s1} = 0.1 \text{ s}^{-1}, k_{s2} = 0.0 \text{ s}^{-1}, k_{s3} = 0.0 \text{ s}^{-1}$$

Influence of side reactions in step 1 (formate carboxylation). Side reactions are generalized as unimolecular decays following the rate law $r_{s1} = k_{s1}[\text{formate}]$. At this value of k_{s1} , the rate of side product formation completely arrests autocatalysis, resulting in an undefined net reaction selectivity.

S.5 Effects of Side Reactions – Selectivity of Reaction 2

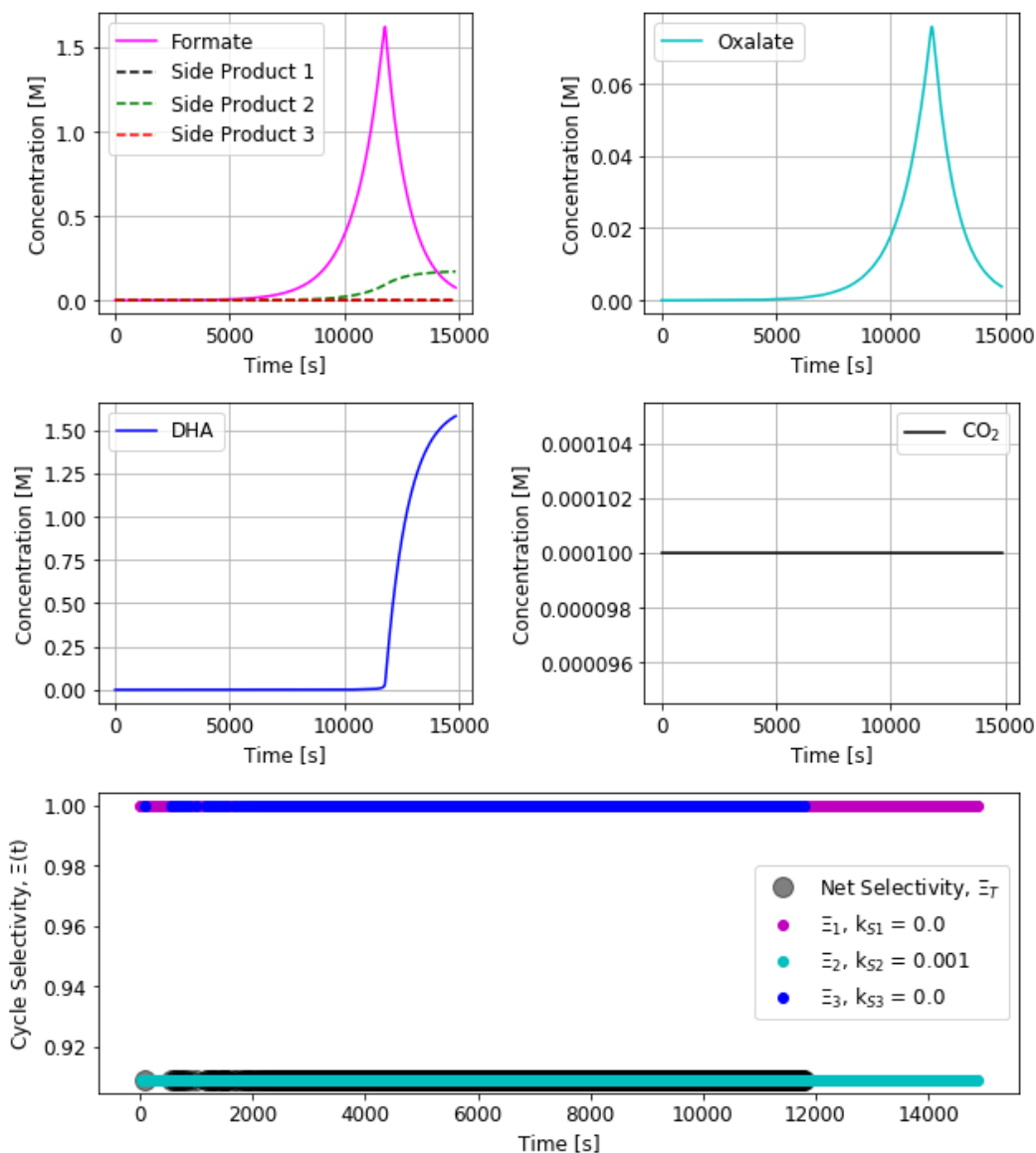


Figure S12 – Basic System

$$k_{s1} = 0.0 \text{ s}^{-1}, k_{s2} = 0.001 \text{ s}^{-1}, k_{s3} = 0.0 \text{ s}^{-1}$$

Influence of side reactions in step 2 (oxalate reduction). Side reactions are generalized as unimolecular decays following the rate law $r_{s2} = k_{s2}[\text{oxalate}]$. Spikes and hard transitions observed in these reactions occur from the total consumption of water (simulated as a batch species) during the simulation time. Net selectivity is undefined for times where replication has been arrested, and subsequent reactions only result in the consumption of formate.

S.5 Effects of Side Reactions – Selectivity of Reaction 2

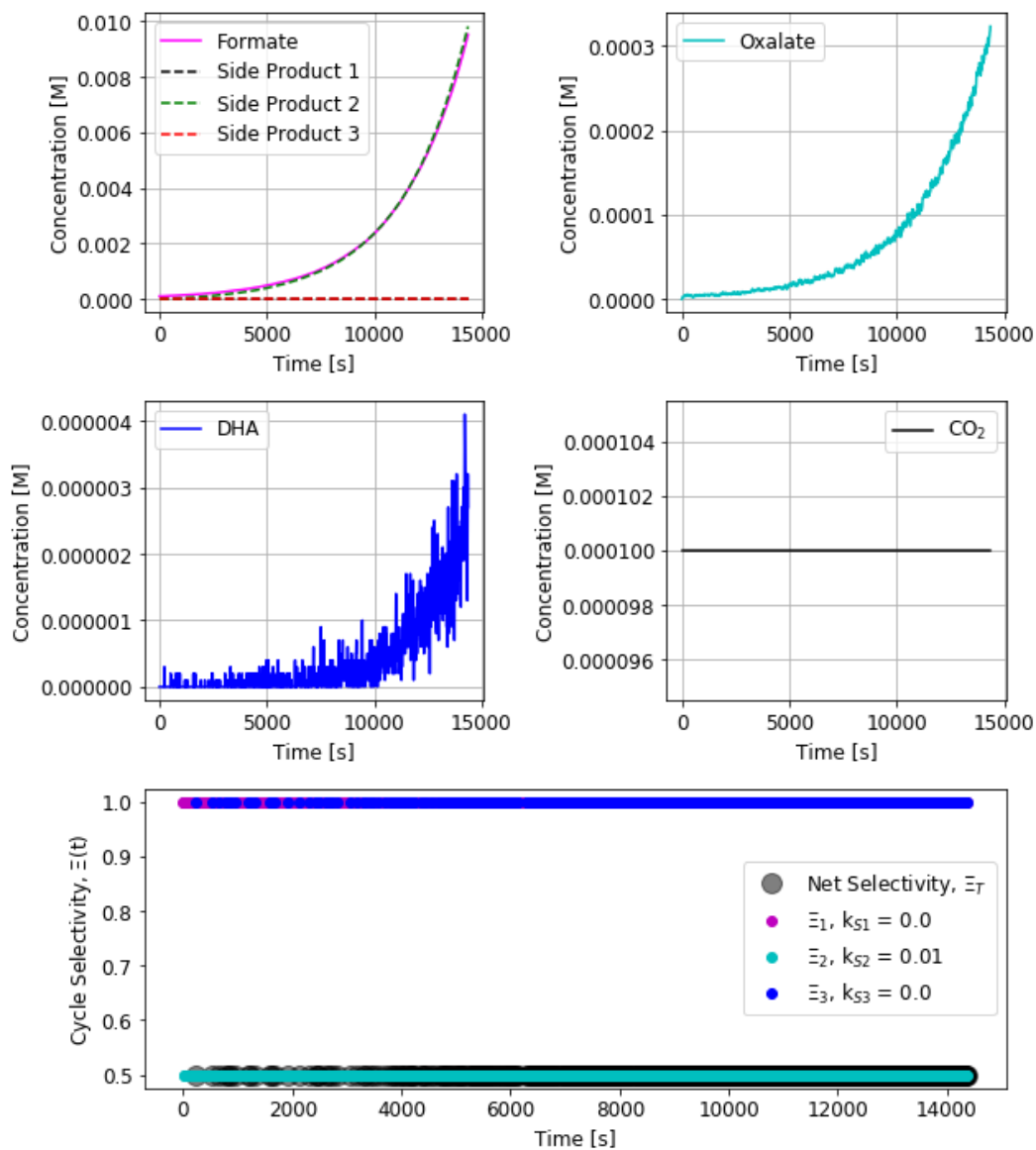


Figure S13 – Basic System

$$k_{s1} = 0.0 \text{ s}^{-1}, k_{s2} = 0.01 \text{ s}^{-1}, k_{s3} = 0.0 \text{ s}^{-1}$$

Influence of side reactions in step 2 (oxalate reduction). Side reactions are treated as a generic reaction following the rate law $r_{s2} = k_{s2}[\text{oxalate}]$.

S.5 Effects of Side Reactions – Selectivity of Reaction 3

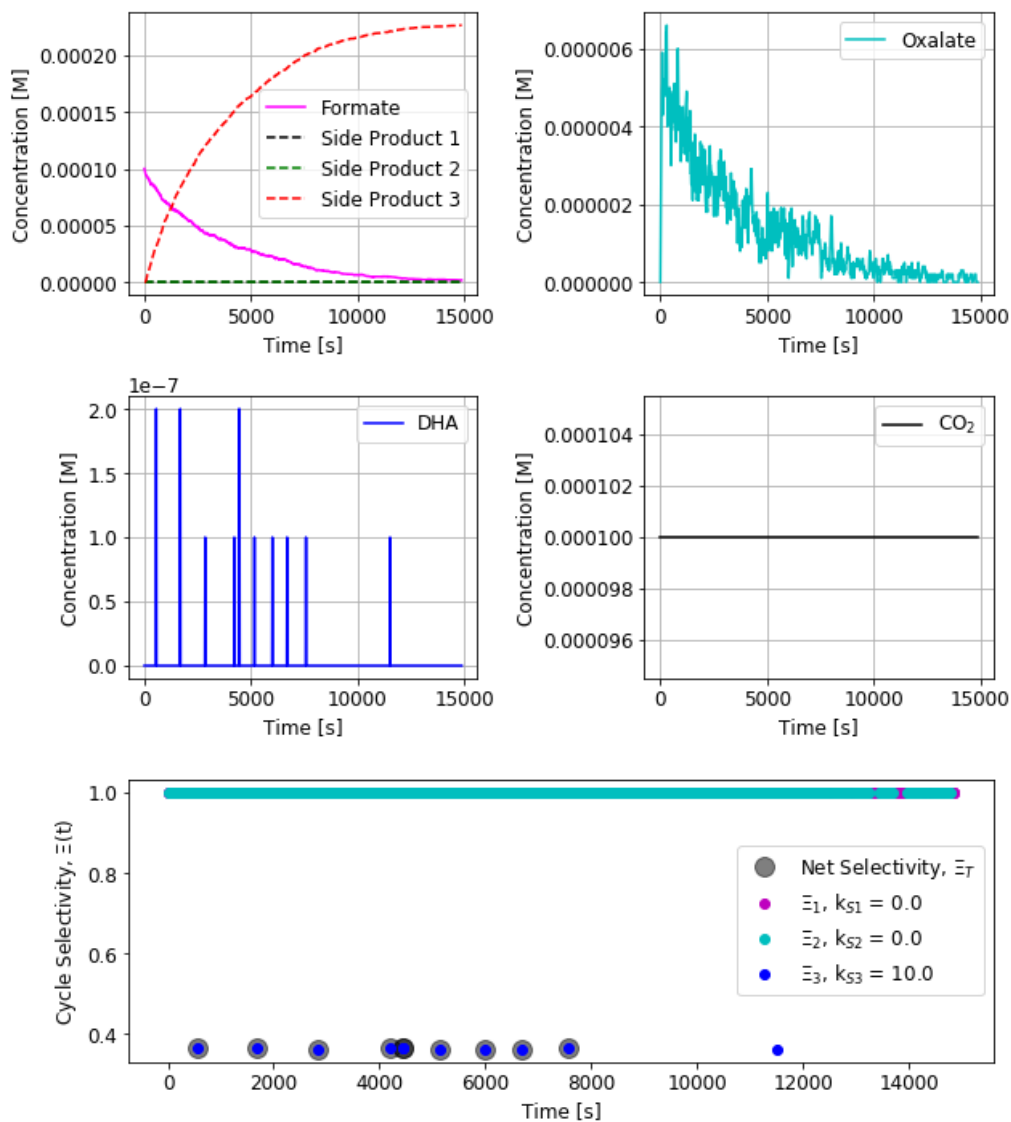


Figure S14 – Basic System

$$k_{s1} = 0.0 \text{ s}^{-1}, k_{s2} = 0.0 \text{ s}^{-1}, k_{s3} = 10.0 \text{ s}^{-1}$$

Influence of side reactions in step 3 (formate carboxylation). Side reactions are treated as a generic reaction following the rate law $r_{s3} = k_{s3}[\text{DHA}]$. Net selectivity is undefined for times where replication has been arrested, and subsequent reactions only result in the consumption of formate.

S.5 Effects of Side Reactions – Selectivity of Reaction 3

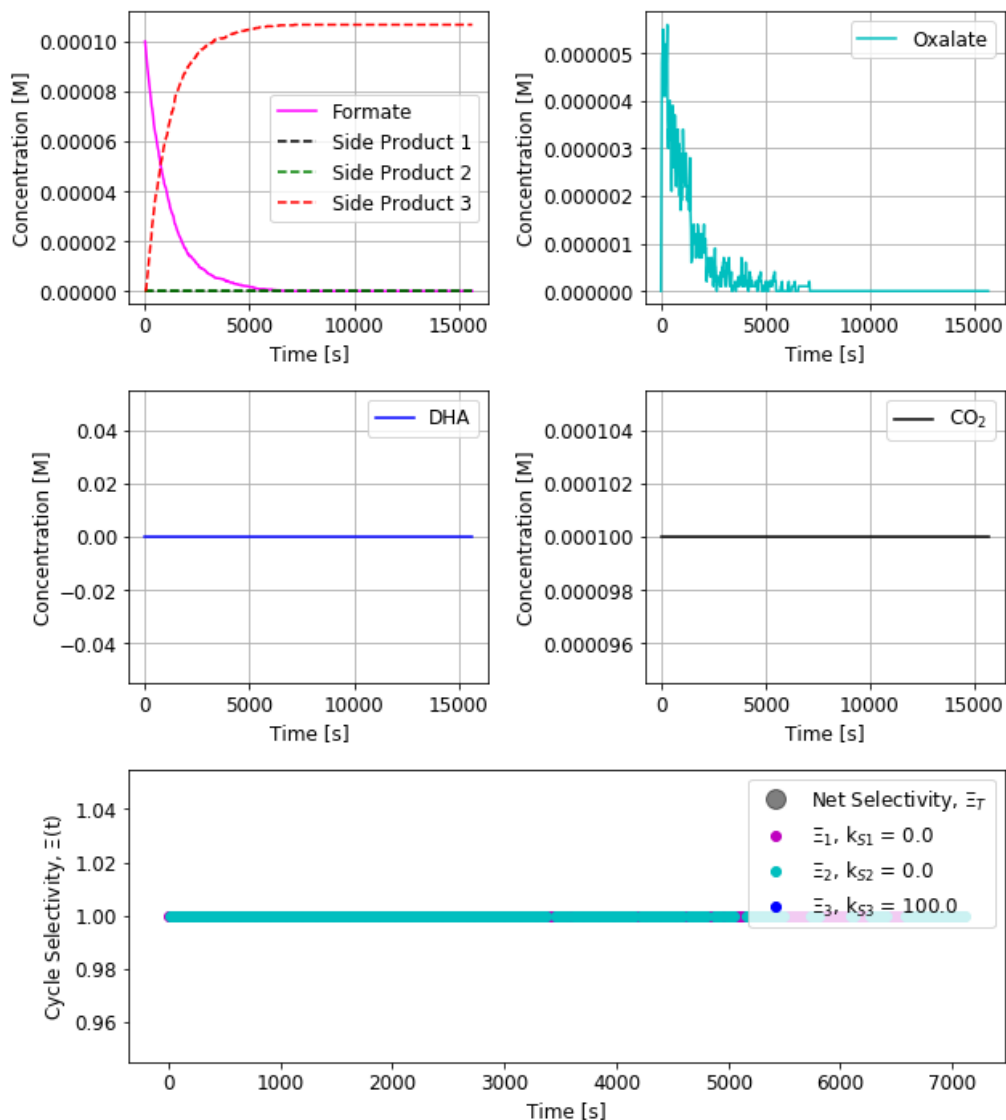


Figure S15 – Basic System

$$k_{s1} = 0.0 \text{ s}^{-1}, k_{s2} = 0.0 \text{ s}^{-1}, k_{s3} = 100.0 \text{ s}^{-1}$$

Influence of side reactions in step 3 (formate carboxylation). Side reactions are treated as a generic reaction following the rate law $r_{s3} = k_{s3}[\text{DHA}]$. Net selectivity is undefined for times where replication has been arrested, and subsequent reactions only result in the consumption of formate.

S.5 Effects of Side Reactions – Selectivity of Reaction 3

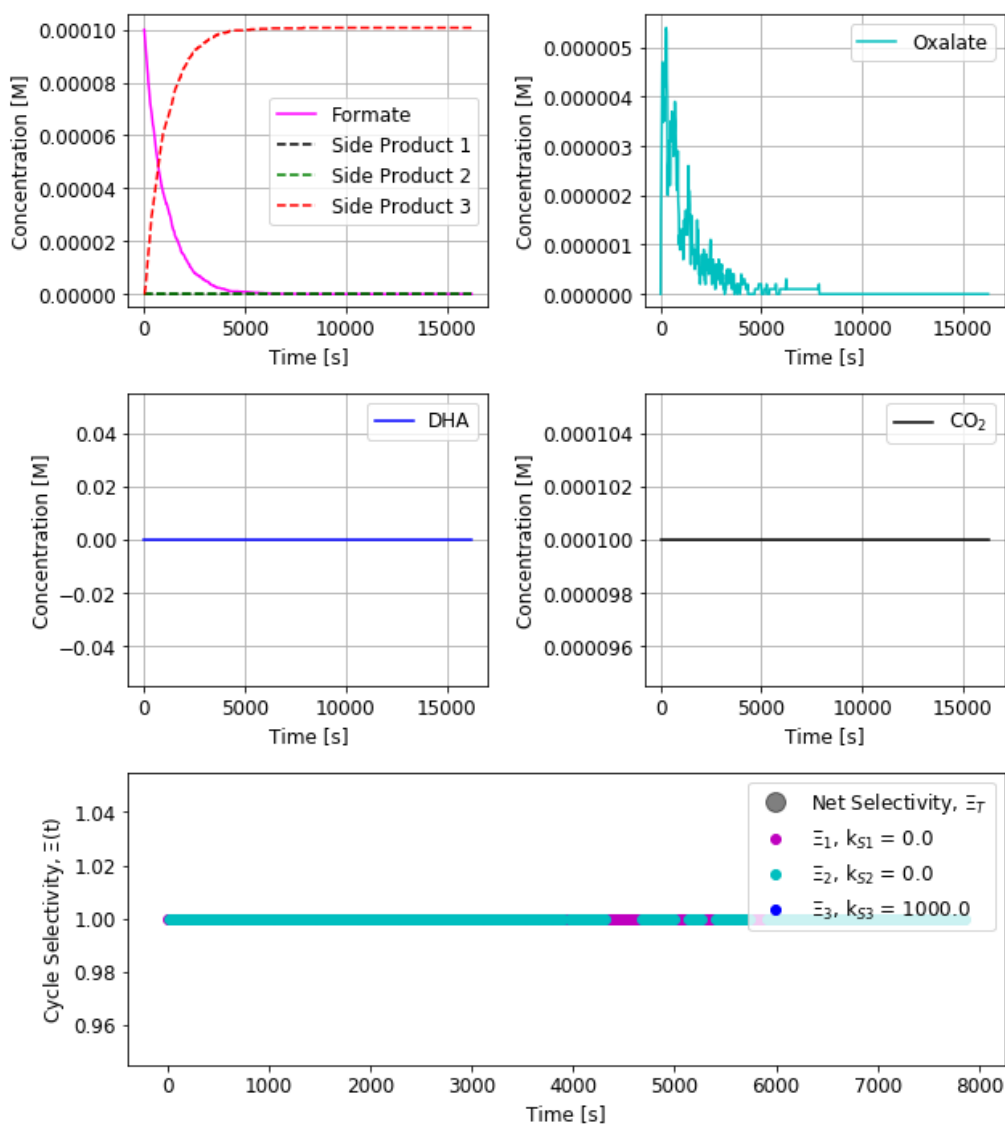


Figure S16 – Basic System

$$k_{s1} = 0.0 \text{ s}^{-1}, k_{s2} = 0.0 \text{ s}^{-1}, k_{s3} = 1000.0 \text{ s}^{-1}$$

Influence of side reactions in step 3 (formate carboxylation). Side reactions are treated as a generic reaction following the rate law $r_{s3} = k_{s3}[\text{DHA}]$. Net selectivity is undefined for times where replication has been arrested, and subsequent reactions only result in the consumption of formate.

S.6 Effects of Batch CO₂ supply

Batch CO₂ reactor

$$[\text{CO}_2]_0 = 10^{-4} \text{ M}$$

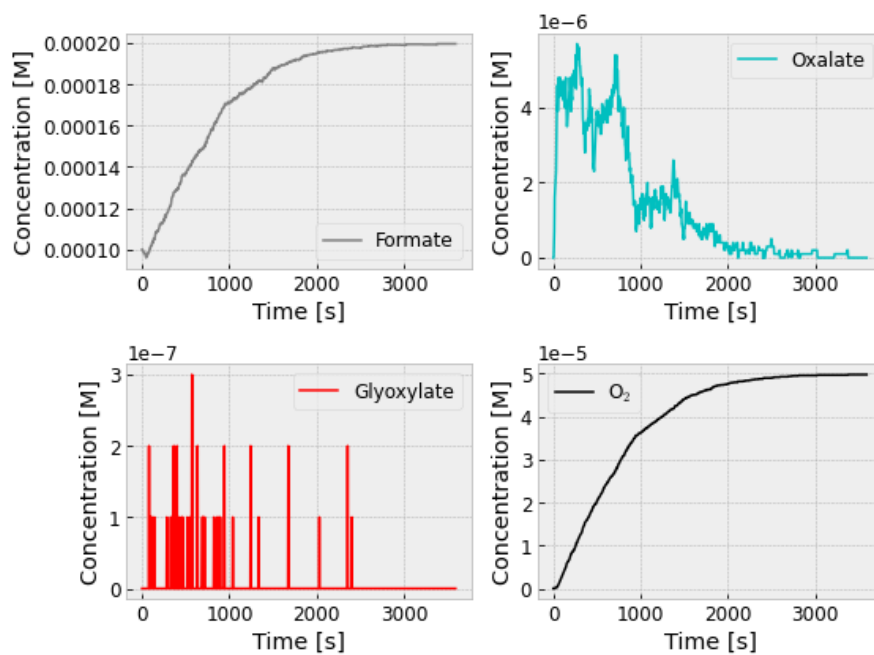


Figure S17 – Basic System

Influence of a batch CO₂ supply on autocatalysis. Initial formate and CO₂ concentrations are 100 μM.

S.7 Rate Constant Sensitivity Analysis of Glyoxylate/DHA Bond Fission (Partial System)

Sensitivities tested (base cases in bold):

Reaction 3a, $\text{DHA} + \text{Cat} \leftrightarrow \text{Cat-DHA}$: $k = 10, \mathbf{100}, 1000 \text{ M}^{-1} \text{ s}^{-1}$
Reaction 3b, $\text{Cat-DHA} \leftrightarrow \text{Cat-DHA}^*$: $k = 100, \mathbf{1000}, 10000 \text{ M}^{-1} \text{ s}^{-1}$
Reaction 3c, $\text{Cat-DHA}^* \leftrightarrow \text{Cat-DHA}^*$: $k = 1, \mathbf{10}, 100 \text{ s}^{-1}$

Reaction 3a (#14): $\text{DHA} + \text{Cat} \leftrightarrow [\text{Cat-DHA}]$

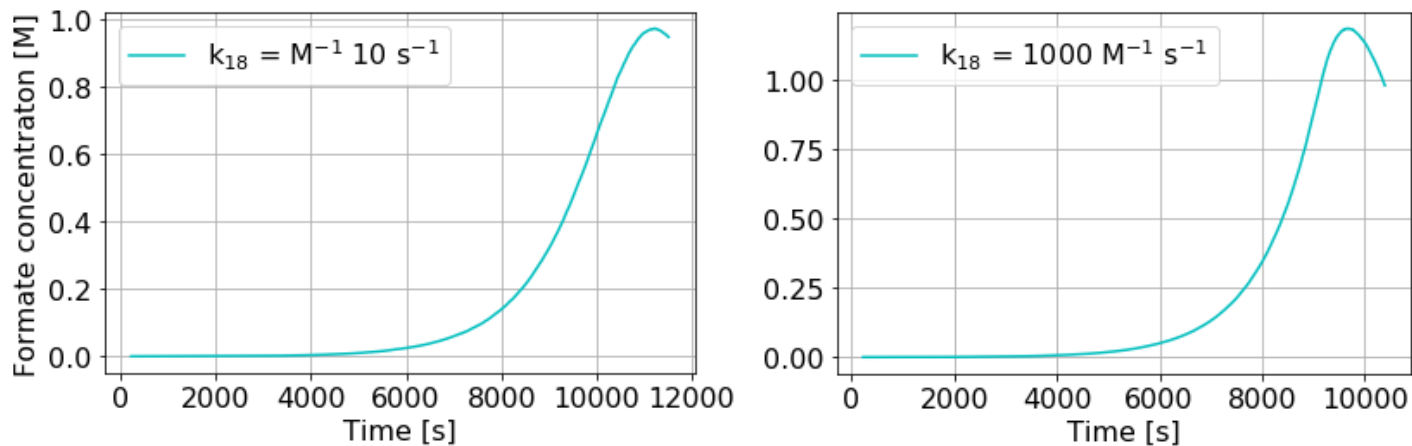


Figure S18

Variance of the forward rate constant for DHA binding to catalyst is shown to yield exponential growth over several orders of magnitude (base case: $k_{18} = 100 \text{ M}^{-1} \text{ s}^{-1}$), with increases in this rate constant leading to overall decreases in the characteristic time for the replication cycle. The values modeled represent very slow rates and weak equilibrium constants (reverse rate constant is $k = 1 \text{ s}^{-1}$) for binding, suggesting the possibility of this replication scheme succeeding even when using a very slow and weakly-binding catalyst.

S.7 Rate Constant Sensitivity Analysis of Glyoxylate/DHA Bond Fission (Partial System)

Reaction 3b (#15): $[\text{Cat-DHA}] + \text{OH}^- \leftrightarrow [\text{Cat-DHA}^*]$

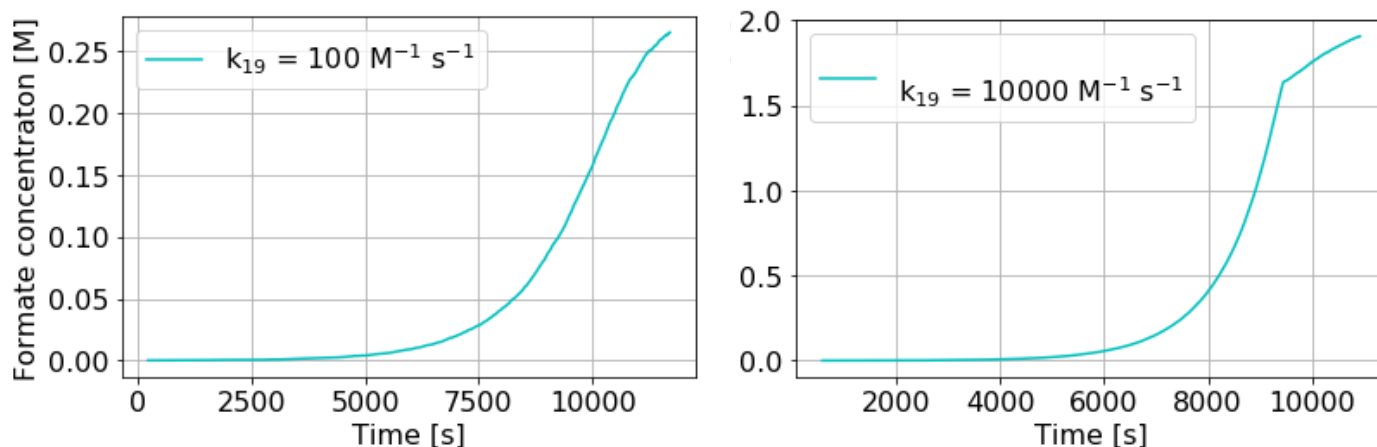


Figure S19

Variance of the forward rate constant for formation of the pre-fission intermediate (DHA*) binding to catalyst; base case: $k_{19} = 1000 \text{ M}^{-1} \text{ s}^{-1}$). The range of values modeled represent relatively slow rates of bimolecular reaction, nevertheless suggesting the possibility of this replication scheme succeeding even when the kinetics of this step are slow.

Reaction 3c (#16): $[\text{Cat-DHA}^*] \rightarrow \text{Cat} + 2 \text{HCO}_2^-$

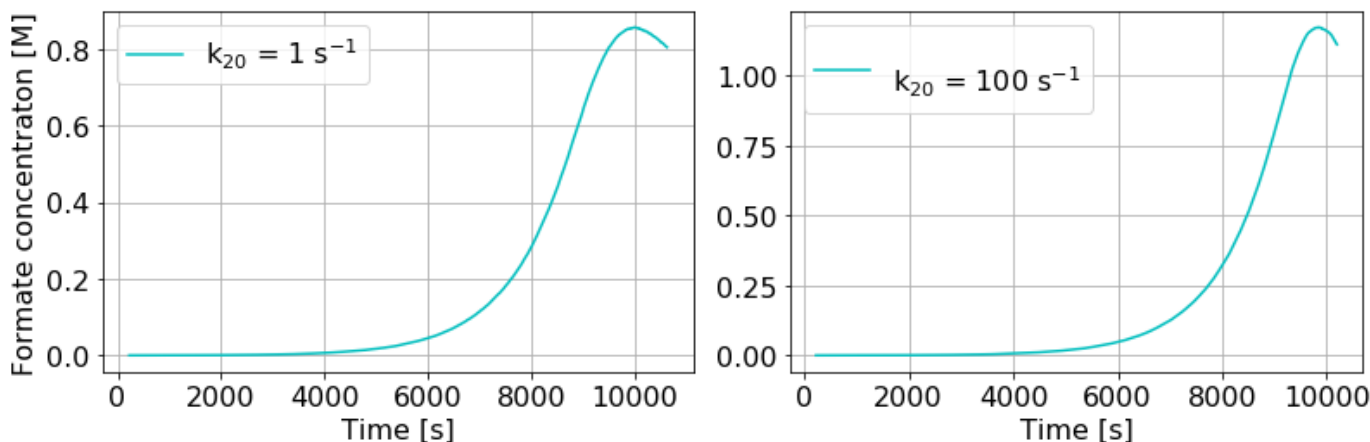


Figure S20

Variance of the forward rate constant for decay of DHA* into two molecules of formate; base case: $k_{20} = 10 \text{ s}^{-1}$). The range of values modeled represent relatively slow rates of first order decays. Despite this, the reaction still exhibits exponential growth kinetics reaction, suggesting the possibility of this replication scheme succeeding even when the kinetics of this step are slow.

S.8 Species Evolution Under VUV Pumping – Steady State Illumination (Full Mechanistic System)

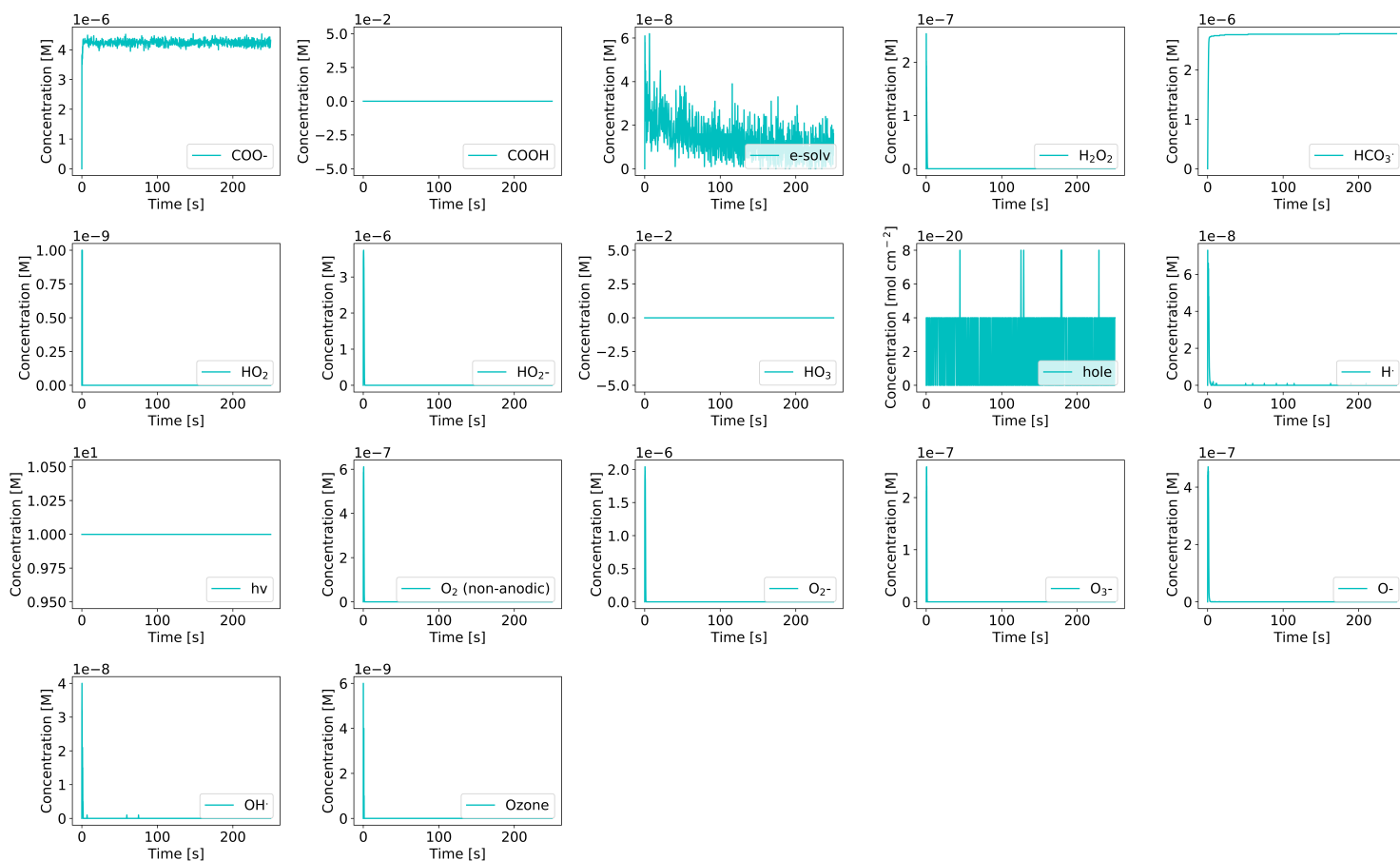


Figure S21

Time evolution of additional species in the Full System under steady-state VUV illumination (remaining species of Figure 6). Behavior of the system with a mechanistic description for all steps, coupled to anodic OER. $[\text{Formate}]_0 = 100 \mu\text{M}$; $[\text{CO}_2]$ is held constant at $100 \mu\text{M}$. The cycle now incorporates VUV-pumped radical mechanisms reported to drive net formate carboxylation to oxalate (step 1).

S.8 Species Evolution Under VUV Pumping – Transient Illumination (Full Mechanistic System)

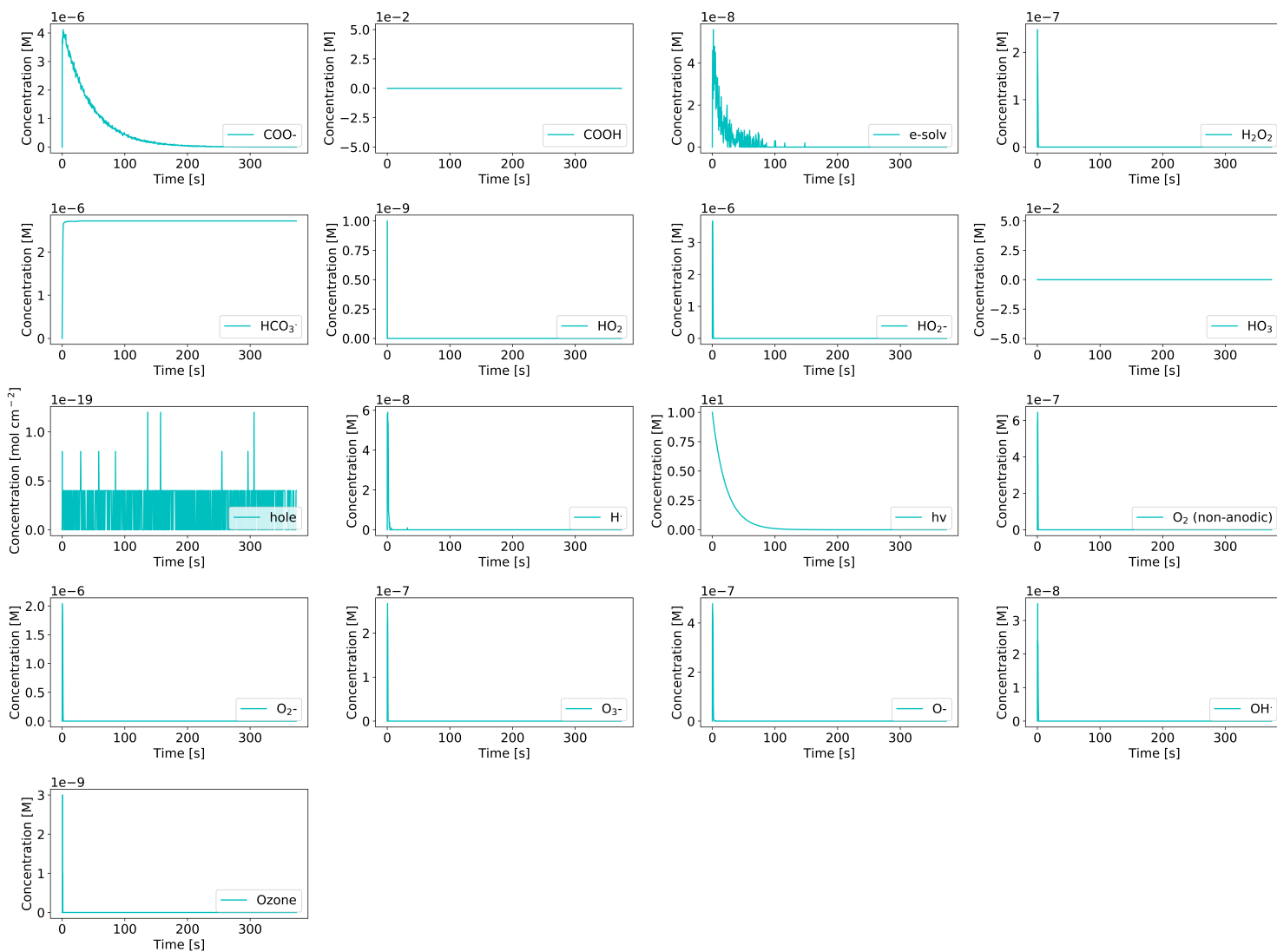


Figure S22

Time evolution of additional species in the Full System modeled under transient VUV illumination (remaining species of Figure 7). Behavior of the system with a mechanistic description for all steps, coupled to anodic OER. $[\text{Formate}]_0 = 100 \mu\text{M}$; $[\text{CO}_2]$ is held constant at $100 \mu\text{M}$. The cycle now incorporates VUV-pumped radical mechanisms reported to drive net formate carboxylation to oxalate (step 1).

S.9 Energy Efficiency of Full Mechanistic System - Steady-State and Transient VUV Pumping

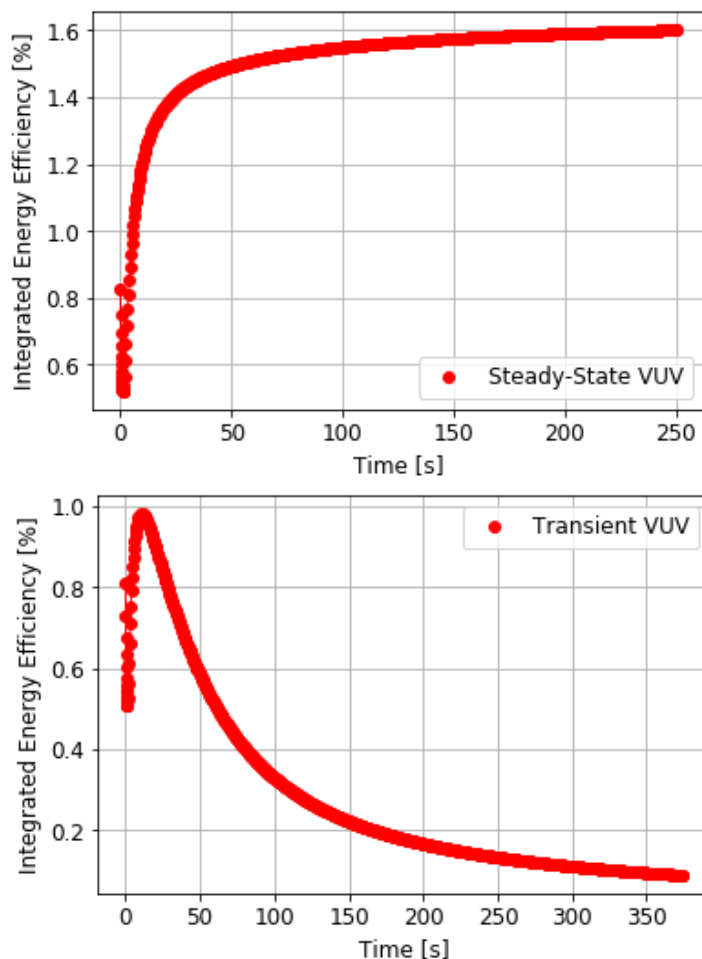


Figure S23

Energy efficiency of autocatalytic fuel conversion under VUV illumination at 124 nm, in the case of steady-state (top) and transient (bottom) illumination. The second point of energy input into the cycle, electrochemical conversion of oxalate to glyoxylate/dihydroxyacetate, is treated as an electrochemical electrolyzer operating at 1.6 V (representing a ~ 300 mV overpotential for oxalate reduction to glyoxylate coupled to water oxidation). Oxalate electrolysis is at steady-state for both illumination cases. Efficiencies are calculated using the free energies of combustion of the main fuel products of the cycle, formate, oxalate, glyoxylate, and hydrogen. The low efficiencies are primarily driven by the high energy photons and their high intensity required for sustaining the formate carboxylation radical reactions used in the fuel replication scheme. Photon concentrations used in these simulations (10 M) correspond to an illumination intensity $n =$ of 0.0464 mol photons cm^{-2} . The rate constant of photon injection ($k_{hv} = 4.5 \times 10^{-4} \text{ s}^{-1}$) sets the required photon flux at this illumination density. Using these values, The VUV illumination power density, P , is calculated according to:

$$P = nN_A k_{hv} \frac{hc}{\lambda}$$

Where h is Planck's constant and c is the speed of light. For $\lambda = 124$ nm, this yields an illumination source power density of 20.2 W cm^{-2} .

S.10 Arrhenius Extrapolation of Measured Formic Acid Decay

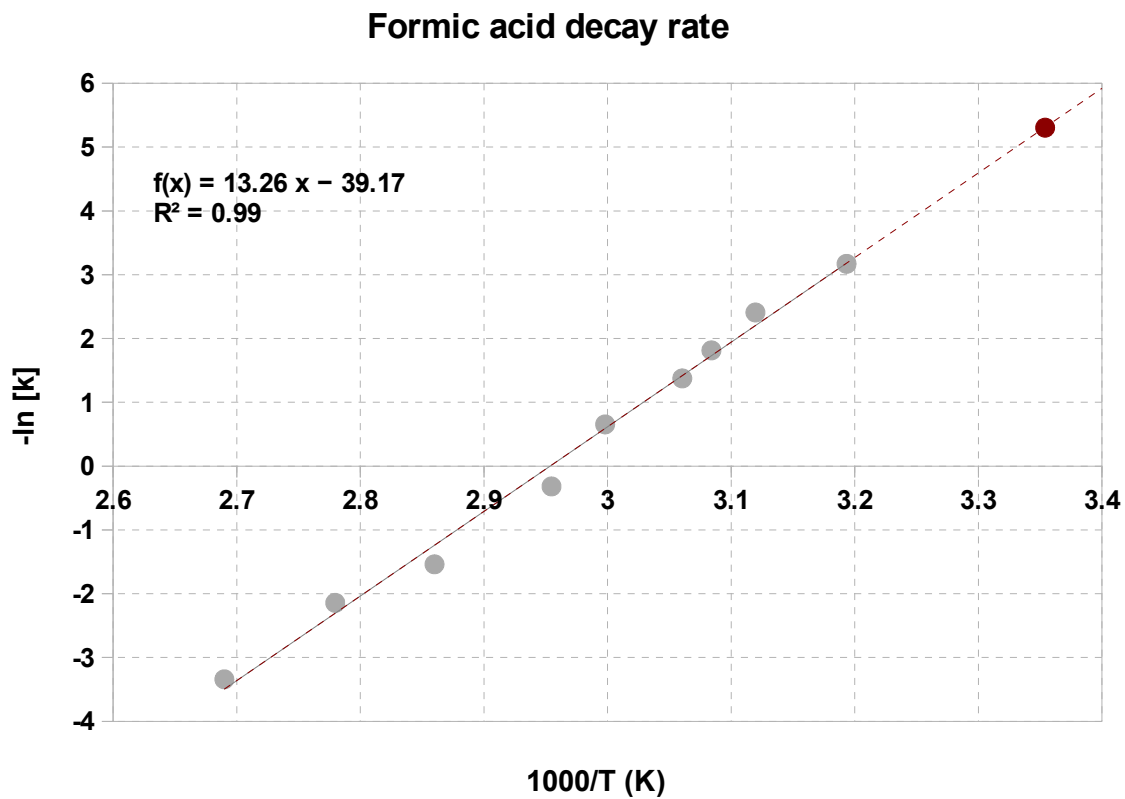


Figure S24

Arrhenius plot of measured formic acid decay into CO and H₂O between 40 and 98.6 °C, adapted from Barham et al¹⁷. Original data are shown as gray dots, with the linear fit shown as a dark line. Linear extrapolation of the Arrhenius relationship to 25 °C is shown as a red dot ($-\ln[k] = 23$; $k_d = 8.3 \times 10^{-11} \text{ s}^{-1}$).

S.11 Glyoxylate Hydrolysis Catalyst Characterization - HPLC

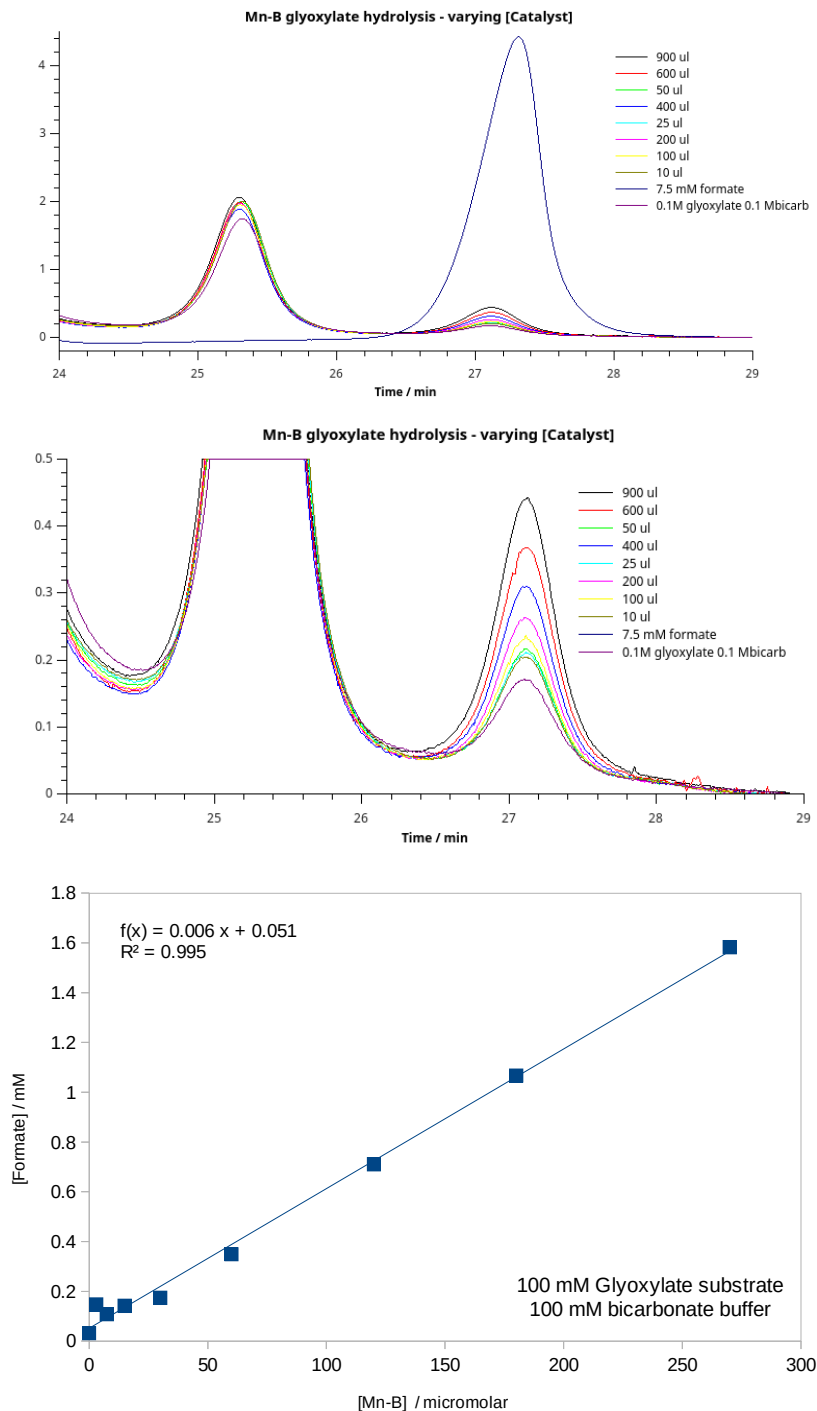


Figure S25

HPLC analysis of mixtures of Mn(Tetraazacyclotetradecane) (Mn-B) complex in a solution of 0.1 M glyoxylate in 0.1 M bicarbonate. Extent of formate evolution displays a direct correlation with the amount of Mn-B catalyst added to the glyoxylate solution, suggestive of Mn-B catalyzing the hydrolytic decomposition of glyoxylate into formate. Future work will characterize the kinetics of this reaction and resolve the stoichiometry of formate evolved with respect to hydrolyzed glyoxylate, as it is also possible that reactions in which glyoxylate is decomposed into 1 equivalent of CO_2 and formate each are occurring.

S.11 Glyoxylate Hydrolysis Catalyst Characterization - UV-Vis

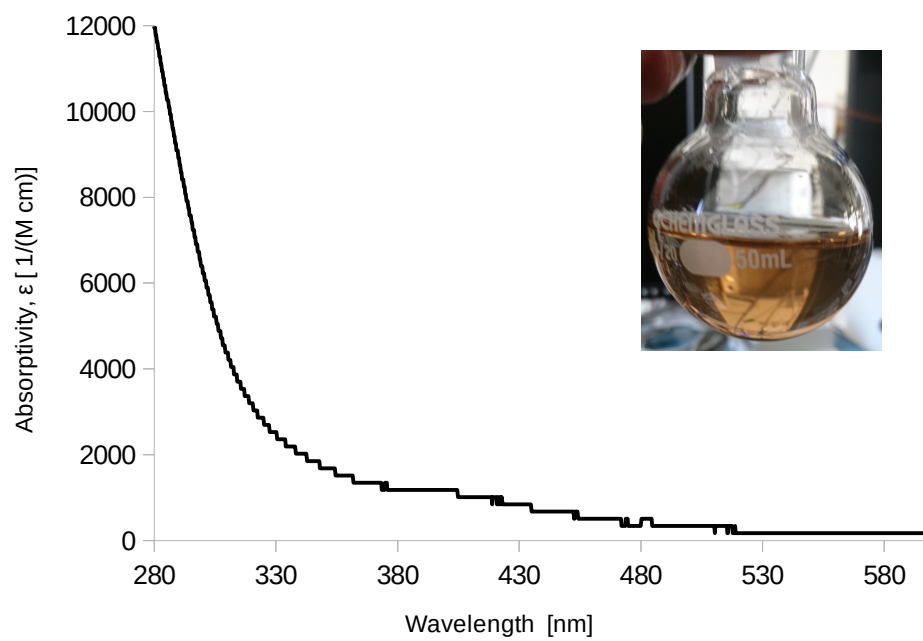


Figure S26

UV-Vis absorption spectroscopy of a 330 μ M solution of Mn(Tetraazacyclotetradecane) complex.

S.12 Putative CO Replication Scheme

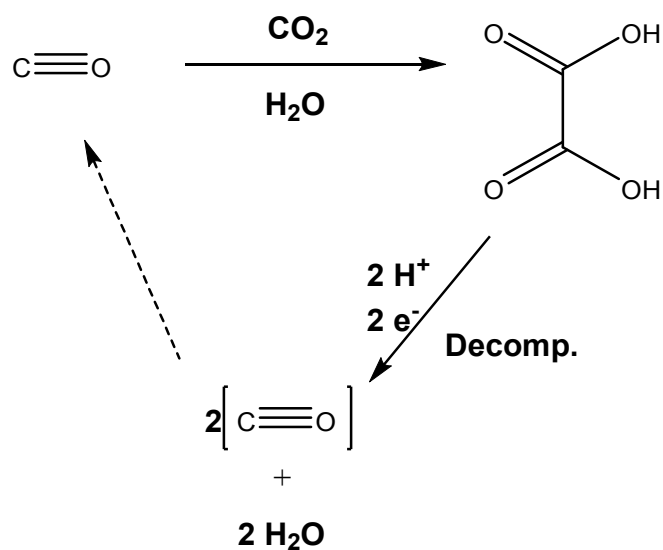


Figure S27

The scheme below represents an example of a potential synthetic route for autocatalytic generation of carbon monoxide, with an exponent base of 2. The reaction as shown is for reactions occurring in acid/neutral conditions, rather than base. Ultimately, a process to yield $2\text{CO} + 2\text{H}_2\text{O}$ through the pathway shown will likely proceed through some metastable intermediate, which is implicit in the unspecified decomposition pathway here. Reaction stoichiometries are only reflected here; mechanistic pathways for the efficient decomposition of oxalate/oxalic acid into CO and H_2O would have to be determined for implementing such a cycle.

S.13 Putative Syngas Replication Scheme

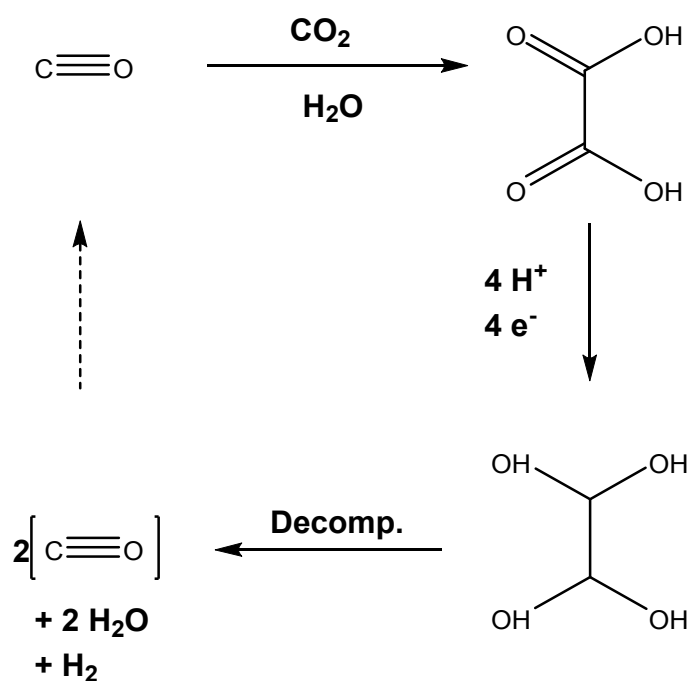


Figure S28

The scheme below represents an example of a potential synthetic route for autocatalytic generation of syngas, with a 2:1 $\text{CO}:\text{H}_2$ ratio yielded at the termination of each cycle (exponent base of 2). The reaction as shown is for reactions occurring in acid/neutral conditions, rather than base. Decomposition of 1,1,2,2-tetrahydroxyethane (THE) to yield $2\text{CO} + \text{H}_2 + 2\text{H}_2\text{O}$ will be required. However the details of how to achieve uniform reduction of oxalate to THE and even more challenging, uniform decomposition of THE to CO , H_2 and H_2O , would require further investigation for implementing this cycle.

S.14 Putative Methanol Replication Scheme

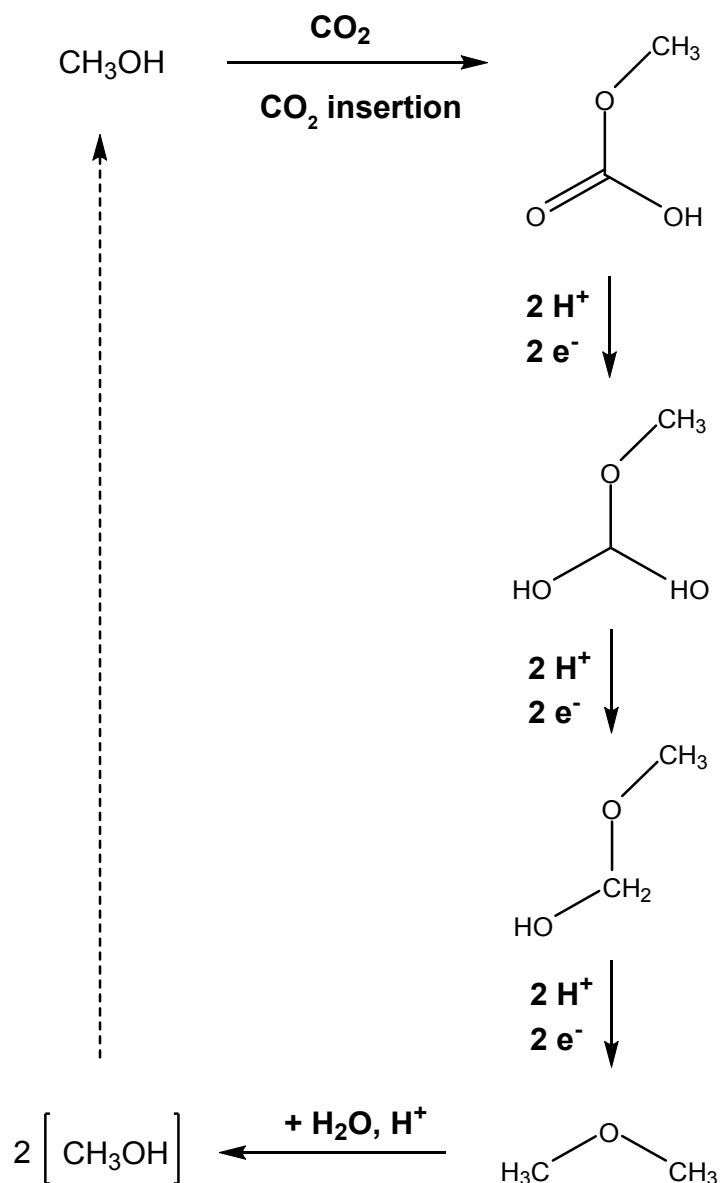


Figure S29

The scheme below represents an example of a potential synthetic route for autocatalytic generation of methanol (exponent base of 2). As a result of methanol being a far more reduced product than CO or formate, the scheme requires three successive, 2-electron reductions before generating an intermediate (dimethyl ether) of the oxidation state and molecular symmetry needed to yield two methanol molecules upon hydrolytic cleavage of the ether bond^{18,19} (acidic conditions shown here). The significant number of steps required in this instance would likely make autocatalytic methanol production far more challenging. Interestingly, depending on the relative rate constants of the cycle, as demonstrated for formate autocatalysis, selection of dimethyl ether (a potential diesel replacement) as a target product, would also be possible, provided that appropriate reaction rates for the individual steps could be realized.

S.15. Kinetiscope Simulation Setup and Parameters – Basic System

System5_basic_reactionscheme_03062024+polyprotic_buffer_100uM_CO2.rxn

Time Units: sec
Temperature Units: °K
Energy Units: kJ
Concentration Units: mole/liter
Pressure Units: atm
Length Units: m

Temperature Option: Constant Temperature
Pressure Option: Constant Pressure
Volume Option: Constant Volume
Temperature: 293.15

This Reaction Scheme Contains the Following Compartments:

Compartment Name: single

This Compartment Contains the Following Reaction Steps:

Equation: Formate + CO2 + H2O => Oxalate + CO2 + H3O
Forward k: 10
This Reaction uses a Nonstandard Rate Law

Equation: Buffer + H3O <=> BufferH1 + H2O
Forward k: 1.0e8
Reverse k: 1.0
This Reaction uses a Nonstandard Rate Law

Equation: BufferH1 + H3O <=> BufferH2 + H2O
Forward k: 1.0e13
Reverse k: 1.0
This Reaction uses a Nonstandard Rate Law

Equation: BufferH1 + OH <=> Buffer + H2O
Forward k: 1.0e6
Reverse k: 1.0
This Reaction uses a Nonstandard Rate Law

Equation: BufferH2 + OH <=> BufferH1 + H2O
Forward k: 1.0e1
Reverse k: 1.0
This Reaction uses a Nonstandard Rate Law

Equation: H3O + OH <=> 2 H2O
Forward k: 1.12e11
Reverse k: 1e-3
This Reaction uses a Nonstandard Rate Law

Equation: Formate => side_product_0
Forward k: 1e-30
This Reaction uses a Standard Rate Law

Equation: 2 Oxalate + 4 H2O => 2 DHA + 2 OH + O2

Forward k: 0.01
This Reaction uses a Nonstandard Rate Law

Equation: Oxalate => side_product_1
Forward k: 1e-30
This Reaction uses a Standard Rate Law

Equation: OH + DHA => 2 Formate + H2O
Forward k: 1000
This Reaction uses a Nonstandard Rate Law

Equation: DHA => side_product_2
Forward k: 1e-30
This Reaction uses a Standard Rate Law

This Compartment Uses the Following Species:

Buffer (initial concentration 1)
BufferH1 (initial concentration 0)
BufferH2 (initial concentration 0)
CO2 (initial concentration 1e-4)
DHA (initial concentration 0)
Formate (initial concentration 1e-4)
H2O (initial concentration 55.4)
H3O (initial concentration 1e-9)
O2 (initial concentration 0)
OH (initial concentration 1e-5)
Oxalate (initial concentration 0)
side_product_0 (initial concentration 0)
side_product_1 (initial concentration 0)
side_product_2 (initial concentration 0)

* * *

Basic System with phosphate and carbonate buffering equilibria

System5_basic_reactionscheme_082724+phosphate+carbonate_buffer_100uM_CO2.rxn

Time Units: sec
Temperature Units: °K
Energy Units: kJ
Concentration Units: mole/liter
Pressure Units: atm
Length Units: m

Temperature Option: Constant Temperature
Pressure Option: Constant Pressure
Volume Option: Constant Volume
Temperature: 293.15

This Reaction Scheme Contains the Following Compartments:

Compartment Name: single

This Compartment Contains the Following Reaction Steps:

Equation: Formate + CO2 + H2O => Oxalate + CO2 + H3O

Forward k: 10
This Reaction uses a Nonstandard Rate Law

Equation: Buffer + H3O <=> BufferH1 + H2O
Forward k: 1.58e7
Reverse k: 1.0
This Reaction uses a Nonstandard Rate Law

Equation: BufferH1 + H3O <=> BufferH2 + H2O
Forward k: 2.38e12
Reverse k: 1.0
This Reaction uses a Nonstandard Rate Law

Equation: BufferH1 + OH <=> Buffer + H2O
Forward k: 6.34e6
Reverse k: 1.0
This Reaction uses a Nonstandard Rate Law

Equation: BufferH2 + OH <=> BufferH1 + H2O
Forward k: 4.21e1
Reverse k: 1.0
This Reaction uses a Nonstandard Rate Law

Equation: CO2 + H2O <=> H2CO3 + CO2
Forward k: 0.04
Reverse k: 12
This Reaction uses a Nonstandard Rate Law

Equation: CO2 + OH <=> HCO3 + CO2
Forward k: 12.1e3
Reverse k: 40e-5
This Reaction uses a Nonstandard Rate Law

Equation: H2CO3 <=> HCO3 + H3O
Forward k: 1e7
Reverse k: 5e10
This Reaction uses a Standard Rate Law

Equation: HCO3 <=> CO32 + H3O
Forward k: 3
Reverse k: 5e10
This Reaction uses a Nonstandard Rate Law

Equation: H3O + OH <=> 2 H2O
Forward k: 1.12e11
Reverse k: 1e-3
This Reaction uses a Nonstandard Rate Law

Equation: Formate => side_product_0
Forward k: 1e-30
This Reaction uses a Standard Rate Law

Equation: 2 Oxalate + 4 H2O => 2 DHA + 2 OH + O2
Forward k: 0.01
This Reaction uses a Nonstandard Rate Law

Equation: Oxalate => side_product_1

Forward k: 1e-30
This Reaction uses a Standard Rate Law

Equation: OH + DHA => 2 Formate + H2O
Forward k: 1000
This Reaction uses a Nonstandard Rate Law

Equation: DHA => side_product_2
Forward k: 1e-30
This Reaction uses a Standard Rate Law

This Compartment Uses the Following Species:

Buffer (initial concentration 1)
BufferH1 (initial concentration 0)
BufferH2 (initial concentration 0)
CO2 (initial concentration 1e-4)
CO32 (initial concentration 0)
DHA (initial concentration 0)
Formate (initial concentration 1e-4)
H2CO3 (initial concentration 0)
H2O (initial concentration 55.4)
H3O (initial concentration 1e-9)
HCO3 (initial concentration 0.01)
O2 (initial concentration 0)
OH (initial concentration 1e-5)
Oxalate (initial concentration 0)
side_product_0 (initial concentration 0)
side_product_1 (initial concentration 0)
side_product_2 (initial concentration 0)

S.16 Simulation 2 – Partial System – Calculation Setup

Reaction Scheme Name:

09032024_Partial_mechanistic_scheme_Final[base_model]_(100uM_formate+CO2+25mM_catalyst)_phosphate+carbonate_buffering_Final.rxn

Time Units: sec

Temperature Units: °K

Energy Units: kJ

Concentration Units: mole/liter

Pressure Units: atm

Length Units: m

Temperature Option: Constant Temperature

Pressure Option: Constant Pressure

Volume Option: Constant Volume

Temperature: 293.15

This Reaction Scheme Contains the Following Compartments:

Compartment Name: single

This Compartment Contains the Following Reaction Steps:

Equation: Formate + CO2 + H2O => Oxalate + CO2 + H3O

Forward k: 10

This Reaction uses a Nonstandard Rate Law

Equation: Buffer + H3O <=> BufferH1 + H2O

Forward k: 1.58e7

Reverse k: 1.0

This Reaction uses a Nonstandard Rate Law

Equation: BufferH1 + H3O <=> BufferH2 + H2O

Forward k: 2.38e12

Reverse k: 1.0

This Reaction uses a Nonstandard Rate Law

Equation: BufferH1 + OH <=> Buffer + H2O

Forward k: 6.34e6

Reverse k: 1.0

This Reaction uses a Nonstandard Rate Law

Equation: BufferH2 + OH <=> BufferH1 + H2O

Forward k: 4.21e1

Reverse k: 1.0

This Reaction uses a Nonstandard Rate Law

Equation: CO2 + H2O <=> H2CO3 + CO2

Forward k: 0.04

Reverse k: 12

This Reaction uses a Nonstandard Rate Law

Equation: CO2 + OH <=> HCO3 + CO2

Forward k: 12.1e3

Reverse k: 40e-5
This Reaction uses a Nonstandard Rate Law

Equation: $\text{H}_2\text{CO}_3 \rightleftharpoons \text{HCO}_3 + \text{H}_3\text{O}$
Forward k: 1e7
Reverse k: 5e10
This Reaction uses a Standard Rate Law

Equation: $\text{HCO}_3 \rightleftharpoons \text{CO}_3^{2-} + \text{H}_3\text{O}$
Forward k: 3
Reverse k: 5e10
This Reaction uses a Nonstandard Rate Law

Equation: $\text{H}_3\text{O} + \text{OH} \rightleftharpoons 2 \text{H}_2\text{O}$
Forward k: 1.12e11
Reverse k: 1.12e-3
This Reaction uses a Nonstandard Rate Law

Equation: $\text{Formate} \Rightarrow \text{side_product}_0$
Forward k: 1e-30
This Reaction uses a Standard Rate Law

Equation: $\text{Oxalate} + \text{A} \rightleftharpoons \text{A-Oxalate_ads}$
Forward k: 2.4
Reverse k: 0.8
This Reaction uses a Nonstandard Rate Law

Equation: $\text{A-Oxalate_ads} + 2 \text{H}_2\text{O} \rightleftharpoons \text{A-GLY_ads} + 3 \text{OH} + 2 \text{hole}$
Forward k: 215
Reverse k: 0.002
This Reaction uses a Nonstandard Rate Law

Equation: $\text{A-GLY_ads} \rightleftharpoons \text{GLY} + \text{A}$
Forward k: 0.8
Reverse k: 2.4
This Reaction uses a Nonstandard Rate Law

Equation: $\text{GLY} + \text{H}_2\text{O} \rightleftharpoons \text{DHA}$
Forward k: 70
Reverse k: 1.14
This Reaction uses a Nonstandard Rate Law

Equation: $4 \text{OH} + 4 \text{hole} \rightleftharpoons 2 \text{H}_2\text{O} + \text{O}_2$
Forward k: 215
Reverse k: 0.002
This Reaction uses a Nonstandard Rate Law

Equation: $\text{Oxalate} \Rightarrow \text{side_product}_1$
Forward k: 1e-30
This Reaction uses a Standard Rate Law

Equation: $\text{DHA} + \text{Cat} \rightleftharpoons \text{Cat-DHA}$
Forward k: 100
Reverse k: 1.0
This Reaction uses a Standard Rate Law

Equation: $\text{Cat-DHA} + \text{OH} \rightleftharpoons \text{Cat-PFI}$

Forward k: 1000
Reverse k: 1.0
This Reaction uses a Standard Rate Law

Equation: Cat-PFI => 2 Formate + H2O + Cat
Forward k: 10
This Reaction uses a Standard Rate Law

Equation: DHA => side_product_2
Forward k: 1e-30
This Reaction uses a Standard Rate Law

This Compartment Uses the Following Species:

A (initial concentration 8300)
A-GLY_ads (initial concentration 0)
A-Oxalate_ads (initial concentration 0)
Buffer (initial concentration 1)
BufferH1 (initial concentration 0)
BufferH2 (initial concentration 0)
Cat (initial concentration 2.5e-2)
Cat-DHA (initial concentration 0)
Cat-PFI (initial concentration 0)
CO2 (initial concentration 1e-4)
CO32 (initial concentration 0)
DHA (initial concentration 0)
Formate (initial concentration 1e-4)
GLY (initial concentration 0)
H2CO3 (initial concentration 0)
H2O (initial concentration 55.4)
H3O (initial concentration 1e-9)
HCO3 (initial concentration 0.01)
hole (initial concentration 0)
O2 (initial concentration 0)
OH (initial concentration 1e-5)
Oxalate (initial concentration 0)
side_product_0 (initial concentration 0)
side_product_1 (initial concentration 0)
side_product_2 (initial concentration 0)

This Reaction Scheme Contains the Following Species/Property Definitions:

Species Name: A
Species Name: A-GLY_ads
Species Name: A-Oxalate_ads
Species Name: Buffer
Species Name: BufferH1
Species Name: BufferH2
Species Name: Cat
Species Name: Cat-DHA
Species Name: Cat-PFI
Species Name: CO2
Species Name: CO32
Species Name: DHA
Species Name: Formate
Species Name: GLY

Species Name: H2CO3
Species Name: H2O
Species Name: H3O
Species Name: HCO3
Species Name: hole
Species Name: O2
Species Name: OH
Species Name: Oxalate
Species Name: side_product_0
Species Name: side_product_1
Species Name: side_product_2

S.17 Simulation 3 – Full System (Steady-state) – Calculation Setup

Reaction Scheme Name:

Full_mechanistic_scheme_082224+Pastina_model_VUV_initiation(124nm)_100uM_CO2_v2_steady-state_light+H2O_phosphate+carbonate_buffering.rxn

Time Units: sec

Temperature Units: °K

Energy Units: kJ

Concentration Units: mole/liter

Pressure Units: atm

Length Units: m

Temperature Option: Constant Temperature

Pressure Option: Constant Pressure

Volume Option: Constant Volume

Temperature: 293.15

This Reaction Scheme Contains the Following Compartments:

Compartment Name: single

This Compartment Contains the Following Reaction Steps:

Equation: $\text{H}_2\text{O} + \text{h}\nu \Rightarrow \text{Hrad} + \text{OHrad} + \text{h}\nu$

Forward k: $0.045\text{e-}2$

This Reaction uses a Nonstandard Rate Law

Equation: $6 \text{H}_2\text{O} + 100 \text{h}\nu \Rightarrow 6 \text{esolv} + 100 \text{h}\nu$

Forward k: $0.045\text{e-}2$

This Reaction uses a Nonstandard Rate Law

Equation: $\text{Formate} + \text{Hrad} \Rightarrow \text{COO} + \text{H}_2$

Forward k: $2.2\text{e}8$

This Reaction uses a Standard Rate Law

Equation: $\text{Formate} + \text{OHrad} \Rightarrow \text{COO} + \text{H}_2\text{O}$

Forward k: $2.5\text{e}9$

This Reaction uses a Nonstandard Rate Law

Equation: $\text{Formate} + \text{esolv} \Rightarrow \text{COO} + \text{H}_2 + \text{OH}$

Forward k: $1.0\text{e}6$

This Reaction uses a Standard Rate Law

Equation: $\text{CO}_2 + \text{OHrad} \Rightarrow \text{HCO}_3\text{rad} + \text{CO}_2$

Forward k: $1.0\text{e}6$

This Reaction uses a Standard Rate Law

Equation: $\text{CO}_2 + \text{Hrad} \Rightarrow \text{COOH} + \text{CO}_2$

Forward k: $8.0\text{e}6$

This Reaction uses a Standard Rate Law

Equation: $\text{COOH} + \text{H}_2\text{O} \rightleftharpoons \text{H}_3\text{O} + \text{COO}$

Forward k: $3.98\text{e}7$

Reverse k: $1.0\text{e}9$

This Reaction uses a Nonstandard Rate Law

Equation: $\text{CO}_2 + \text{esolv} \Rightarrow \text{COO} + \text{CO}_2$

Forward k: 7.7e9
This Reaction uses a Standard Rate Law

Equation: 2 COO => Oxalate
Forward k: 1.0e9
This Reaction uses a Standard Rate Law

Equation: Buffer + H3O <=> BufferH1 + H2O
Forward k: 1.58e7
Reverse k: 1.0
This Reaction uses a Nonstandard Rate Law

Equation: BufferH1 + H3O <=> BufferH2 + H2O
Forward k: 2.38e12
Reverse k: 1.0
This Reaction uses a Nonstandard Rate Law

Equation: BufferH1 + OH <=> Buffer + H2O
Forward k: 6.34e6
Reverse k: 1.0
This Reaction uses a Nonstandard Rate Law

Equation: BufferH2 + OH <=> BufferH1 + H2O
Forward k: 4.21e1
Reverse k: 1.0
This Reaction uses a Nonstandard Rate Law

Equation: H3O + OH <=> 2 H2O
Forward k: 1.12e11
Reverse k: 1.12e-3
This Reaction uses a Nonstandard Rate Law

Equation: Formate => side_product_0
Forward k: 1e-30
This Reaction uses a Standard Rate Law

Equation: Oxalate + A <=> A-Oxalate_ads
Forward k: 2.4
Reverse k: 0.8
This Reaction uses a Nonstandard Rate Law

Equation: A-Oxalate_ads + 2 H2O <=> A-GLY_ads + 3 OH + 2 hole
Forward k: 215
Reverse k: .002
This Reaction uses a Nonstandard Rate Law

Equation: A-GLY_ads <=> GLY + A
Forward k: 0.8
Reverse k: 2.4
This Reaction uses a Nonstandard Rate Law

Equation: GLY + H2O <=> DHA
Forward k: 70
Reverse k: 1.14
This Reaction uses a Nonstandard Rate Law

Equation: 4 OH + 4 hole <=> 2 H2O + O2_anode

Forward k: 215
Reverse k: .002
This Reaction uses a Nonstandard Rate Law

Equation: Oxalate => side_product_1
Forward k: 1e-30
This Reaction uses a Standard Rate Law

Equation: DHA + Cat <=> Cat-DHA
Forward k: 100
Reverse k: 1.0
This Reaction uses a Standard Rate Law

Equation: Cat-DHA + OH <=> Cat-PFI
Forward k: 1000
Reverse k: 1.0
This Reaction uses a Standard Rate Law

Equation: Cat-PFI => 2 Formate + H2O + Cat
Forward k: 10
This Reaction uses a Standard Rate Law

Equation: DHA => side_product_2
Forward k: 1e-30
This Reaction uses a Standard Rate Law

***The steps below mark the detailed VUV-initiated radical processes for driving net formate carboxylation to oxalate, taken from Domanich et al., and Pastina et al^{8,9}.

Equation: H2O2 + H2O => H3O + HO2_minus
Forward k: 9.43e-2
This Reaction uses a Nonstandard Rate Law

Equation: H3O + HO2_minus => H2O2 + H2O
Forward k: 5.02e10
This Reaction uses a Standard Rate Law

Equation: H2O2 + OH => HO2_minus + H2O
Forward k: 1.33e10
This Reaction uses a Standard Rate Law

Equation: HO2_minus + H2O => H2O2 + OH
Forward k: 1.27e6
This Reaction uses a Nonstandard Rate Law

Equation: esolv + H2O => Hrad + OH
Forward k: 15.75
This Reaction uses a Nonstandard Rate Law

Equation: Hrad + OH => esolv + H2O
Forward k: 2.44e7
This Reaction uses a Standard Rate Law

Equation: Hrad + H2O => esolv + H3O
Forward k: 5.83
This Reaction uses a Nonstandard Rate Law

Equation: $\text{esolv} + \text{H3O} \Rightarrow \text{Hrad} + \text{H2O}$
Forward k: 2.09e10
This Reaction uses a Standard Rate Law

Equation: $\text{OHrad} + \text{OH} \Rightarrow \text{O_minus} + \text{H2O}$
Forward k: 1.33e10
This Reaction uses a Standard Rate Law

Equation: $\text{O_minus} + \text{H2O} \Rightarrow \text{OHrad} + \text{OH}$
Forward k: 1.27e6
This Reaction uses a Nonstandard Rate Law

Equation: $\text{OHrad} + \text{H2O} \Rightarrow \text{O_minus} + \text{H3O}$
Forward k: 9.43e-2
This Reaction uses a Nonstandard Rate Law

Equation: $\text{O_minus} + \text{H3O} \Rightarrow \text{OHrad} + \text{H2O}$
Forward k: 5.02e10
This Reaction uses a Standard Rate Law

Equation: $\text{H02} + \text{H2O} \Rightarrow \text{O2_minus} + \text{H3O}$
Forward k: 7.73e5
This Reaction uses a Nonstandard Rate Law

Equation: $\text{O2_minus} + \text{H3O} \Rightarrow \text{H02} + \text{H2O}$
Forward k: 5.02e10
This Reaction uses a Standard Rate Law

Equation: $\text{H02} + \text{OH} \Rightarrow \text{O2_minus} + \text{H2O}$
Forward k: 1.33e10
This Reaction uses a Standard Rate Law

Equation: $\text{O2_minus} + \text{H2O} \Rightarrow \text{H02} + \text{OH}$
Forward k: 1.55e-1
This Reaction uses a Nonstandard Rate Law

Equation: $\text{esolv} + \text{OHrad} \Rightarrow \text{OH}$
Forward k: 3.55e10
This Reaction uses a Standard Rate Law

Equation: $\text{esolv} + \text{H2O2} \Rightarrow \text{OHrad} + \text{OH}$
Forward k: 1.36e10
This Reaction uses a Standard Rate Law

Equation: $\text{esolv} + \text{O2_minus} + \text{H2O} \Rightarrow \text{H02_minus} + \text{OH}$
Forward k: 1.30e10
This Reaction uses a Nonstandard Rate Law

Equation: $\text{esolv} + \text{H02} \Rightarrow \text{H02_minus}$
Forward k: 1.30e10
This Reaction uses a Standard Rate Law

Equation: $\text{esolv} + \text{O2} \Rightarrow \text{O2_minus}$
Forward k: 2.29e10
This Reaction uses a Standard Rate Law

Equation: $2 \text{ esolv} + 2 \text{ H2O} \Rightarrow \text{H2} + 2 \text{ OH}$
Forward k: 7.26e9
This Reaction uses a Nonstandard Rate Law

Equation: $\text{esolv} + \text{Hrad} + \text{H2O} \Rightarrow \text{H2} + \text{OH}$
Forward k: 2.76e10
This Reaction uses a Nonstandard Rate Law

Equation: $\text{esolv} + \text{H02_minus} \Rightarrow \text{O_minus} + \text{OH}$
Forward k: 3.50e9
This Reaction uses a Standard Rate Law

Equation: $\text{esolv} + \text{O_minus} + \text{H2O} \Rightarrow 2 \text{ OH}$
Forward k: 2.20e10
This Reaction uses a Nonstandard Rate Law

Equation: $\text{esolv} + \text{O3_minus} + \text{H2O} \Rightarrow \text{O2} + 2 \text{ OH}$
Forward k: 1.60e10
This Reaction uses a Nonstandard Rate Law

Equation: $\text{esolv} + \text{Ozone} \Rightarrow \text{O3_minus}$
Forward k: 3.60e10
This Reaction uses a Standard Rate Law

Equation: $\text{Hrad} + \text{H2O} \Rightarrow \text{H2} + \text{OHrad}$
Forward k: 4.58e-5
This Reaction uses a Nonstandard Rate Law

Equation: $\text{Hrad} + \text{O_minus} \Rightarrow \text{OH}$
Forward k: 1e10
This Reaction uses a Standard Rate Law

Equation: $\text{Hrad} + \text{H02_minus} \Rightarrow \text{OHrad} + \text{OH}$
Forward k: 9.00e7
This Reaction uses a Standard Rate Law

Equation: $\text{Hrad} + \text{O3_minus} \Rightarrow \text{OH} + \text{O2}$
Forward k: 1.0e10
This Reaction uses a Standard Rate Law

Equation: $2 \text{ Hrad} \Rightarrow \text{H2}$
Forward k: 5.14e9
This Reaction uses a Standard Rate Law

Equation: $\text{Hrad} + \text{OHrad} \Rightarrow \text{H2O}$
Forward k: 1.09e10
This Reaction uses a Standard Rate Law

Equation: $\text{Hrad} + \text{H2O2} \Rightarrow \text{OHrad} + \text{H2O}$
Forward k: 3.65e7
This Reaction uses a Standard Rate Law

Equation: $\text{Hrad} + \text{O2} \Rightarrow \text{H02}$
Forward k: 1.31e10
This Reaction uses a Standard Rate Law

Equation: $\text{Hrad} + \text{H02} \Rightarrow \text{H2O2}$

Forward k: 1.14e10
This Reaction uses a Standard Rate Law

Equation: Hrad + O2_minus => H02_minus
Forward k: 1.14e10
This Reaction uses a Standard Rate Law

Equation: Hrad + Ozone => H03
Forward k: 3.80e10
This Reaction uses a Standard Rate Law

Equation: 2 OHrad => H2O2
Forward k: 4.81e9
This Reaction uses a Standard Rate Law

Equation: OHrad + H02 => H2O + O2
Forward k: 8.84e9
This Reaction uses a Standard Rate Law

Equation: OHrad + O2_minus => OH + O2
Forward k: 1.1e10
This Reaction uses a Standard Rate Law

Equation: OHrad + H2 => Hrad + H2O
Forward k: 3.95e7
This Reaction uses a Standard Rate Law

Equation: OHrad + H2O2 => H02 + H2O
Forward k: 2.92e7
This Reaction uses a Standard Rate Law

Equation: OHrad + O_minus => H02_minus
Forward k: 2.50e10
This Reaction uses a Standard Rate Law

Equation: OHrad + H02_minus => H02 + OH
Forward k: 7.5e9
This Reaction uses a Standard Rate Law

Equation: OHrad + O3_minus => Ozone + OH
Forward k: 2.60e9
This Reaction uses a Standard Rate Law

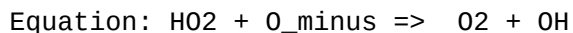
Equation: OHrad + O3_minus + H2O => 2 O2_minus + H3O
Forward k: 6.0e9
This Reaction uses a Nonstandard Rate Law

Equation: OHrad + Ozone => H02 + O2
Forward k: 1.1e8
This Reaction uses a Standard Rate Law

Equation: H02 + O2_minus => H02_minus + O2
Forward k: 8.0e7
This Reaction uses a Standard Rate Law

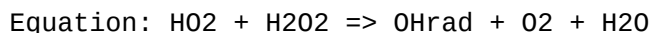
Equation: 2 H02 => H2O2 + O2
Forward k: 8.4e5

This Reaction uses a Standard Rate Law



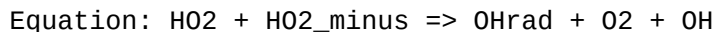
Forward k: 6.0e9

This Reaction uses a Standard Rate Law



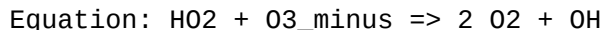
Forward k: 0.5

This Reaction uses a Standard Rate Law



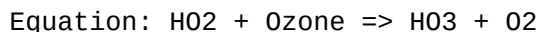
Forward k: 0.5

This Reaction uses a Standard Rate Law



Forward k: 6.0e9

This Reaction uses a Standard Rate Law



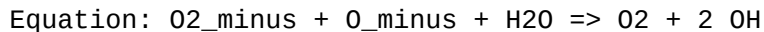
Forward k: 5.0e8

This Reaction uses a Standard Rate Law



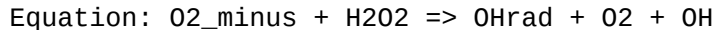
Forward k: 0.3

This Reaction uses a Nonstandard Rate Law



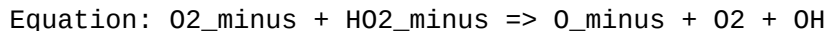
Forward k: 6.0e8

This Reaction uses a Nonstandard Rate Law



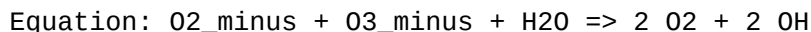
Forward k: 0.13

This Reaction uses a Standard Rate Law



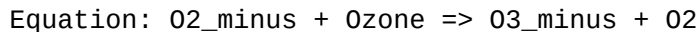
Forward k: 0.13

This Reaction uses a Standard Rate Law



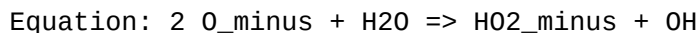
Forward k: 1.0e4

This Reaction uses a Nonstandard Rate Law



Forward k: 1.5e9

This Reaction uses a Standard Rate Law



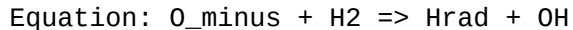
Forward k: 1.0e9

This Reaction uses a Nonstandard Rate Law



Forward k: 3.75e9

This Reaction uses a Standard Rate Law



Forward k: 1.28e8

This Reaction uses a Standard Rate Law

Equation: $O_{\text{minus}} + H2O2 \Rightarrow O2_{\text{minus}} + H2O$
Forward k: 5.0e8
This Reaction uses a Standard Rate Law

Equation: $O_{\text{minus}} + H2O_{\text{minus}} \Rightarrow O2_{\text{minus}} + OH$
Forward k: 7.86e8
This Reaction uses a Standard Rate Law

Equation: $O_{\text{minus}} + O3_{\text{minus}} \Rightarrow 2 O2_{\text{minus}}$
Forward k: 7.0e8
This Reaction uses a Standard Rate Law

Equation: $O_{\text{minus}} + Ozone \Rightarrow O2_{\text{minus}} + O2$
Forward k: 5.0e9
This Reaction uses a Standard Rate Law

Equation: $O3_{\text{minus}} \Rightarrow O2 + O_{\text{minus}}$
Forward k: 2.62e3
This Reaction uses a Standard Rate Law

Equation: $O3_{\text{minus}} + H3O \Rightarrow O2 + OH_{\text{rad}} + H2O$
Forward k: 9.0e10
This Reaction uses a Standard Rate Law

Equation: $H03 \Rightarrow O2 + OH_{\text{rad}}$
Forward k: 1.10e5
This Reaction uses a Standard Rate Law

***The steps below incorporate the use of an H2O reservoir input and reactions for carbonate buffering equilibria.

Equation: $reservoir \Rightarrow H2O + reservoir$
Forward k: .025
This Reaction uses a Nonstandard Rate Law

Equation: $C02 + H2O \rightleftharpoons H2C03 + C02$
Forward k: 0.04
Reverse k: 12
This Reaction uses a Nonstandard Rate Law

Equation: $C02 + OH \rightleftharpoons HC03 + C02$
Forward k: 12.1e3
Reverse k: 40e-5
This Reaction uses a Nonstandard Rate Law

Equation: $H2C03 \rightleftharpoons HC03 + H3O$
Forward k: 1e7
Reverse k: 5e10
This Reaction uses a Standard Rate Law

Equation: $HC03 \rightleftharpoons C032 + H3O$
Forward k: 3
Reverse k: 5e10
This Reaction uses a Nonstandard Rate Law

This Compartment Uses the Following Species:

A (initial concentration 8300)
A-GLY_ads (initial concentration 0)
A-oxalate_ads (initial concentration 0)
Buffer (initial concentration 1)
BufferH1 (initial concentration 0)
BufferH2 (initial concentration 0)
Cat (initial concentration 2.5e-2)
Cat-DHA (initial concentration 0)
Cat-PFI (initial concentration 0)
CO2 (initial concentration 1e-4)
CO32 (initial concentration 0)
COO (initial concentration 0)
COOH (initial concentration 0)
DHA (initial concentration 0)
esolv (initial concentration 0)
Formate (initial concentration 1e-4)
GLY (initial concentration 0)
H2 (initial concentration 0)
H2CO3 (initial concentration 0)
H2O (initial concentration 55.4)
H2O2 (initial concentration 0)
H3O (initial concentration 1e-9)
HCO3 (initial concentration 0.01)
HCO3rad (initial concentration 0)
HO2 (initial concentration 0)
HO2_minus (initial concentration 0)
HO3 (initial concentration 0)
hole (initial concentration 0)
Hrad (initial concentration 0)
hv (initial concentration 10)
O2 (initial concentration 0)
O2_anode (initial concentration 0)
O2_minus (initial concentration 0)
O3_minus (initial concentration 0)
O_minus (initial concentration 0)
OH (initial concentration 1e-5)
OHrad (initial concentration 0)
Oxalate (initial concentration 0)
Ozone (initial concentration 0)
reservoir (initial concentration 55.4)
side_product_0 (initial concentration 0)
side_product_1 (initial concentration 0)
side_product_2 (initial concentration 0)

This Reaction Scheme Contains the Following Species/Property Definitions:

Species Name: A
Species Name: A-GLY_ads
Species Name: A-oxalate_ads

Species Name: Buffer
Species Name: BufferH1
Species Name: BufferH2
Species Name: Cat
Species Name: Cat-DHA

Species Name: Cat-PFI
Species Name: CO2
Species Name: CO32
Species Name: CO0
Species Name: COOH
Species Name: DHA
Species Name: esolv
Species Name: Formate
Species Name: GLY
Species Name: H2
Species Name: H2CO3
Species Name: H2O
Species Name: H2O2
Species Name: H3O
Species Name: HCO3
Species Name: HCO3rad
Species Name: HO2
Species Name: HO2_minus
Species Name: HO3
Species Name: hole
Species Name: Hrad
Species Name: hv
Species Name: O2
Species Name: O2_anode
Species Name: O2_minus
Species Name: O3_minus
Species Name: O_minus
Species Name: OH
Species Name: OHrad
Species Name: Oxalate
Species Name: Ozone
Species Name: reservoir
Species Name: side_product_0
Species Name: side_product_1
Species Name: side_product_2

Simulation 3 – Full System (Transient Illumination, Batch H₂O) – Calculation Setup

Equation: reservoir => H2O + reservoir

Forward k: 0 (M s⁻¹)

This Reaction uses a Standard Rate Law

Equation: H2O + hv => Hrad + ORad

Forward k: 0.045e-2

This Reaction uses a Nonstandard Rate Law

Equation: 6 H2O + 100 hv => 6 esolv

Forward k: 0.045e-2

This Reaction uses a Nonstandard Rate Law

→ All subsequent steps are identical to the Full System, steady-state.

S.18 Calculation of Radiolysis Rates and Rate Constants from Nuclear Decay Source G Values

Species	10 MeV proton G values	Flux (mol/sec) from 50 μ A beam current
$e^-_{(aq)}$	0.9	4.66E-05
H \cdot	0.57	2.95E-05
H $_2$	0.64	3.32E-05
OH \cdot	1.18	6.11E-05
H $_2$ O $_2$	0.74	3.83E-05
HO $_2$	0.03	1.55E-06
H $^+$	1.1	5.70E-05
OH $-$	0.2	1.04E-05

Species	2 MeV proton G values	Flux (mol/sec) from 50 μ A beam current
$e^-_{(aq)}$	0.3	1.55E-05
H \cdot	0.2	1.04E-05
H $_2$	0.9	4.66E-05
OH \cdot	0.63	3.26E-05
H $_2$ O $_2$	0.76	3.94E-05
HO $_2$	0.05	2.59E-06
H $^+$	0.36	1.87E-05
OH $-$	0.06	3.11E-06

Species	10 MeV γ ray G values	Flux (mol/sec) from 50 μ A beam current
$e^-_{(aq)}$	2.6	1.35E-04
H \cdot	0.66	3.42E-05
H $_2$	0.45	2.33E-05
OH \cdot	2.7	1.40E-04
H $_2$ O $_2$	0.7	3.63E-05
HO $_2$	0.02	1.04E-06
H $^+$	3.1	1.61E-04
OH $-$	0.5	2.59E-05

Table S1

Rates of production for primary products of radiolysis of water from irradiation by 10 MeV protons, 2 MeV protons and 2 MeV gamma rays as described by Pastina et al. Fluxes of the generated species are calculated assuming irradiation beam currents of 50 μ A. G values describe the number of primary species products generated per particle emission.

Example results for substitution of primary OH \cdot , H \cdot and $e^-_{(aq)}$ production VUV illumination for these radiolytic processes are shown below. These substitutions, with the G values reported for these particular radiolytic sources at 10 MeV and 2 MeV, fail to result in autocatalytic formate evolution. However, tuning radiolytic sources appropriately, such that their G values for H \cdot , OH \cdot , and $e^-_{(aq)}$ approach the quantum efficiencies of those species yields under VUV illumination, may possibly allow the use of radiolytic sources, such as depleted nuclear wastes, in this autocatalytic cycle.

S.18 Calculation of Radiolysis Rates and Rate Constants from Nuclear Decay Source G Values
- Simulation of Autocatalysis Driven by Radiolysis from Nuclear Decays ($^1\text{H}^+$ irradiation).

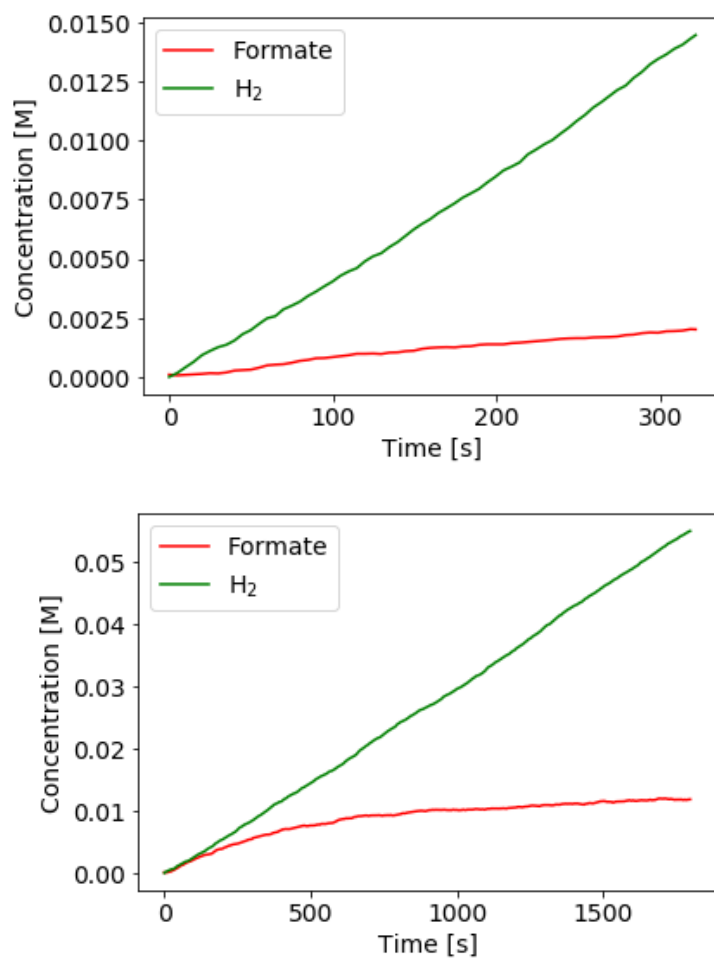


Figure S30

(Top) Formate autocatalysis simulated for radiolysis using 2 MeV proton irradiation, at a 50 μA particle flux.

(Bottom) Formate autocatalysis simulated for radiolysis using 10 MeV proton irradiation, at a 50 μA particle flux.

S.18 Calculation of Radiolysis Rates and Rate Constants from Nuclear Decay Source G Values
- Simulation of Autocatalysis Driven by Radiolysis from Nuclear Decays (γ rays).

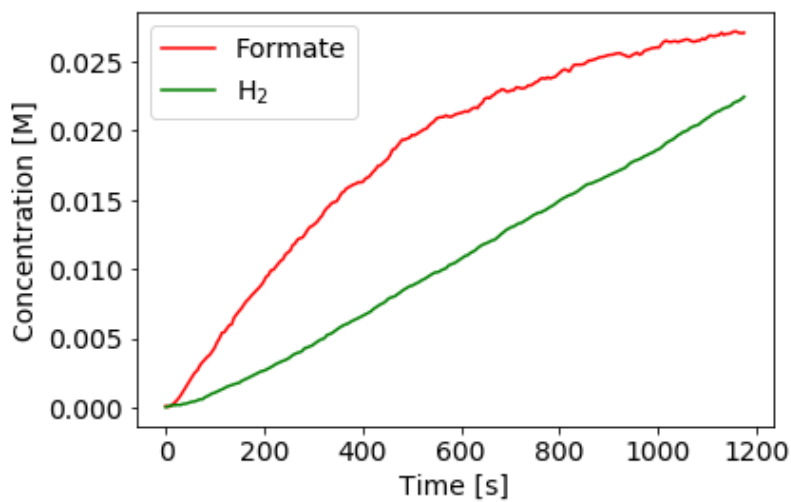


Figure S31

Formate autocatalysis simulated for radiolysis using 10 MeV γ rays.

References

- (1) Gillespie, D. T. A General Method for Numerically Simulating the Stochastic Time Evolution of Coupled Chemical Reactions. *Journal of Computational Physics* **1976**, 22 (4), 403–434. [https://doi.org/10.1016/0021-9991\(76\)90041-3](https://doi.org/10.1016/0021-9991(76)90041-3).
- (2) Getoff, N.; Schenck, G. O. Primary Products of Liquid Water Photolysis at 1236, 1470 and 1849 Å. *Photochemistry and Photobiology* **1968**, 8 (3), 167–178. <https://doi.org/10.1111/j.1751-1097.1968.tb05859.x>.
- (3) Zumdahl, S. S. *Chemical Principles*, 5th edition.; Houghton Mifflin: Boston, 2004.
- (4) Wang, X.; Conway, W.; Burns, R.; McCann, N.; Maeder, M. Comprehensive Study of the Hydration and Dehydration Reactions of Carbon Dioxide in Aqueous Solution. *J. Phys. Chem. A* **2010**, 114 (4), 1734–1740. <https://doi.org/10.1021/jp909019u>.
- (5) Dreybrodt, W.; Lauckner, J.; Zaihua, L.; Svensson, U.; Buhmann, D. The Kinetics of the Reaction $\text{CO}_2 + \text{H}_2\text{O} \rightarrow \text{H}^+ + \text{HCO}_3^-$ as One of the Rate Limiting Steps for the Dissolution of Calcite in the System $\text{H}_2\text{O} - \text{CO}_2 - \text{CaCO}_3$. *Geochimica et Cosmochimica Acta* **1996**, 60 (18), 3375–3381. [https://doi.org/10.1016/0016-7037\(96\)00181-0](https://doi.org/10.1016/0016-7037(96)00181-0).
- (6) Mitchell, M. J.; Jensen, O. E.; Cliffe, K. A.; Maroto-Valer, M. M. A Model of Carbon Dioxide Dissolution and Mineral Carbonation Kinetics. *Proceedings of the Royal Society of London A: Mathematical, Physical and Engineering Sciences* **2010**, 466 (2117), 1265–1290. <https://doi.org/10.1098/rspa.2009.0349>.
- (7) Šljukić, B.; Baron, R.; Compton, R. G. Electrochemical Determination of Oxalate at Pyrolytic Graphite Electrodes. *Electroanalysis* **2007**, 19 (9), 918–922. <https://doi.org/10.1002/elan.200703852>.
- (8) Pastina, B.; LaVerne, J. A. Effect of Molecular Hydrogen on Hydrogen Peroxide in Water Radiolysis. *J. Phys. Chem. A* **2001**, 105 (40), 9316–9322. <https://doi.org/10.1021/jp012245j>.
- (9) Domnanich, K. A.; Severin, G. W. A Model for Radiolysis in a Flowing-Water Target during High-Intensity Proton Irradiation. *ACS Omega* **2022**, 7 (29), 25860–25873. <https://doi.org/10.1021/acsomega.2c03540>.
- (10) Getoff, N. CO_2 and CO Utilization: Radiation-Induced Carboxylation of Aqueous Chloroacetic Acid to Malonic Acid. *Radiation Physics and Chemistry* **2003**, 67 (5), 617–621. [https://doi.org/10.1016/S0969-806X\(03\)00145-2](https://doi.org/10.1016/S0969-806X(03)00145-2).
- (11) Eggins, B. R.; Brown, E. M.; McNeill, E. A.; Grimshaw, J. Carbon Dioxide Fixation by Electrochemical Reduction in Water to Oxalate and Glyoxylate. *Tetrahedron Letters* **1988**, 29 (8), 945–948. [https://doi.org/10.1016/S0040-4039\(00\)82489-2](https://doi.org/10.1016/S0040-4039(00)82489-2).
- (12) Alberty, R. A. *Thermodynamics of Biochemical Reactions*, 1st ed.; John Wiley & Sons, Ltd, 2003. <https://doi.org/10.1002/0471332607>.
- (13) Burgess, D. R., N. O. of D. and. *NIST Chemistry WebBook, NIST Standard Reference Database Number 69*. <https://doi.org/10.18434/T4D303>. (accessed 2024-07-26).
- (14) Miller, S. L.; Smith-Magowan, D. The Thermodynamics of the Krebs Cycle and Related Compounds. *Journal of Physical and Chemical Reference Data* **1990**, 19 (4), 1049–1073. <https://doi.org/10.1063/1.555878>.
- (15) Eggins, B. R.; McMullan, E. A. Kinetic Control and Adsorption in the Voltammetry of Glyoxylate. *Collect. Czech. Chem. Commun.* **1989**, 54 (10), 2631–2637. <https://doi.org/10.1135/cccc19892631>.
- (16) Bard, A. J.; Faulkner, L. R. *Electrochemical Methods: Fundamentals and Applications*; Wiley, 2001.
- (17) Barham, H. N.; Clark, L. W. The Decomposition of Formic Acid at Low Temperatures. *J. Am. Chem. Soc.* **1951**, 73 (10), 4638–4640. <https://doi.org/10.1021/ja01154a042>.

- (18) Semelsberger, T. A.; Ott, K. C.; Borup, R. L.; Greene, H. L. Role of Acidity on the Hydrolysis of Dimethyl Ether (DME) to Methanol. *Applied Catalysis B: Environmental* **2005**, *61* (3), 281–287. <https://doi.org/10.1016/j.apcatb.2005.05.014>.
- (19) Namuangruk, S.; Meeprasert, J.; Khemthong, P.; Faungnawakij, K. A Combined Experimental and Theoretical Study on the Hydrolysis of Dimethyl Ether over H-ZSM-5. *J. Phys. Chem. C* **2011**, *115* (23), 11649–11656. <https://doi.org/10.1021/jp202408q>.